Available online at www.sciencedirect.com
SCIENCE DIRECT®
Progress in Particle and Nuclear Physics
52 (2004) 133–195

Progress in
Particle and
Nuclear Physics

www.elsevier.com/locate/ppnp

Review

Precision spectroscopy of light exotic atoms

D. Gotta

Institut für Kernphysik, Forschungszentrum Jülich, D-52425 Jülich, Germany

Received 26 September 2003

Abstract

The new era in X-ray spectroscopy of exotic atoms is based on high-resolution reflection-type crystal spectrometers, state-of-the-art X-ray detectors, and sophisticated set-ups to stop the negatively charged particles provided by modern accelerator facilities. Measurements on the elementary systems formed with hydrogen and helium isotopes yield a precision unprecedented in low-energy strong-interaction physics. Spin–spin and spin–orbit effects were identified in antiprotonic hydrogen and hadronic effects were observed for the first time in antiprotonic deuterium. In kaonic hydrogen strong-interaction effects could finally be identified unambiguously. For the pion–proton and pion–deuteron system the measurements reach an accuracy for the hadronic shift of a few per mill, which demands further theoretical effort to extract the scattering lengths at the same level. To allow a precise determination of the pion–nucleon coupling constant, which constitutes a stringent test of the approach for quantum chromodynamics in the non-perturbative regime, a new series of measurements has been started aiming at an accuracy of 1% for the hadronic width in pionic hydrogen. The mass of the charged pion was re-measured by using light pionic and muonic atoms and the first direct observation of Coulomb explosion was achieved for exotic atoms. Tests of bound-state quantum electrodynamics became possible at an accuracy which in turn can be used now to establish X-ray standards in the few keV range by the pionic atoms themselves.

PACS: 36.10.-k; 36.10.Gv; 36.10.Dr; 25.45.+t; 25.80.Hp; 12.20.Fv; 14.40Aq; 07.85Jy; 29.30kv

Keywords: Exotic atoms; Antiprotonic atoms; Kaonic atoms; Pionic atoms; Light hadronic atoms; Low-energy strong interaction; Pion mass; Bound-state QED; Exotic-atom cascade; Crystal spectrometer; X-ray detection; X-ray standards; Fluorescence X-rays

---

Contents

1. Introduction 135
2. Exotic atoms 137

E-mail address: d.gotta@fz-juelich.de (D. Gotta).

doi:10.1016/j.ppnp.2003.09.003

- 2.1. From capture to quantum cascade ... 137
- 2.2. General aspects of the atomic cascade ... 137
- 2.3. Cascade in exotic hydrogen and helium ... 139

3. Hadronic effects ... 143
- 3.1. Nucleon–antinucleon ... 146
- 3.2. Kaon–nucleon ... 147
- 3.3. Pion–nucleon ... 148

4. Experimental techniques ... 150
- 4.1. Cyclotron trap and X-ray source ... 151
- 4.2. Crystal spectrometer ... 152
  - 4.2.1. Resolution ... 152
  - 4.2.2. Energy and efficiency calibration ... 153
- 4.3. X-ray detectors ... 155
- 4.4. Linear stop arrangement and triggered X-ray detectors ... 155

5. Strong-interaction results ... 155
- 5.1. Antiprotonic hydrogen ... 155
  - 5.1.1. 1s ground state ... 155
  - 5.1.2. 2p state ... 158
- 5.2. Antiprotonic deuterium ... 162
  - 5.2.1. 1s ground state ... 162
  - 5.2.2. 2p state ... 163
- 5.3. Antiprotonic helium and lithium ... 163
- 5.4. Kaonic hydrogen and helium ... 166
- 5.5. Pionic hydrogen and deuterium ... 169
  - 5.5.1. Cascade effects ... 169
  - 5.5.2. Ground-state shift in πH ... 169
  - 5.5.3. Ground-state broadening in πH ... 170
  - 5.5.4. Ground-state shift in πD ... 171
  - 5.5.5. Scattering lengths $a^{\pm}$ and the πN coupling constant ... 172
- 5.6. Pionic helium ... 174

6. Supplementary results ... 175
- 6.1. Mass of the charged pion ... 175
- 6.2. Coulomb explosion ... 178
- 6.3. Bound-state QED ... 180
  - 6.3.1. Hyperfine structure in $\bar{p}$H and $\bar{p}$D ... 181
  - 6.3.2. Antiprotonic helium ... 182
  - 6.3.3. Test of the Klein–Gordon equation ... 182
- 6.4. Fluorescence X-rays ... 183

7. Conclusions ... 185
- 7.1. Summary of results ... 185
  - 7.1.1. Strong interaction ... 185
  - 7.1.2. Pion mass and electromagnetic properties of exotic atoms ... 186
- 7.2. Outlook ... 186
  - 7.2.1. Hadronic interaction ... 186
  - 7.2.2. Particle properties ... 187
  - 7.2.3. Multidisciplinary problems ... 187

Acknowledgements ... 188

References ... 188

1. Introduction

Systems in which a heavier particle of negative charge is bound into atomic orbits by the Coulomb field of the nucleus are called **exotic atoms**. Predicted in the 1940s [1–3], their existence was first established by the observation of Auger electrons in photographic emulsions [4]. Characteristic X-rays from pionic and muonic atoms were identified for the first time in the early 1950s. Up to now, X-radiation from exotic atoms with muons [5], pions [6], kaons [7], antiprotons [8], and sigma hyperons [9] has been established.

In leading order, given by the *Bohr* formula,[1] the binding energies B_n are proportional to the reduced mass m_{red} of captured particle and nucleus $A(Z, N)$. *Bohr* radii r_{B} and consequently the expectation values of orbit radii $\langle r_n\rangle$ are proportional to $1/m_{\mathrm{red}}$:

$$B_n = m_{\mathrm{red}}c^2\alpha^2 Z^2/2n^2 \tag{1}$$

$$r_{\mathrm{B}} = \hbar c/m_{\mathrm{red}}c^2\alpha Z \tag{2}$$

$$\langle r_n\rangle = r_{\mathrm{B}}\cdot[3n^2 - \ell(\ell+1)]/2. \tag{3}$$

The transition energies are increased approximately by the ratio m/m_e of the masses of the captured particle and the electron. Even for light elements such atomic systems reach nuclear dimensions for the low-lying states (Table 1). This allows a large variety of investigations:

- hadronic interaction at threshold [10–18],
- masses and magnetic moments of negatively charged particles [19–22],
- tests of bound-state quantum electrodynamics (QED) [23, 24],
- interaction with the electron shell of atoms and molecules [25],
- nuclear properties [17, 26],
- electro-weak interaction [27–30], and
- muon-catalyzed fusion [31–33].

Table 1

Binding energies B_{1s} of the atomic ground state and "*Bohr* radii" r_{B} of "electronic" and "exotic" hydrogen for a captured particle of mass m. ℓ_{had} denotes the angular momentum states noticeably affected by strong interaction. *Hadronic decay* indicates the corresponding most important final state

	$m/\mathrm{MeV/c^2}$	B_{1s}/keV	$r_{\mathrm{B}}/10^{-15}$ m	Accessible interactions	ℓ_{had}	Hadronic decay
ep	0.511	13.6×10^{-3}	0.53×10^{5}	Electro-weak	–	–
μp	105.7	2.53	279	Electro-weak	–	–
πp	139.6	3.24	216	Electro-weak + strong	s	$\to \pi^\circ n$
Kp	493.7	8.61	81	Electro-weak + strong	s, p	$\to \Sigma\pi$
$\bar{p}$p	938.3	12.5	58	Electro-weak + strong	s, p	$\to$ mesons

---

[1] The symbols α, Z, n, and ℓ denote the fine structure constant, the nuclear charge, the principal quantum number and the angular momentum. The present value of the conversion constant $\hbar c$ is $197.326\,9602 \pm 0.000\,0077$ MeV fm [34].

From the beginning, strong-interaction physics was a major motivation for studying exotic atoms. Atomic binding energies of light systems are in the keV range, which is far below the hadronic scale of about 1 GeV. Hence, exotic atoms offer the unique possibility to perform experiments equivalent to scattering at vanishing relative energy. This allows the determination of the hadron–nucleus interaction at threshold without extrapolation as necessary in the case of low-energy scattering data. Of particular interest for exotic-atom experiments are studies of the systems formed with hydrogen isotopes, as these give access to the basic low-energy parameters—the hadron–proton scattering lengths and volumes. Deuterium enables access to the hadron–neutron system. Other light elements and especially isotope effects yield information on how to construct the particle–nucleus interaction from the elementary reactions. It is noteworthy that light exotic atoms can be obtained electron-free, which makes them true hydrogen-like systems. This opens new potentialities for high-precision measurements due to the absence of any screening effects.

The theoretical description of the low-energy hadronic interaction has reached different levels, which is also reflected in the different approaches applied to hadronic atoms. There is the workhorse even today, the *optical potential* and the more microscopic view of *meson exchange*. Finally with *chiral perturbation theory* (χPT) a framework has been developed, which is based on the fundamental description of strong interaction—the quantum chromodynamics (QCD).

The progress in the understanding of exotic atoms is closely related to the development of experimental techniques. Whereas the early experiments measured X-rays from several tens of keV to the MeV range by using NaI(Tl) scintillators, the advent of high-resolution semiconductor detectors immediately led to substantial progress in the spectroscopy of exotic atoms [12, 35]. A further step was achieved by introducing crystal spectrometers [36] when meson factories at the Paul-Scherrer-Institut (PSI) [37], TRIUMF, and LAMPF provided high-intensity muon and pion beams. From 1983 until 1996, at CERN, high-quality antiproton beams were available at the low-energy-antiproton ring (LEAR) [38]. With all that, exotic-atom research became high-precision physics [39].

This article outlines recent results obtained from light exotic atoms. They were achieved with dedicated techniques developed for high-precision measurements of X-rays in the few keV range. Experiments include reflection-type crystal spectrometers, new-generation X-ray detectors such as charge-coupled devices (CCDs) and trigger capabilities on particles in the final state to allow background suppression, cryogenic targets, and a particle concentrator—the cyclotron trap—in order to produce bright X-ray sources. Such efforts are mandatory to compensate for the low count rates inherent to high-resolution devices even at the high-flux beam lines at LEAR and PSI or to counteract severe background conditions.

Besides X-ray spectroscopy, additional important methods for investigating exotic atoms were developed, which are not subjects of this review. Laser techniques are used for studies of the meta-stable high-lying levels in antiprotonic helium, which give detailed insight into cascade processes and test QED at the ultimate precision [40]. To access the pion–nucleon s-wave interaction in heavy nuclei, deeply bound pionic states have been populated in proton–nucleus collisions in recoilless kinematics [41, 42].

During the last decade, antiprotonic atoms were studied with a crystal spectrometer for the first time and the first unambiguous observation of kaonic hydrogen could be achieved.

Experiments are going on at the continuously improved pion beams of PSI investigating the pion–nucleon interaction with increasing precision. High resolution allows one to resume the tradition of testing bound-state QED and, beyond that, new insights into exotic-atom and exotic-molecule formation and de-excitation [43]. Supplementary studies of fluorescence X-rays from electronic atoms demonstrate the potential of exotic atoms to serve as X-ray standards and to take over calibration methods from other fields.

The experiments discussed in the following comprise aspects of the

- hadronic interaction in exotic hydrogen and helium,
- mass of the negatively charged pion,
- tests of bound-state QED in pionic and antiprotonic atoms, and
- cascade effects in muonic and pionic atoms.

2. Exotic atoms

2.1. *From capture to quantum cascade*

The negatively charged particles, after being slowed down to a kinetic energy of a few tens of eV, are bound into highly excited atomic states at about the radius of the outermost electrons. Deceleration at the lowest energies is caused by processes similar to friction acting on the particle when moving through the electron cloud [44]. Kinetic energy is absorbed by electron emission or electron excitation to unoccupied atomic states.

As a rule of thumb, the quantum cascade of the heavy captured particle starts where the overlap of the wavefunctions is maximal with the outermost electrons of the atom or molecule. The initial principal quantum number is about $n \approx n_e\sqrt{m/m_e}$, where n_e is the principal quantum number of the outermost electron shell. The value for the square-root expression is 14, 16, 31, and 40 for muons, pions, kaons, and antiprotons, respectively.

Because of the large number of degrees of freedom, capture is generally very complex. It depends on atomic and molecular structure and the range of values for n and angular momentum states ℓ at capture is specific to the element or compound under consideration [45, 46]. Cascade models mostly use a modified statistical distribution $P_\ell \propto (2\ell+1)\mathrm{e}^{\alpha\ell}$ for the angular momentum states starting the calculation at $n = \sqrt{m/m_e}$ which is only a crude approximation for the initial population. Hence, the X-ray yields of the transitions between states of low n contain only indirect information on capture and the first de-excitation steps. The parameter α is fitted to the data and the modulus of its value is typically $\simeq$0.2 or less [345]. Detailed descriptions of capture and atomic cascade may be found in [47, 48] and [25], respectively.

2.2. *General aspects of the atomic cascade*

For atoms with $Z > 2$, the development of the subsequent quantum cascade is determined by the different energy dependences of the two leading de-excitation mechanisms, **Auger emission** of electrons and **radiative decay**. For hydrogen (Fig. 1), however, and to some extent for helium, other mechanisms such as **Stark mixing** and **Coulomb de-excitation** become dominant (see below). The typical cascade of exotic atoms with $Z > 2$ may be divided into three parts:

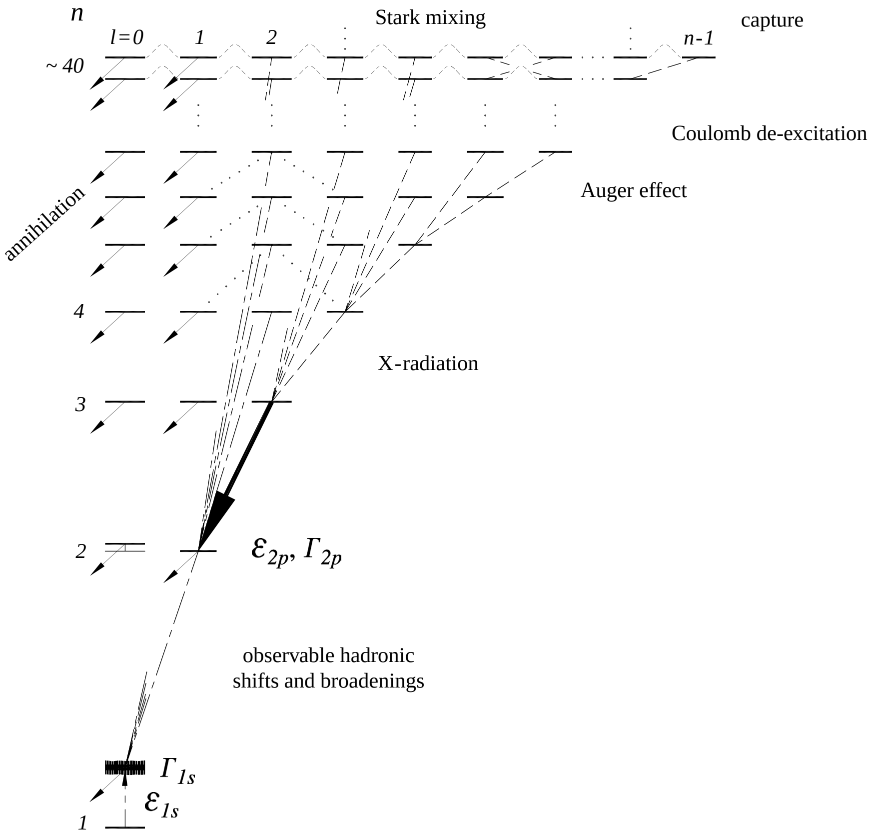

Fig. 1. Atomic cascade in antiprotonic hydrogen. The strong interaction, leading to a repulsion in the case of $\bar{p}$p, manifests itself in an energy shift ϵ and broadening Γ of the low-lying and inner atomic levels. The hadronic parameters ϵ and Γ scale with the geometrical overlap (Section 3). In this article, a positive (negative) sign of ϵ stands for an attractive (repulsive) interaction, i.e., $\epsilon \equiv E_{\mathrm{exp}} - E_{\mathrm{QED}}$. E_{exp} denotes the measured and E_{QED} the (calculated) pure electromagnetic transition energy.

- **Depletion of the electron shell.** The emission of remaining electrons proceeds shell by shell through successive Auger emissions as soon as the energy difference between the exotic-atom levels exceeds the ionisation energy for an electron. Because Auger transitions prefer a small energy difference between initial and final state ($\Gamma_A \propto 1/\sqrt{\Delta E_{nn'}}$ and $\Delta\ell = \pm 1$ [49]), the initial distribution of the angular momentum states ℓ does not change significantly in the upper part of the cascade. Auger transition rates exceed radiative de-excitation for $\Delta n = 1$ transitions ($\Gamma_X \propto n^{-5}$ for $n \gg 1$ [50, 51]) down to about $n \geq 5$ and $n \geq 9$ in the case of medium Z muonic and antiprotonic atoms, respectively, as can be seen from inspecting Ferrell's formula $\Gamma_A/\Gamma_X = \sigma_{\gamma e}^{(Z-1)}(E)/[(Z-1)^2\sigma_T]$ [52].[2]

---

[2] $\sigma_{\gamma e}(E)$ and σ_T denote the photoelectric and the Thomson cross sections.

Therefore, X-ray transitions from above those levels are suppressed as long as electrons are present.

- **Point-nucleus regime.** In lighter exotic atoms and when using dilute targets, hydrogen-like systems are formed by depletion of the electron shell. This is in particular true for antiprotons, where the large value of the initial principal quantum number n provides enough de-excitation steps in the cascade to empty all electron shells completely. A pure radiative cascade already develops in the intermediate part of the cascade without satellite transitions because of the absence of electron screening [53–55]. Due to the strong energy dependence of the radiative decay ($\Gamma_X \propto \Delta E^3_{nn'}$ [51]), the population of the states with maximum angular momentum $(n, \ell = n-1)$ is strongly enhanced by $\Delta n \gg 1$ transitions. In light exotic atoms, from such so-called circular states, further decay can proceed exclusively by $\Delta n = 1$ electromagnetic electric dipole $(E1)$ transitions.

  In the intermediate part finite-size effects can be neglected and the transition energies are determined exclusively by the electromagnetic interaction, the mass A of the nucleus, and the mass of the captured particle x. In dilute gas targets the line intensities in $Z > 2$ systems are saturated even for large n, i.e., line yields are of the order of 90% (Fig. 5). In heavier atoms and dense or solid targets, where electron capture (refilling) $(x^-A)_{n\ell}N\mathrm{e}^- + \mathrm{e}^- \rightarrow (x^-A)_{n\ell}(N+1)\mathrm{e}^-$ from the surrounding atoms occurs, de-excitation continues at first by Auger emission. In general the remaining electron configuration de-excites immediately to its ground state, before the next transition of the captured particle occurs.

  In the lower part of the cascade, X-ray emission dominates even when electrons are left due to the sharp increase of the energy gain per transition. The cascade time is basically given by the first radiative transition because of the much faster Auger transitions. As the radiative width strongly depends on the nuclear charge ($\Gamma_X \propto Z^4$ [50]), the cascade time becomes quickly shorter with increasing Z.

- **Particle–nucleus interaction.** During the very last steps of the cascade, the finite size of the nucleus affects the atomic level structure even in the lightest exotic atom. In the case of strongly interacting particles such as pions, kaons, or antiprotons, electromagnetic de-excitation finally has to compete with hadronic reactions. The presence of a hadronic potential causes an energy shift $\epsilon_{n\ell}$ of the atomic levels as compared to the pure electromagnetic interaction. The reaction channels opened by strong interaction reduce the lifetime of the low-angular-momentum states, which appears as a line broadening $\Gamma_{n\ell}$ of the X-ray transitions.

2.3. *Cascade in exotic hydrogen and helium*

Exotic hydrogen occupies a special position regarding the interaction with the target material. It is electrically neutral and rather small on the atomic scale and, therefore, approaches closely nuclei of neighboring atoms and experiences their Coulomb field. The frequent collisions are most important for the evolution of the cascade because of the slow radiative de-excitation (Table 2). The cross sections of all collisional processes are of geometrical order of magnitude, i.e., of about the size of the exotic atom $\sigma_{\mathrm{coll}} \approx \pi \langle r_n \rangle^2$. Non-radiative mechanisms also from collisional processes prefer $\Delta n = 1$ transitions and

Table 2
Processes occurring during the atomic cascade of exotic atoms, transition rates Γ_{nl} for $n \gg 1$, and the main decay mode of the unstable particles. Because of the short cascade time only a few per cent decay for the lightest elements and at low densities. τ_0 denotes the decay time of the free particle [34] and N the number of electrons

Process	Example		Γ_{nl}
El. dipole (E1)	$(x^-\mathrm{p})_{n\ell} \to (x^-\mathrm{p})_{n',\ell-1} + \gamma$	$Z \geq 1$	$\propto n^{-5}$
Internal Auger effect	$(x^-A)_{n\ell}\mathrm{Ne}^- \to (x^-A)_{n'\ell'}(\mathrm{N}-1)\mathrm{e}^- + \mathrm{e}^-$	$Z \geq 2$	$\propto n^7$
External Auger effect	$(x^-\mathrm{p})_{n\ell} + \mathrm{H} \to (x^-\mathrm{p})_{n'\ell'} + \mathrm{P} + \mathrm{e}^-$	$Z = 1$	
Stark mixing	$\lvert n\ell m\rangle \leftrightarrow \lvert n(\ell \pm 1)m\rangle$	$Z \leq 1$	$2 \times 10^9/\mathrm{s}(n = 30)^{\mathrm{b}}$
Coulomb de-excitation[a]	$(x^-\mathrm{p})_{n\ell} + \mathrm{H}_2 \to (x^-\mathrm{p})_{n'\ell'} + \mathrm{H} + \mathrm{H}$	$Z = 1$	$1 \times 10^9/\mathrm{s}(n = 30)^{\mathrm{b}}$
Elastic scattering	$(x^-\mathrm{p})_{n\ell} + \mathrm{H}_2 \to (x^-\mathrm{p})_{n\ell} + \mathrm{H}_2{}^*$	$Z = 1$	$1 \times 10^9/\mathrm{s}(n = 12)^{\mathrm{b}}$
Electron capture	$(x^-A)_{n\ell}\mathrm{Ne}^- + \mathrm{e}^- \to (x^-A)_{n\ell}(N+1)\mathrm{e}^-$	$Z > 2$	
Weak decay	$\mu^- \to \mathrm{e}^- + \bar{\nu}_e + \nu_\mu$		$\tau_0 = 2.2\ \mu\mathrm{s}$
Weak decay	$\pi^- \to \mu^- + \bar{\nu}_\mu$		$\tau_0 = 26\ \mathrm{ns}$
Weak decay	$K^- \to \mu^- + \bar{\nu}_\mu$		$\tau_0 = 12\ \mathrm{ns}$

[a] *Coulomb de-excitation* comprises the *chemical de-excitation* as introduced in [58] to take into account the missing non-radiative de-excitation strength.

[b] Transition rates in $\bar{\mathrm{p}}\mathrm{p}$ for a kinetic energy of 1 eV at 10^{-4} of liquid hydrogen density (from [78]).

* Denotes a (possibly) excited H_2 molecule. The exotic atom remains in the same quantum state.

are able to change the velocity of the exotic atom significantly during the de-excitation. All these effects counteract the development of a distinct circular cascade. Recently developed cascade models, so-called *extended standard cascade models* [56, 57], take into account the evolution of the kinetic energy distribution. A review of progress in the cascade theory of exotic hydrogen may be found in [48].

- **Stark mixing.** When passing through a Coulomb field during collisions with other target atoms, the electric field $\mathbf{E}$ mixes the pure parity states $\lvert n\ell m\rangle$ because of the non-vanishing matrix element $\langle n\ell m\lvert\mathbf{E}\rvert n\ell' m'\rangle$. Mixing occurs between states of the same principal quantum number n but different angular momentum according to the selection rules $\Delta\ell = \pm 1$ and $\Delta m = 0$ [51].

  Stark mixing prevails over all other internal and external de-excitation processes except radiation from low-lying states and, therefore, primarily determines the density dependence of the X-ray line yields. It can be described by introducing $(\Delta\ell = \pm 1, \Delta m = 0)$ transition rates Γ_{Stark}. For high-n states the transition rates Γ_{Stark} are large enough to allow numerous transitions between ℓ states during the typical collision time τ_{Stark} of 10^{-14}–10^{-13}s. In hadronic hydrogen the induced s- and p-wave contributions in high-angular-momentum states lead with high probability to absorption or annihilation [25, 49, 58–63]). As shown in Fig. 2, *Stark mixing* leads to a drastic reduction of the X-ray yields with increasing target density (Day–Snow–Sucher effect [64]). A further consequence is the very short time from Coulomb capture to absorption or annihilation in dense targets (cascade time), which has been observed already from bubble chamber data [65].

  Assuming the splitting of the energy levels $\Delta E_{n,\ell\pm 1} \ll \Gamma_{\mathrm{Stark}}$ and $\tau_{\mathrm{Stark}} \cdot \Gamma_{\mathrm{Stark}} \gg \hbar$, the mixing is complete and a statistical population is re-established for each n.

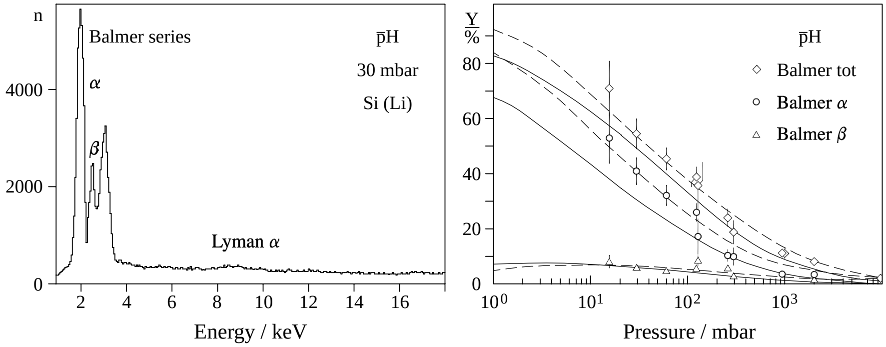

Fig. 2. *Left*: X-ray spectrum from $\bar{p}$H measured with a 30 mm^2 Si(Li) showing the almost fully developed Balmer transitions. The Lyman α line is suppressed due the strong p-state annihilation (from [62]). *Right*: Absolute line yields of Balmer transitions. Data are from LEAR experiments PS171 [89], PS174 [90], and PS175 [62]. Dashed lines show the results of the cascade code of Borie and Leon [58] with the parameters fitted to the line yields for $T_{\text{kin}} = 1$ eV (from [62]). The solid lines result from the recently developed *extended standard cascade model* of Jensen and Markushin [48, 78], which follows the development of the kinetic energy distribution during cascade.

In the case of hadronic atoms mixing is suppressed for the low-lying low-angular-momentum states by the large level shift due to the strong interaction. For example, in $\bar{p}$H and $\bar{p}$He below n $\cong$ 9 s–p and p–d mixing, respectively, no longer occurs.

In exotic helium *Stark mixing* is much less pronounced than for hydrogen, but is still the process which dominates the pressure dependence of the line yields [66–69]. At higher densities, above about 10 bar, in addition molecule–ion formation has to be taken into account [66]. The formation of the positively charged exotic helium $(x^-\text{He})^+$ with another He atom into a molecule could explain an anomaly observed in π ^{4}He for liquid helium, where the Kα yield was found to be lower than the Kβ yield [70].

- **Coulomb de-excitation** is a non-radiative cascade process competing with *external Auger emission* and *radiative decay* [56, 71]. It occurs during a collision of exotic hydrogen and the energy release $\Delta E_{nn'}$ for step $n \to n'$ is converted into kinetic energy of the x^-p system and H (from a molecule H_2). *Coulomb de-excitation* was observed directly as a broadening in the time-of-flight (TOF) spectrum of the monoenergetic neutrons from the charge-exchange reaction $\pi^-\text{p} \to \pi^0\text{n}$ at rest [72–75]. The TOF spectrum turned out to be a superposition of several Doppler broadened contributions corresponding to various de-excitation steps $n \to n'$. The fastest component identified corresponds to a kinetic energy of 200 eV and, therefore, is attributed to the (3–2) Coulomb transition. $\Delta n = 1$ transitions are preferred in agreement with calculations, but evidence for $\Delta n = 2$ has been found from the TOF measurement. *Coulomb de-excitation* has been considered so far only for hydrogen, but is not in principle excluded for exotic helium.
- **Elastic scattering** and Stark collisions counteract the acceleration by *Coulomb de-excitation*, but they are not assumed to be sufficient to thermalise the exotic-hydrogen atom. In a detailed consideration of the various cascade processes the cross sections

for Coulomb and Stark transitions and scattering were calculated simultaneously for large n instead of fitting strength parameters to the line yields [76–78]. It turned out that *Coulomb de-excitation* is the dominant process for $n > 20$ but remains important also for lower-lying states. The large energy gain leads to a significant Doppler broadening of subsequent X-ray transitions. For that reason, the inclusion of the evolution of the kinetic energy became mandatory in cascade theory.

- **External Auger effect.** Auger emission off H_2 molecules reaches a similar rate to Coulomb and Stark transitions when the energy gain for Δn transitions exceeds the electron's binding energy. Auger emission therefore contributes significantly in the range $n \approx 6$–10 [78, 79].
- **Cascade times** have been measured in $\bar{p}$H at 1 bar (NTP) by the ASTERIX collaboration [80] to 5.1 ± 0.7 ns and both in $\bar{p}$H and $\bar{p}$He at very low pressures by the OBELIX experiment [81, 82]. For $\bar{p}$H at 3.4 mbar a cascade time of 84 ± 10 ns was obtained. A comparison of a recent calculation which accounts for the strong *Coulomb de-excitation* [78] leads to shorter cascade times than a previous one using an effective cross section for chemical de-excitation given by $\pi \langle r_n \rangle^2$—the geometrical size of the $\bar{p}$p system [59]. Shorter cascade times are in much better agreement with data, especially below 10 mbar. Recently, at 3 mbar a cascade time of 30 ns has been reported by the ASACUSA collaboration when starting from the $(n = 31, \ell = 30)$ state in $\bar{p}$He [83]. This is less than half the value given by Bianconi et al. [82] but the time elapsed from Coulomb capture to the arrival at this particular level is not included here.
- **Influence of the strong interaction.** For exotic hydrogen and helium when formed with hadrons, the use of low-pressure gas targets is essential to achieve high X-ray yields, in particular for $\bar{p}$H where the strong p-state annihilation further suppresses the K transitions (Fig. 2). Due to the large s- and p-state annihilation $\ell = 1$ states are fed almost exclusively from that part of the atomic cascade which did not pass through any s or p state. For that reason the line yields are hardly sensitive to the annihilation widths $\Gamma_{n\mathrm{p}}$ and $\Gamma_{n\mathrm{s}}$ [58, 84]. As expected, no isotope effect was identified from the line yields within the present experimental accuracy [62], but at the 20% level from a precise measurement of the capture probabilities of pions in HD and $H_2 + D_2$ mixtures [85].

  If a direct measurement of the level width is excluded, a yield measurement of the $\bar{p}$H Lyman α permits the determination of the 2p annihilation width from the intensity balance of the Lyman α and the whole Balmer series.[3] The quantity $\Gamma_{2\mathrm{p}}^{\mathrm{bal}}$ derived in this way, however, coincides with the true spin-averaged hadronic width $\Gamma_{2\mathrm{p}}$ only in the limit of equal annihilation rate from *all* 2p hyperfine states [14, 62, 86] (see Section 5.1.2).

---

[3] In the *Bohr* model, the terms Lyman and Balmer lines denote any transitions to the $n = 1$ and $n = 2$ states from excited states. Lines are labeled by Greek letters starting with α for the one with the lowest energy. Ignoring substructures the labeling of an exotic-atom transition by, e.g., Balmer α is not absolutely precise. Following *Siegbahn's* notation [91], in the case of $\bar{p}$p Balmer α represents the three (3d–2p) fine structure lines $L\alpha_1$, $L\alpha_2$, and $L\beta_1$.

In antiprotonic helium strong-interaction effects occur in s, p, and d states (Section 5.3). The relative contribution of the various partial waves can be calculated by cascade models almost with the accuracy given by the knowledge of the hadronic widths [68, 84]. *Stark mixing* is still important. Temperature or equivalent kinetic energy determine in certain limits the relative s-, p-, and d-wave annihilation. For example, a cascade calculation yields for a density of 1 bar for s-/p-/d-absorption the ratios 6%/47%/47% at 300 K and 1%/41%/58% at 5 K in $\bar{\mathrm{p}}^4$He [68, 84]. The percentage given here represents almost the full range of variation, unlike the case for $\bar{p}$H, where s- to p-state annihilation changes from about 0.1 to 10 from dilute gas ($\ll$1 bar) to liquid hydrogen [87, 88].

3. Hadronic effects

In light exotic atoms, binding energies and, consequently, kinetic energies are in the keV range (Table 1), which is small compared to the typical hadronic scale represented by the nucleon mass of ~1 GeV. Therefore, X-ray spectroscopy of exotic atoms offers the possibility of performing a scattering experiment directly at threshold. The connection between low-energy scattering and strong-interaction effects in exotic atoms may be illustrated by inspecting the partial wave expansion of the scattering amplitude $f(\Theta) = \sum_\ell f_\ell(\Theta)$, where $f_\ell(\Theta) = (2\ell+1)a_\ell k^{2\ell} P_\ell(\cos\Theta)$. For vanishing momentum $k \to 0$, the amplitude $f(\Theta)$ reduces to the s-wave scattering length a_s, which is the basic parameter representing the interaction at threshold. Besides scattering, absorption or annihilation occurs and in analogy to optics, where the complex refraction index takes into account non-coherent processes, a complex *(optical) potential* is introduced. Then the scattering length $\mathbf{a_s}$ becomes a complex number too.[4] Detailed discussions may be found in the reviews of Hüfner [10] and Klempt et al. [16] or the textbook of Ericson and Weise [18].

The relation between shift and broadening of the atomic ground state and the complex s-wave scattering length is given by an expansion in the parameter $\mathbf{a_s}/r_\mathrm{B}$, where $r_\mathrm{B} = \hbar c/m_\mathrm{red}c^2\alpha Z$ is the Bohr radius of the particle–nucleus system. The leading order using hydrogen-like wavefunctions $\Psi_{n\mathrm{s}}$ and taking the value of the wavefunction at the origin yields the Deser formula [92]

$$\begin{aligned}\epsilon_{ns} + i\Gamma_{ns}/2 &= -(2\pi\hbar^2/m_\mathrm{red}) \cdot |\Psi_{ns}(0)|^2 \cdot \mathbf{a_s}\\ &= -(2\hbar^2/m_\mathrm{red}r_\mathrm{B}^3) \cdot \mathbf{a_s}/n^3. \end{aligned} \tag{4}$$

For the next term in the low-energy expansion, for the p-wave, the scattering volume $\mathbf{a_p}$ reads in lowest order [93]

$$\begin{aligned}\epsilon_{np} + i\Gamma_{np}/2 &= -(6\pi\hbar^2/m_\mathrm{red}) \cdot |\nabla\Psi_{np}(0)|^2 \cdot \mathbf{a_p}\\ &= -(3\hbar^2/16m_\mathrm{red}r_\mathrm{B}^5) \cdot \mathbf{a_p} \cdot 32(n^2-1)/3n^5. \end{aligned} \tag{5}$$

Similar relations hold for higher-angular-momentum states [18, 94–96]. Corrections due to interference of the Coulomb and nuclear interaction are taken into account by

---

[4] Scattering lengths are printed in **bold face** when complex.

Table 3
Theoretical approach, exotic-hydrogen X-ray transition, and accessible hadron–nucleus properties

Meson exchange	$\bar{p}$H Kα	$\bar{\mathrm{N}}$N spin–spin force
+ optical potential	Lα	$\bar{\mathrm{N}}$N spin–orbit force
	$\bar{p}$D Kα	multiple scattering + annihilation strength
	Lα	multiple scattering + overlap
HBχPT	KH, KD Kα	KN isospin scattering length, KN sigma term
HBχPT	πH Kα	πN isovector and isoscalar scattering length, πN sigma term
	πD Kα	πN isoscalar scattering length + 3-body effects, isospin breaking

higher-order terms (*Trueman expansion*) [93]. Second-order terms, proportional to $(\mathbf{a}_\ell/r_B)^2$, are significant for s states of kaonic or antiprotonic systems. It is worth mentioning that in second order also the imaginary part of the scattering length contributes to the hadronic shift [93]. In the case of protonium the validity of the *Trueman expansion* was shown when a coupling of channels ($\bar{p}$p and $\bar{n}$n) occurs and tensor forces are present [97, 98].

As mentioned above the scattering lengths and volumes determined in this way do not yet represent the pure hadronic parameter $\mathbf{a}_\ell^s$, but describe the interaction resulting from the superposition of electromagnetic and strong potential and are denoted by $\mathbf{a}_\ell^{\mathbf{cs}}$. In $\bar{p}$p, such Coulomb corrections are sizable (up to 20%) for the s-states but already small for p-states [97, 99, 100] and the lightest pionic atoms. A rigorous treatment including the finite size of the nuclear potential was given by Mandelzweig and applied to medium-Z pionic atoms [101].

The scattering lengths may be regarded as the interface of experiment and theoretical understanding. The experimentally determined parameters have to be compared with the results from theory based on the most fundamental approach available. The level of "microscopic" understanding achieved is different for $\bar{N}A$, KA, and πA atoms corresponding approximately to the internal complexity of the hadrons involved (Table 3).

In the simplest version, the *local optical potential* is given by a phenomenological ansatz

$$U_{\mathrm{local}} = V(r) + \mathbf{i}W(r) = -(4\pi\hbar/2m_{\mathrm{red}})(1 + m_{\mathrm{red}}/M)\rho(r)\bar{\mathbf{b}}, \tag{6}$$

where the nuclear matter density distribution $\rho(r)$ is normalized to A. It was found that the variation of the hadronic effects over the whole periodic table could be described (except for a few special cases) by a few common quantities [10, 15, 18, 102–104]. They are understood as *effective* scattering lengths and volumes and the imaginary parts represent absorption or annihilation. Necessarily this procedure averages out details of the elementary interactions. In contrast to antiprotons or kaons, for pionic atoms and $A > 1$ nuclei terms proportional to ρ^2 must be included because pion absorption at rest takes place with two nucleons [10, 18]. The success of parametrising the *optical potential* in terms of effective scattering parameters is based on the validity of a multiple-scattering approach for the hadron–nucleus interaction and was developed first for pionic atoms by Ericson and Ericson [105, 106].

For the description of pionic atoms in $\ell > 0$ states a *non-local*—i.e., a momentum-dependent—part of the potential of the form $U_{\text{non-local}}(r) = (4\pi\hbar/2m_{\text{red}})(1 + m_{\text{red}}/M)\bar{\mathbf{c}}\nabla\rho(r)\nabla$ [107] was found to be necessary in addition. The strong influence of the p-wave πN interaction even at threshold is obvious from the large strength and width of the $\Delta(1232)$ resonance. The πN s-wave interaction is atypically weak for a hadronic process, which is now understood from chiral symmetry [18] (see below). Generally speaking, a local potential is sufficient in the case of K^- and $\bar{p}$ because of their short mean free path in nuclear matter [15, 108].

Meson exchange constitutes an understanding of the strong force mediated by various mesons and describing the medium- and long-range part. In the quark model, mesons and baryons are composite particles consisting of bound quark–antiquark and of three-quark combinations, respectively, where the strong force is mediated by the exchange of gluons. In the meson-exchange picture the strength of the consequently effective interaction and the internal degrees of freedom are condensed in (effective) couplings attributed to a specific *meson*NN vertex and the potential is build up from the sum of the contributing mesons. Commonly used starting points are the so-called *Paris* [109] and the *Bonn* potential [110].

QCD as a part of the standard model is today's basic theory of the strong interaction based on colored fermions—the quarks—and colored massless field quanta—the gluons. At highest energies, perturbative methods are applied with great success because of the decreasing strength of the interaction as described by a running strong coupling constant α_s (asymptotic freedom). At low energies, in the non-perturbative regime, a modern framework (χPT) has been developed, which is based on the symmetry of the QCD Lagrangian for the *ideal world* of two (or three) massless quarks u, d (and s), where *chirality* is conserved for ever. The symmetry of the strong force is broken by the Higgs field being an essential element in the description of the electroweak interaction. The Higgs mechanism leads to finite but small (current) quark masses of about 4, 6 and 125 MeV/c^2 for the light quarks u, d, and s, respectively [34]. Symmetry breaking together with the properties of the QCD vacuum, being responsible for the bulk part of the masses, is the basis of our existence and manifests itself in the particles observed in the *real world*. On the strong-interaction scale of about 1 GeV/c^2, the zero mass limit is closely approached for the first quark doublet and an expansion around the *chiral limit* $m_u = m_d = (m_s =)\ 0$ should provide a reasonable description at low energies. χPT relates unambiguously the symmetry properties of the QCD Lagrangian to observables by low-energy theorems. Being an effective field theory, the unknown structure of the theory at short distances is parametrised by so called low-energy constants (LECs) to be taken from experiment [111–115].

The mass of a pseudoscalar meson is given by the average (current) mass of the quark–antiquark pair and the matrix element of the pair between QCD vacuum states $B \cdot F_\pi^2 = \langle 0|\bar{q}q|0\rangle$, where F_π is the pion decay constant. For the case of pions the Gell-Mann–Oakes–Renner relation reads [346]

$$m_\pi^2 = \tfrac{1}{2}(m_u + m_d)|\langle 0|\bar{q}q|0\rangle|/F_\pi^2 + \text{higher orders.} \tag{7}$$

The constant B—the chiral condensate, equal for all pseudoscalar mesons—adjusts the physical masses of the pseudoscalar octet [112, 113, 116]. Though principally calculable within lattice QCD, precise numerical values for B and F_π are still derived from experiment. Similarly, sigma terms are measures of the chiral symmetry breaking. They are basically the product of current quark masses and densities given by $\langle hadron|\bar{q}q|hadron\rangle$ matrix elements between $hadron$ states evaluated in the limit of vanishing quark masses and momentum transfer. The sigma terms are related to the $\bar{s}s$ contents of meson or nucleon [117, 118] and, hence, probe the non-valence quark part, e.g., of the nucleon wavefunction. Located outside the physical region, sigma terms are not directly accessible by experiment, but they can be connected to hadron–hadron amplitudes by extrapolation into the unphysical region [118, 119]. Hence, scattering lengths are of great importance because they represent the closest approach in the *real world*.

3.1. Nucleon–antinucleon

At present ab initio calculations in the framework of non-perturbative QCD are limited to special cases [120–125]. Therefore, a potential must be constructed from symmetry considerations and plausible ad hoc assumptions.

Symmetries conserved in the strong interaction allow one to derive the real part of the antinucleon–nucleon potential including its spin dependence in the framework of *meson-exchange* models from the nucleon–nucleon interaction. At medium and long range, the real part of the $\bar{\text{N}}$N potential is directly obtained by the so-called *G-parity* transformation [126] from the NN potential [123, 127–131]. For the short distance a phenomenological short-range part is commonly used. In most cases the *Paris* potential is applied [128, 129, 132] (*Dover–Richard* potential). At low energies, it is sufficient to include the lightest mesons π, ρ, and ω and the non-resonant $2\pi(\sigma)$ and $3\pi(\epsilon)$ exchange for a proper description of the scattering cross section. The low-energy $\bar{\text{N}}$N interaction was recently reviewed by Klempt et al. [16].

For $\bar{\text{N}}$N, a strong annihilation to mesonic final states occurs, which is of short range and may change considerably the predictions based on the real part of the potential and hence the level shifts in $\bar{p}$H (Fig. 9). In addition strong distortions of the Coulomb wavefunctions are expected, which has a significant effect on the ratios of branching into meson final states [121, 122, 133–135]. The annihilation part of the potential is still best described by a phenomenological complex ansatz with a radial behavior close to the matter distribution (e.g., a Wood–Saxon distribution).

The *G-parity* transformation yields totally different shapes for the real part of the NN and $\bar{\text{N}}$N potential. Simplified, the strongly repulsive part of the NN potential (mainly from ω exchange) changes into strongly attractive in the $\bar{\text{N}}$N case. Spin–orbit forces in the $\bar{\text{N}}$N interaction are rather weak, whereas spin–spin forces are strong in contrast to the NN interaction [128]. Consequently, knowledge from individual hyperfine states is essential to discriminate between various theoretical approaches. In the case of hydrogen, the detection of Lyman or Balmer transitions makes sure that the antiproton–proton system ends in a pure 1s or 2p state, respectively.

Because of the small proton–neutron mass difference the coupling of the $|\bar{p}\text{p}\rangle$ to the $|\bar{n}\text{n}\rangle$ state, e.g., by pion exchange, has to be considered [136, 137]. Including the $|\bar{n}\text{n}\rangle$ component yields a dramatic effect for the hadronic broadening of the $^3\text{P}_0$ hyperfine state in protonium. It is predicted to increase by a factor of about 2, which can be traced back to a strongly attractive isoscalar tensor interaction [97, 128, 138, 139]. At short distances, where annihilation takes place, the isospin content of the final state is significantly changed by the charge-exchange potential. The $^3P_0$ state is predicted to be almost pure isospin 0 and not a half–half configuration $|\bar{p}p\rangle = \frac{1}{2}\sqrt{2}(\psi_0 + \psi_1)$ of $I = 0$ and $I = 1$ states as for the $|\bar{p}p\rangle$ approximation [138–140]. Such an isospin mixing, however, could not be confirmed from the study of branching ratios of meson final states, which indicates a sizeable isovector component [141]. A possible explanation may come from the fact that annihilation from atomic states and into meson final states probes the interaction at different distances. Atomic widths describe more the peripheral part, whereas annihilation, especially into heavier mesons, must be of very short range, where pion exchange plays a minor role.

Annihilation is very strong, which is illustrated by the short mean free path of 1.2 nucleon diameters of antiprotons in nuclear matter (black sphere) [136, 142, 143]. Therefore, the black-sphere model is able to describe reasonably the hadronic width for nuclei $A \geq 4$ by using the $\bar{N}N$ annihilation cross section [144]. Consequently, annihilation is a peripheral process except for the lightest nuclei, but can in turn be used to probe the nuclear halo [145, 146]. The distortions of atomic wavefunctions are significant in the presence of such a strong annihilation and, as mentioned before, are crucial in the calculations of branching ratios for the numerous mesonic final states. Therefore, much effort went into the calculation and quality of realistic wavefunctions. Shifts and broadenings of the atomic levels explicitly test the medium- and long-range part of the interaction at threshold and involve all final states [97, 128, 129, 139].

Low-energy scattering experiments provide complementary access to the scattering lengths by extrapolation to threshold [147–150]. The results must be consistent with the ones from exotic-atom data. Any disagreement between the methods of effective range theory and exotic-atom data indicates either an incompleteness of the physical processes taken into account or necessitates a check of the experimental and theoretical methods.

An anomalous threshold behavior could be evidence for exotic $\bar{N}N$ bound states close to threshold. Such objects have been considered in the framework of quark models to be “meta-stable” quark–antiquark combinations with or without gluon admixture [151, 152]. Potential models predict such bound states (“baryonium”) because of the strongly attractive short-range $\bar{N}N$ interaction, which may show up in an enhanced p-wave annihilation [128, 153–157].

3.2. *Kaon–nucleon*

Like the $\bar{N}N$ system the kaon and nucleon are composed of $I = 0$ and/or $I = 1$ isospin states. The scattering length reads $\mathbf{a_{K^-p}} = (\mathbf{a_0} + \mathbf{a_1})/2$ and the individual isospin components may be determined by fits to data from several kaonic atoms with a different composition of the nucleus [158]. Ideally, the individual components are determined by combining kaonic hydrogen and deuterium, but to date no measurements on kaonic deuterium have been performed (see Section 7). The scattering length in kaonic deuterium is given by $\mathbf{a_{K^-d}} = \frac{1}{2}\left(\frac{1+m_K/M}{1+m_K/M_d}\right)(\mathbf{a_0}+3\mathbf{a_1})+C$, where the kinematic factor is due to shift from the KN to the Kd center of mass.[5] The three-body corrections are sizable and involve

---

[5] M and M_d denote the proton and deuteron mass, respectively.

large imaginary parts due to the inelastic KN channels, which complicates the description of the K^-p interaction at low energies.

Close to threshold the isospin 0 $\Lambda(1405)$ and isospin 1 $\Sigma(1385)$ resonances exist. The nature of the $\Lambda(1405)$ particle is still poorly understood [159]. Its mass is only 26 MeV/c^2 below the K^-p threshold (and even closer in the case of helium because of the large binding energy) and has a lifetime of about 50 MeV decaying exclusively into the $\Sigma\pi$ channel [34]. Such a situation usually requires a more sophisticated approach such as coupled channels [160–162]. Primarily the $I = 0$ amplitude may then change rapidly with energy because of the nearby resonance [163, 164].

The importance of the KN interaction at threshold is due to the possibility of testing χPT for systems involving the "heavy" light quark s. Low-energy theorems have to be worked out in the framework of (χPT) using constraints from coupled channel techniques [165, 166].

3.3. *Pion–nucleon*

According to its origin, the methods of χPT work best for the lightest quarks u and d as combined in the lightest strongly interacting particle—the pion. Therefore, the pion–pion interaction [113] is regarded to be the best testing ground for non-perturbative QCD. Unfortunately, experimental circumstances prevent a determination of the $\pi\pi$ scattering length to the few per cent level [167–169], which would be required for a decisive test of the theory [170–173].

It has been shown that such an effective field-theory approach can also be applied to the meson–nucleon case labeled *heavy-baryon chiral perturbation theory* (HBχPT), where a special transformation bypasses the problem of the non-vanishing nucleon mass in the *chiral limit* $m_{\text{quark}} \rightarrow 0$ [113, 174, 175]. The chiral expansion, ordered by counting the powers of (small) momenta, the quark-mass difference $(m_d - m_u)$, *and* the fine structure constant α [111], allows one to include on the same footing the strong isospin breaking effects based on the mass difference $(m_d \neq m_u)$ and those of electromagnetic origin [176–179].

In the case of πN, the two basic parameters at threshold are the isoscalar and isovector s-wave scattering lengths a^+ and a^-. They are given in terms of the elastic reactions by

$$a^{\pm} = \tfrac{1}{2}(a_{\pi^-p\to\pi^-p} \pm a_{\pi^+p\to\pi^+p}) \qquad (8)$$

or when expressed in terms of the two possible isospin combinations $I = 1/2$ and $I = 3/2$ by

$$a^{+} = \tfrac{1}{3}(a_{1/2} + 2a_{3/2}) \qquad (9)$$

$$a^{-} = \tfrac{1}{3}(a_{1/2} - a_{3/2}). \qquad (10)$$

If isospin conservation is exactly fulfilled, the elastic channels are related to charge exchange by

$$a_{\pi^-p\to\pi^-p} - a_{\pi^+p\to\pi^+p} = -\sqrt{2}a_{\pi^-p\to\pi^\circ n}, \qquad (11)$$

i.e., the strong πN interaction at threshold is described completely by two (real) numbers.

The leading order result for a^+ and a^- derived from current algebra [180, 181] already revealed an important feature of the underlying symmetry—the vanishing of the isoscalar combination a^+ in the chiral limit:

$$a^+ = 0 \tag{12}$$

$$a^- = -0.079/m_\pi \tag{13}$$

a^+ further on remains small also when higher orders are taken into account [177] (Fig. 16).

A fundamental quantity of the πN interaction, the πN coupling constant $f^2_{\pi \mathrm{N}}$, is connected to the isovector scattering length a^- by current algebra and dispersion relation theory through the Goldberger–Miyazawa–Oehme (GMO) sum rule [182]. If isospin symmetry holds, the GMO sum rule directly relates $\Gamma_{1\mathrm{s}}$ to $f^2_{\pi N}$ (Eqs. (11) and (17)):

$$\left(1+\frac{m_\pi}{M}\right)\frac{a^-}{m_\pi} = \frac{2f^2_{\pi \mathrm{N}}}{m^2_\pi - (m^2_\pi/2M_N)^2} + \frac{1}{2\pi^2}\int_0^\infty \frac{\sigma^{\mathrm{tot}}_{\pi^- \mathrm{p}}(k_\pi) - \sigma^{\mathrm{tot}}_{\pi^+ \mathrm{p}}(k_\pi)}{\omega(k_\pi)} dk_\pi . \tag{14}$$

At present, the value of the integral is known with an accuracy of about 1% [183–185]. The leading order result for $f^2_{\pi \mathrm{N}}$, derived within current-algebra, is known as the Goldberger–Treiman relation: [18, 186].

$$\frac{f^2_{\pi \mathrm{N}}}{4\pi} = \frac{m^2_\pi g^2_A}{16\pi F^2_\pi} = \frac{m^2_\pi}{4M^2}\frac{g^2_{\pi \mathrm{N}}}{4\pi} = 0.072. \tag{15}$$

The relation between $f^2_{\pi \mathrm{N}}$, the pion decay constant F^2_π, and the axial vector constant g_A, determined from neutron decay, demonstrates the connections between strong forces, QCD vacuum, and weak interaction. M and m_π denote the proton and the charged-pion mass by convention. The deviation from the value of 0.072 is again directly related to higher orders in the chiral expansion (Goldberger–Treiman discrepancy). The order of magnitude of the discrepancy is about 2–4% [187].

Nowadays, up to fourth-order calculations in the framework of HBχPT have been performed [188]. Consequently, the experimental information obtained from the hadronic shift $\epsilon_{1\mathrm{s}}$ and level broadening $\Gamma_{1\mathrm{s}}$ of the atomic ground state in the pionic hydrogen should at least reach a precision at that level. Expressed in a Deser-type formula [189], the relation between exotic-atom parameters and scattering lengths may be written as[6]

$$\frac{\epsilon_{1\mathrm{s}}}{B_{1\mathrm{s}}} = -\frac{4}{r_\mathrm{B}} a_{\pi^-\mathrm{p}\to\pi^-\mathrm{p}}(1+\delta_\epsilon) \tag{16}$$

$$\frac{\Gamma_{1\mathrm{s}}}{B_{1\mathrm{s}}} = 8\frac{q_0}{r_\mathrm{B}}\left(1+\frac{1}{P}\right)[a_{\pi^-\mathrm{p}\to\pi^0 n}(1+\delta_\Gamma)]^2. \tag{17}$$

Obviously $\epsilon_{1\mathrm{s}} \propto a^+ + a^-$ and, assuming isospin invariance, $\Gamma_{1\mathrm{s}} \propto (a^-)^2$ holds.

The parameters $\delta_{\epsilon,\Gamma}$ prevent a direct extraction of the pure hadronic scattering length from the experimental results. They account both for nuclear–Coulomb interference and terms arising from the chiral expansion treating electromagnetic corrections and isospin

---

[6] $q_0 = 0.1421\ \mathrm{fm}^{-1}$ is the center-of-mass momentum of the π^0 in the charge-exchange reaction $\pi^-\mathrm{p} \to \pi^0\mathrm{n}$ and $P = 1.546 \pm 0.009$ [190] the branching ratio of charge exchange and radiative capture (Panofsky ratio).

breaking effects. The LECs contained in the higher-order terms of the chiral expansion [178, 191] have to come from experiment and not all of them are well known. These corrections are of the order of a few to several per cent and are at present the subject of detailed theoretical studies [178, 179, 183]. Older results, based on a potential approach [192], are assumed to underestimate both the magnitude and the uncertainty of $\delta_{\epsilon,\Gamma}$ [179].

An important independent source of information for a^+ is the ground-state shift ϵ_{1s} of pionic deuterium, which is proportional to the real part of the pion–deuteron scattering length $\Re a_{\pi d}$ according to the Deser formula. Assuming charge symmetry, i.e., $a_{\pi^+ \mathrm{p}} = a_{\pi^- \mathrm{n}}$, the sum (difference) of the free π^-p and π^-n scattering lengths exactly yields the isoscalar (isovector) combination $a^+ (a^-)$. To profit from the precise results for the deuterium ground-state shift, $\Re a_{\pi d}$ must be resolved in the framework of a multiple-scattering approach [18]. Because of the smallness of a^+ compared to a^-, the double-scattering term D dominates over the single-scattering contribution S by an order of magnitude:[7]

$$\begin{aligned}\Re a_{\pi d} &= S + D + \cdots \\ &= \frac{1 + m_\pi/M}{1 + m_\pi/M_d} a^+ \\ &\quad + 2\frac{(1 + m_\pi/M)^2}{1 + m_\pi/M_d}\left[\left(\frac{a^+}{2}\right)^2 - 2\left(\frac{a^-}{2}\right)^2\right]\langle 1/r\rangle + \cdots . \end{aligned} \tag{18}$$

Evidently, like for the Kd case, an elaborate multi-body calculation is mandatory for the precise determination of a^+ [184, 185, 193].

4. Experimental techniques

High-resolution spectroscopy of X-rays from exotic atoms demands the maximization of the X-ray count rate *simultaneously* with an adequate resolution. Semiconductor detectors, used for the direct measurement of the radiation emitted from a target volume, usually cover a few per mill of the solid angle. The efficiency of an ultimate-resolution device such as the crystal spectrometer described here is another two to three orders of magnitude smaller. This requires:

- Highest possible yields of the exotic-atom X-ray transitions, for which in general dilute targets are needed.
- High stop densities, i.e., small stop volumes in the dilute targets, to overcome the low efficiency of high-resolution semiconductor detectors or crystal spectrometers.
- Efficient background suppression to handle the high background level in particle-accelerator environments.

Such conditions are achieved in an experimental set-up combining the *cyclotron trap*, a *focussing low-energy Bragg spectrometer*, and CCDs for X-ray detection (Fig. 3).

---

[7] $\langle 1/r\rangle$ is the inverse deuteron radius.

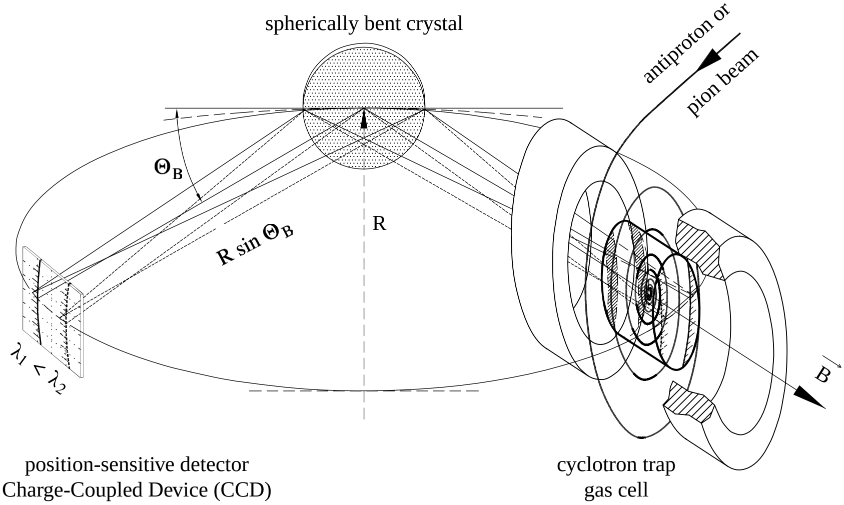

Fig. 3. The experimental approach for a crystal spectrometer experiment. The focussing Bragg spectrometer is equipped with spherically bent crystals and two-dimensional position-sensitive detectors. The diameter R of the Rowland circle is equal to the (horizontal) radius of curvature of the crystal. The X-ray source is provided by a particle concentrator—the cyclotron trap.

4.1. Cyclotron trap and X-ray source

In the cyclotron trap the range curve of the particle beam is wound up in a weakly focussing magnetic field, which is produced by a superconducting split-coil magnet [194]. Between the coils a target chamber is installed containing a suitable degrader arrangement. Entering the target chamber, the beam is degraded immediately to a momentum of about 65 MeV/c to be trapped in the magnetic field. Further on, the particles lose their kinetic energy first in additional degraders and then in the target gas itself, thus approaching the center of the magnet on spiral orbits. Different scenarios exist (Table 4):

- Stable particles such as **antiprotons** can be decelerated slowly. The low-emittance beam of LEAR was stopped almost completely in a few cm^3 at very low pressures.
- Because of the **pion's** short lifetime, the beam must be stopped within a few ns. The fast deceleration by rather thick degraders requires an additional gas cell in the center of the trap. In this way a concentrated and radially homogeneous X-ray source is obtained.
- At pion beams **muonic atoms** are formed when slow pions decay close to the target cell. The use of the decay muons permits the simultaneous measurement of pionic and muonic transitions.

With the cyclotron trap, a gain in stop density over a linear arrangement is achieved by factors of 10^6 and 200 for antiproton and pion beams, respectively.

Table 4
Exotic-atom X-ray sources achievable with the cyclotron trap. ϕ_{source} and l_{axial} are the extensions perpendicular and along the symmetry axis of the magnet

	p_{beam}/MeV/c	Intensity/s	Target	Pressure/mbar	f_{stop}%	$\phi_{\text{source}} \times l_{\text{axial}}$/mm × mm
$\bar{p}$	105	10^6	H_2	20	≈90	20 × 30 FWHM
π^-	110	10^9	N_2	1000	≈2	60 × 40 gas cell
μ^-	From π decay		O_2	1000	≈0.1	60 × 150 gas cell

4.2. *Crystal spectrometer*

When X-rays are scattered off the electrons of atoms, arranged regularly in lattice planes having the distance d, according to Bragg's law

$$n\lambda = 2d \cdot \sin \Theta_B, \tag{19}$$

a coherent superposition for one wavelength λ occurs only close to the Bragg angle Θ_B, where n is the order of reflection. The theoretical limit for the energy resolution is given by the width ω_f at FWHM of the angular distribution of a parallel beam reflected by a perfect plane crystal (rocking curve).

For X-radiation below 20 keV energy, because of the absorption losses, reflection-type crystal spectrometers are normally used. In the few keV range, quartz or silicon are the only materials suitable for ultimate-resolution studies. These are ideal crystals and their reflection properties can be calculated reliably from the dynamical theory except in the close vicinity of absorption edges [195, 196]. The intrinsic resolution ω_f of perfect plane crystals is in the range $\Delta E/E = 10^{-5}$–10^{-4} (Table 5).

For the investigation of broad X-ray lines or multiplets, cylindrically bent crystals are widely used (Johann geometry [197]), because in this case an energy interval corresponding to the width of the source can be recorded simultaneously with position-sensitive detectors. For X-rays reflected at the Bragg angle Θ_B the focussing condition in the direction of dispersion is fulfilled on the Rowland circle at the distance $R \cdot \sin \Theta_B$ (Fig. 3).

Spherically bent crystals in addition have (angle-dependent) focussing properties in the vertical direction, perpendicular to the direction of dispersion, which reduces the height of the image [198]. This allows an efficient use of rather small pixel detectors such as CCDs. The two-dimensional position information permits correction for the curvature of the reflection [199, 200].

4.2.1. *Resolution*

As a consequence of crystal bending, a decrease in resolution owing to the finite size of the crystal and source must be accepted. For the experiment, a compromise between count rate and aberration has to be achieved. In the set-ups described here, aberration is mainly due to the (full) *horizontal* extension b of the crystal. It causes a shift, which depends on the absolute value of the Bragg angle and always reduces the reflection angle in relation to the central ray (Fig. 3). The maximum angular shift $\Delta\Theta_J$, for X-rays reflected from the left or

Table 5
Calculated and measured resolutions ΔE_{cal} and ΔE_{exp} (FWHM) of the crystal spectrometer. The radiative widths Γ_X of the exotic-atom transitions are negligibly small compared to the intrinsic resolution ω_f (FWHM of the rocking curve). The crystal parameters are given as calculated with the code of Brennan and Cowan for plane crystals [196] and the code XOP [206]. The resolution achievable with the bent crystal spectrometer is obtained by convolution of the rocking curve with imaging properties of the set-up

	E_{QED}/eV	Γ_X/meV	Reflection	w_f/meV	ΔE_{cal}/meV	ΔE_{exp}/meV
$\bar{p}\,^3$He(5g–4f)	1686.477	0.26	qu 100	129	150	285 ± 8
$\bar{p}\,^{20}$Ne(13p–12o)	2444.035	10	Si 111	272	320	333 ± 34
$\pi\,^{20}$Ne(7i–6h)	2718.751	4.2	Si 111	348	400	478 ± 29
$\pi\,^{12}$C(5g–4f)	2973.826	4.4	quartz $10\bar{1}$	402	425	477 ± 26
$\pi\,^{20}$Ne(6h–5g)	4509.894	11	Si 220	265	460	550 ± 17
$\pi\,^{20}$Ne(5g–4f)	8306.449	32	Si 440	72	300	725 ± 32

right boundary of the crystal, is given in leading order for both cases by

$$\Delta\Theta_J = 1/2(b/2R)^2 \cdot \cot^2 \Theta_B. \tag{20}$$

Hence, an angle-dependent (asymmetric) broadening and a shift of the reflection towards higher energies appear (Johann broadening and shift) [198, 201]. Further corrections necessary to achieve the “true” Bragg angle for calculating the wavelength are due to the change of the refraction index for the radiation inside the crystal (index of refraction shift) [196, 202] and the penetration depth, which is sensitive to distortions of the lattice constant from the bending [203]. More details may be found in [86, 204].

In theory the resolution of a bent crystal is given by the convolution of the rocking curve and the geometrical broadening. However, forcing a disk into a sphere is in principle impossible without causing non-linear distortions. In addition at low energies, lattice distortions at the surface due to polishing become important. To exclude volume effects on the uniformity of the bending, the crystal disks of 0.3 mm thickness were mounted on glass lenses of high quality by optical contact [86, 204]. For bending radii of $R = 3$ m and crystal diameters of 100 mm the measured resolutions approach the theoretical values in the majority of cases to closer than a factor of 2 (Table 5).

Exotic-atom transitions not affected by strong interaction or screening by remaining electrons have much smaller natural linewidths Γ_X than fluorescence X-rays (Figs. 6 and 11, Table 6). Though beam time consuming, these transitions are currently the only possibility for determining the spectrometer response function in a comparable geometry (Fig. 5—*left*). Narrow nuclear γ-rays with sufficient intensity are not available in the few keV range for practical cases. Hydrogen-like electronic atoms may help to solve this problem in the future (Section 7.2).

4.2.2. Energy and efficiency calibration

Semiconductor detectors. The method of saturated X-rays in dilute targets allows an in-beam energy and efficiency calibration. Selected low- and medium-Z exotic atoms are depleted completely from electrons in the medium part of the atomic cascade. Energies are given with the precision of calculation. The relative efficiency is determined from the line

Table 6
Fluorescence X-rays and exotic-atom transitions used for energy calibration. The calibration was applied to the transitions given in the last column. The Bragg angles are given without the index of refraction shift

Calibration	E/keV	Γ_X/meV	Reflection	Θ_B	Transition
Si Kα_1	1739.986 ± 0.019	524 ± 35	qu 100	$56°50'53.7''$	$\bar{p}$H(3d–2p)
S Kα_1	2307.886 ± 0.034	769 ± 26	Si 111	$58°56'40.0''$	$\bar{p}$D(3d–2p)
Cl Kα_1	2622.441 ± 0.039	925 ± 86	Si 111	$48°55'45.2''$	πD(2p–1s)
Cu Kα_1	8047.838 ± 0.006	2260 ± 20	Si 440	$53°21'10.0''$	πN(5g–4f)
πO(6h–5g)	2880.506	4	Si 111	$43°20'34.0''$	πH(3p–1s)
μO(5g–4f)	4023.997	10	Si 220	$53°20'52.0''$	πN(5g–4f)

intensities, which all have about the same absolute yield in dilute gases (Fig. 5—*right*). The absolute efficiency is obtained by a calibrated radioactive source within the used energy range. An important feature of this method is that it can be extended to lower energies than are available from common calibrated radio-active sources.

Crystal spectrometer. An absolute determination of the Bragg angle from the measured position on the X-ray detector is considered to be impossible for the required accuracies up to 1 ppm. Therefore, relative measurements are performed using radiation of well-known wavelength and close in energy to the transition to be studied. For small angle differences, the higher-order corrections to the Bragg angle are well under control and possible uncertainties in the lattice distance have no effect. Two different cases occur:

- The angle difference between the calibration line and the transition under investigation is small enough for measuring both lines simultaneously as indicated in Fig. 3. The position difference directly yields the energy difference if $R \cdot \sin \Theta_B$ is sufficiently well known. This method rules out systematic errors regarding long-term stability.
- If the angle difference exceeds the size of the source or detector, the crystal is rotated so that the two reflections appear at the same position on the detector and the spectrometer is readjusted to the source. The rotation of the crystal is measured with a high-precision angular encoder ($\Delta\Theta = \pm 0.15$ s of arc or ± 0.5 ppm).

At present two sets of calibration lines are available (Table 6):

- **Fluorescence X-rays.** Among others, the Kα lines from silicon, sulphur, chlorine [207, 208], argon [208, 209], and copper [210] have been re-measured recently with improved precision to be used for calibration purposes. However, the large natural linewidths, the presence of satellite transitions originating from multiple ionisation, and line splitting due to the coupling of vacancies (see Section 6.4) limit the accuracy to a few ppm when relating the peak position to the wavelength. For low-Z atoms, the analysis is also complicated by the incomplete separation of the doublet (Figs. 6 and 11).
- **Exotic X-ray transitions.** Suitable calibration lines from exotic atoms are rare because sufficient yields are achieved only for a few elements in the medium and lower part of the atomic cascade. Again, the transitions must not be affected by

electron screening or strong interaction to make use of the precise QED calculations, which nowadays reach an accuracy of a few meV [211].

4.3. X-ray detectors

CCDs are ideally suited for low-energy X-ray detection in a high-background environment because of their distinguished two-dimensional position resolution together with the excellent energy resolution of semiconductor devices [212–217]. Charge created by the short-range photo-electron from conversion of the X-ray quantum is deposited in one or two pixels only, whereas particle- or Compton-induced events produce larger clusters (Fig. 7). The pixel structure of the CCDs allows an almost complete separation of X-ray and background events by the analysis of the hit pattern (cluster analysis) when the fraction of hit pixels is kept below a few per cent (Fig. 6).

For the direct measurement of exotic-atom X-rays the CCDs were placed close to the stop volume inside one bore hole of the magnet of the cyclotron trap (Fig. 4). Due to the background suppression achieved with the position information, the performances of CCDs are superior to those of conventional semiconductor detectors. Used as focal-plane detectors of the crystal spectrometer, the CCDs can be shielded from the direct radiation of the source. In that way, for extremely small count rates also almost background-free spectra are obtained (Fig. 6). The CCDs used so far, however, are not triggerable, which limits their rejection capability if the background is dominated by low-energy electromagnetic radiation.

4.4. Linear stop arrangement and triggered X-ray detectors

Currently available kaon beams suffer from low kaon fluxes and simultaneously a large contamination with pions. In order to achieve reasonable background conditions, a trigger condition is imposed on X-ray recording. The kaonic hydrogen experiment, set up at the low-energy separated beam line of the KEK proton synchrotron (Japan), used a linear arrangement to stop kaons in a cryogenic hydrogen target [218, 219].

Up to 60 X-ray detectors placed inside the gas volume were used to achieve a maximum solid angle (Fig. 8). Background suppression was performed by tagging on two fast coincident charged pions originating from the branch $K^-_{\mathrm{stop}}p \rightarrow \Sigma^{\pm}\pi^{\mp}$ followed by $\Sigma^{\pm} \rightarrow n\pi^{\pm}$ decay, which occurs in about 50% of all reactions. Vertex reconstruction with multiwire proportional chambers ensured that the pions were created inside the hydrogen target. A sharp timing was achieved by scintillation counters. In this way a background rejection of almost three orders of magnitude was achieved in face of a π/K ratio of 90.

5. Strong-interaction results

5.1. Antiprotonic hydrogen

5.1.1. 1s ground state

In a first generation of LEAR experiments, X-rays from $\bar{p}$H and $\bar{p}$D were detected by using conventional semiconductor and gas-filled devices. An accuracy of 3% and 6% was achieved for the spin-averaged shift ϵ_{1s} and broadening Γ_{1s} (experiments PS174

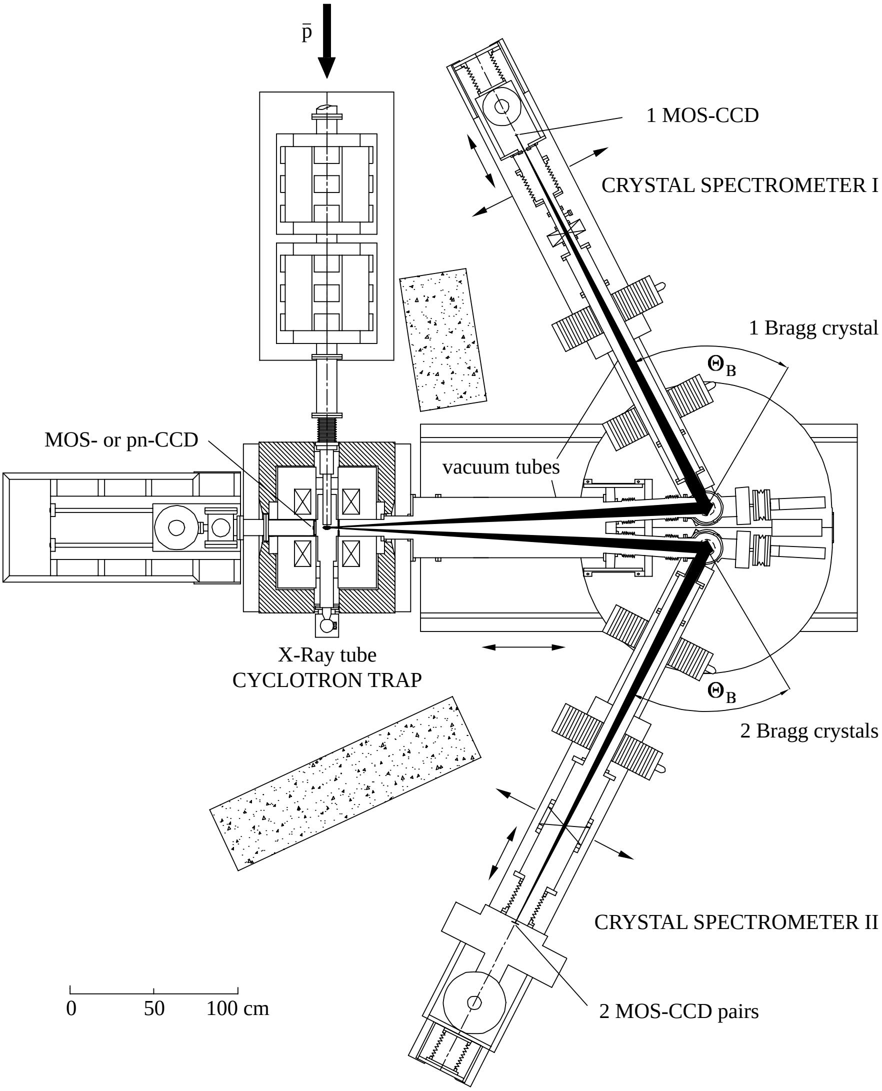

Fig. 4. The set-up of the cyclotron trap, crystal spectrometer, and CCD detectors for the measurement of antiprotonic hydrogen (LEAR experiment PS207) [86, 205]. The Bragg spectrometer was equipped with three independently adjustable spherically bent quartz crystals. Each crystal was directed to its own CCD detector to avoid any reduction of resolution from a matching of reflections. CCDs for the direct measurement of X-rays were mounted in the second bore hole close to the stop volume.

[90, 220] and PS175 [62]). A first glance at the spin dependence (Fig. 9) was obtained from results of the experiments PS171 by tagging X-rays with neutral final states [221] and PS175 by using a high-resolution Si(Li) detector [62] for the $^1S_0$ and $^3S_1$

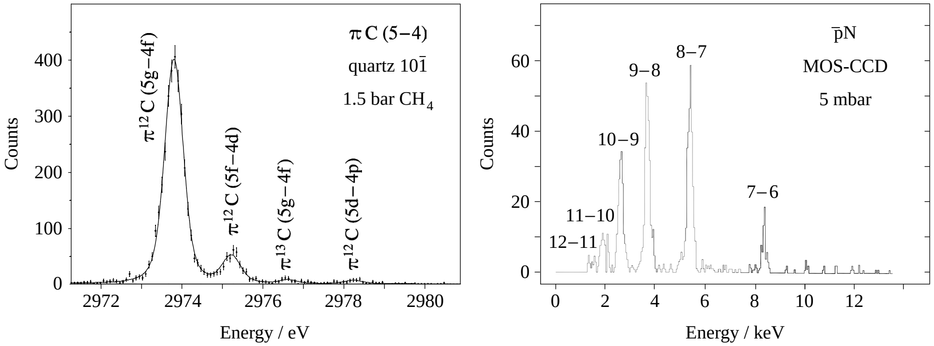

Fig. 5. *Left*: Measurement of the crystal spectrometer response function with the narrow πC(5g–4f) transition. *Right*: Simultaneous in-beam energy and relative efficiency calibration of a MOS CCD with saturated line yields in $\bar{p}$N.

hyperfine states, respectively, which could, however, be obtained only with additional assumptions.

The situation was improved by a measurement with higher statistics using CCDs [222–224]. For the first time the hadronic shift and broadening of both hyperfine components $^3S_1$ and $^1S_0$ were determined from one single spectrum (Fig. 10). The still limited statistics, however, prevented the achieving of a comparable accuracy for the individual hyperfine components as for the spin average without additional constraints. The $\bar{p}$H data were fitted by using a background shape found in the $\bar{p}$D experiment and including further constraints on the $\bar{p}$Be lines and fluorescence X-rays obtained from a $\bar{p}$N measurement. In addition, a contribution tentatively ascribed to inner Bremsstrahlung from annihilation [225] was introduced to achieve a satisfactory description of the background shape [223]. The two hyperfine components were represented by two Voigt functions. The fit did not allow a variation of all parameters at the same time. Therefore, the final fit for the hyperfine states was made by freezing the $\bar{p}$H background shape. Furthermore, to obtain all four strong-interaction parameters the $^3S_1/^1S_0$ intensity ratio had to be fixed to about 2, which is in accordance with the value suggested by the different widths of the 2p hyperfine levels (Table 9).

Spin-averaged strong-interaction effects are given in Table 7 together with typical results from optical model calculations based on meson exchange and a phenomenological annihilation potential. The theoretical approaches labeled DR1 and KW differ from each other slightly in the meson contents for the real part of the $\bar{\text{N}}$N potential, but more in the parametrisation of the absorptive part. The inclusion of decay channels into close-to-threshold $\bar{\text{N}}$N bound states also does not change significantly the values for the spin-averaged shifts and widths. For sensitivity to such details, a better decomposition of the hyperfine structure is necessary, which mainly has to come from a substantially improved statistics and, in addition, from a better knowledge of the background shape. The measurement of the $\bar{n}$p annihilation cross section at low energies by Mutchler et al. [226] yields an estimate on the pure $I = 1$ s-wave annihilation strength. Together with $\bar{p}$ atom data, the $I = 0$ part also becomes accessible (Table 8).

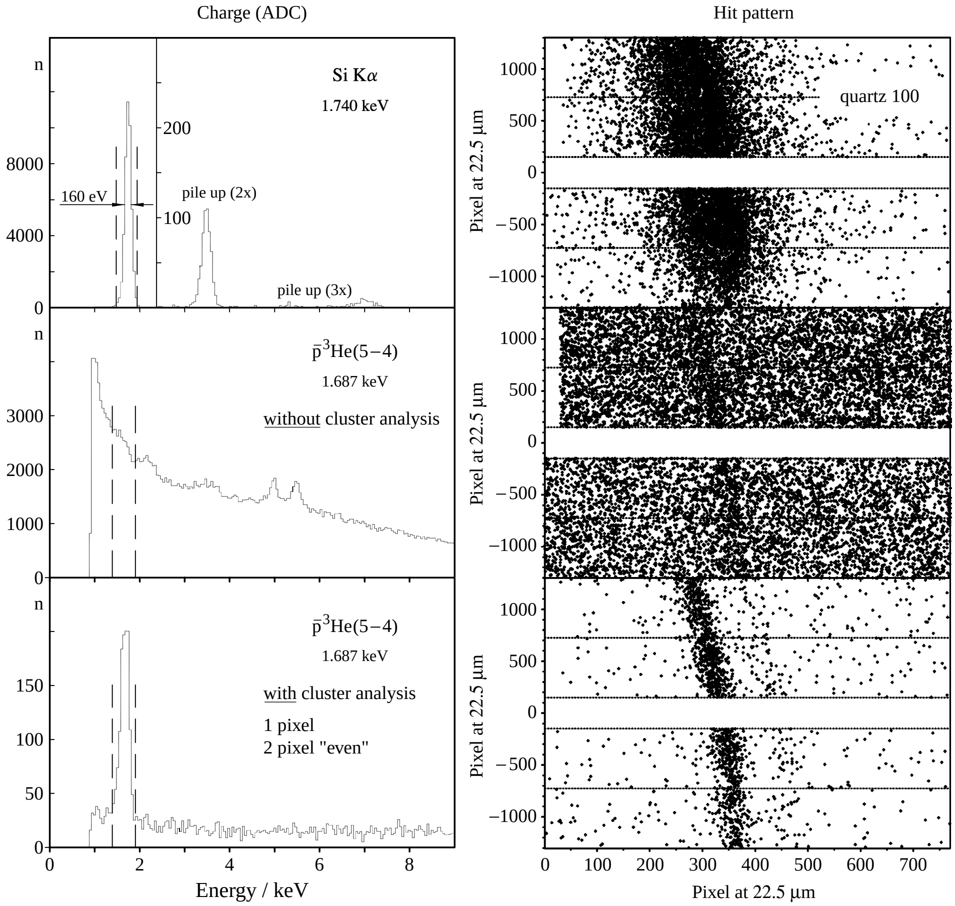

Fig. 6. Background suppression achieved with CCDs as the focal-plane detectors of the crystal spectrometer (from [86]). *Top*: The spectrum obtained with silicon Kα fluorescence radiation, excited by means of an X-ray tube, is background free. *Middle*: Raw data from the measurement of antiprotonic ^{3}He at LEAR (PS207). The vertical dashed lines indicate the energy range of the $\bar{p}^3$He(5–4) transition. *Bottom*: Background reduction by analysis of the hit pattern on the CCD. The rate of the circular transition $\bar{p}^3$He(5g–4f) is about 30 per hour; that of the parallel transition $\bar{p}^3$He(5f–4d) about one order of magnitude less. After correction for the curvature of the reflection, projection to the horizontal axis is equivalent to an energy spectrum (see also Fig. 11).

5.1.2. 2p state

The essential assumption for the analysis of the spectra measured with the crystal spectrometer is a statistical population of the 3d states, which is justified by the negligibly small annihilation from $l \geq 2$ states [139]. Hence the relative intensities of the hyperfine transitions can be fixed [86].

In antiprotonic hydrogen, the 2 $^3P_0$ hyperfine state plays a particular role. It is an indispensable prediction of the meson-exchange model that the electromagnetic splitting of about 200 meV should be increased by another 100 meV by the long-range $\bar{p}$p

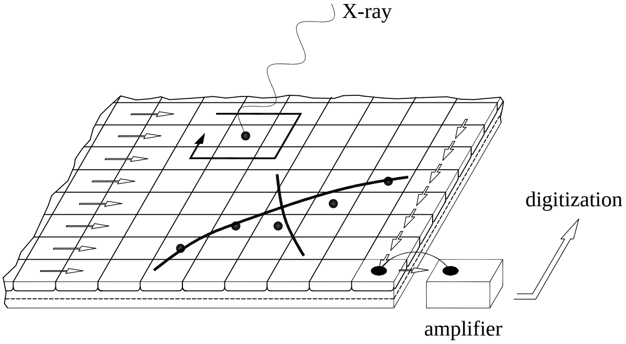

Fig. 7. Discrimination of low-energy X-rays and background by pattern recognition with a standard CCD. Few keV X-rays create charge only in a single or two adjacent pixels.

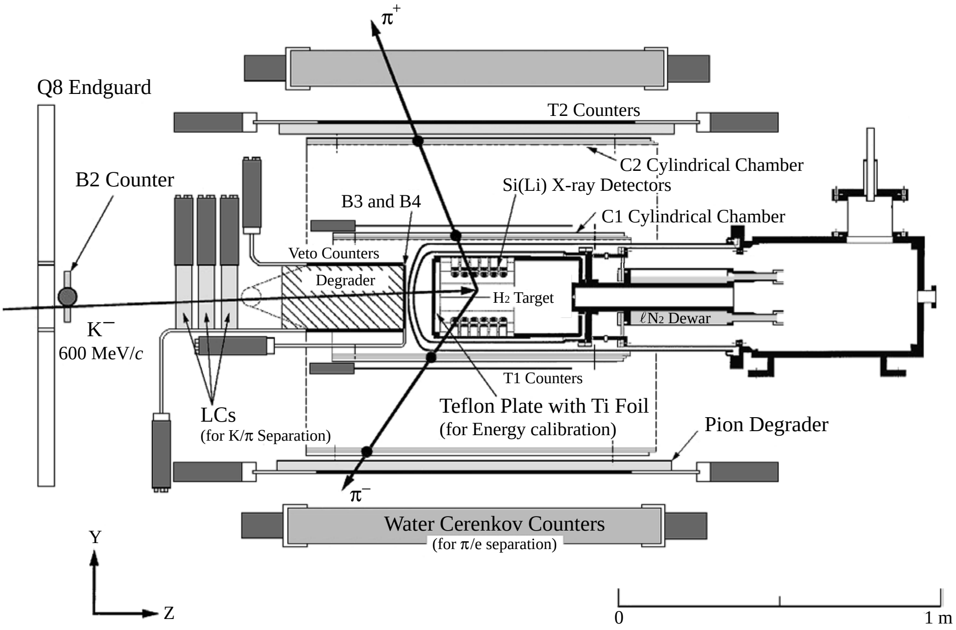

Fig. 8. The set-up of the kaonic hydrogen experiment at KEK (from [219]). Kaons are stopped in hydrogen gas cooled to 100 K at a pressure of 4 bar.

potential (Fig. 9). In fact, the shoulder on the high-energy side of the Balmer α line profile amounts to the expected statistical population of the $2\ ^3P_0$ hyperfine state. The close-lying components $2\ ^3P_2$, $2\ ^3P_1$ and $2\ ^1P_1$ are not resolved (Fig. 11). The value for the hadronic shift $\epsilon(2\ ^3P_0)$ even exceeds the results obtained from most of the theoretical calculations (Table 9). The broadening $\Gamma(2\ ^3P_0)$—much larger than the spin-averaged value—is in the

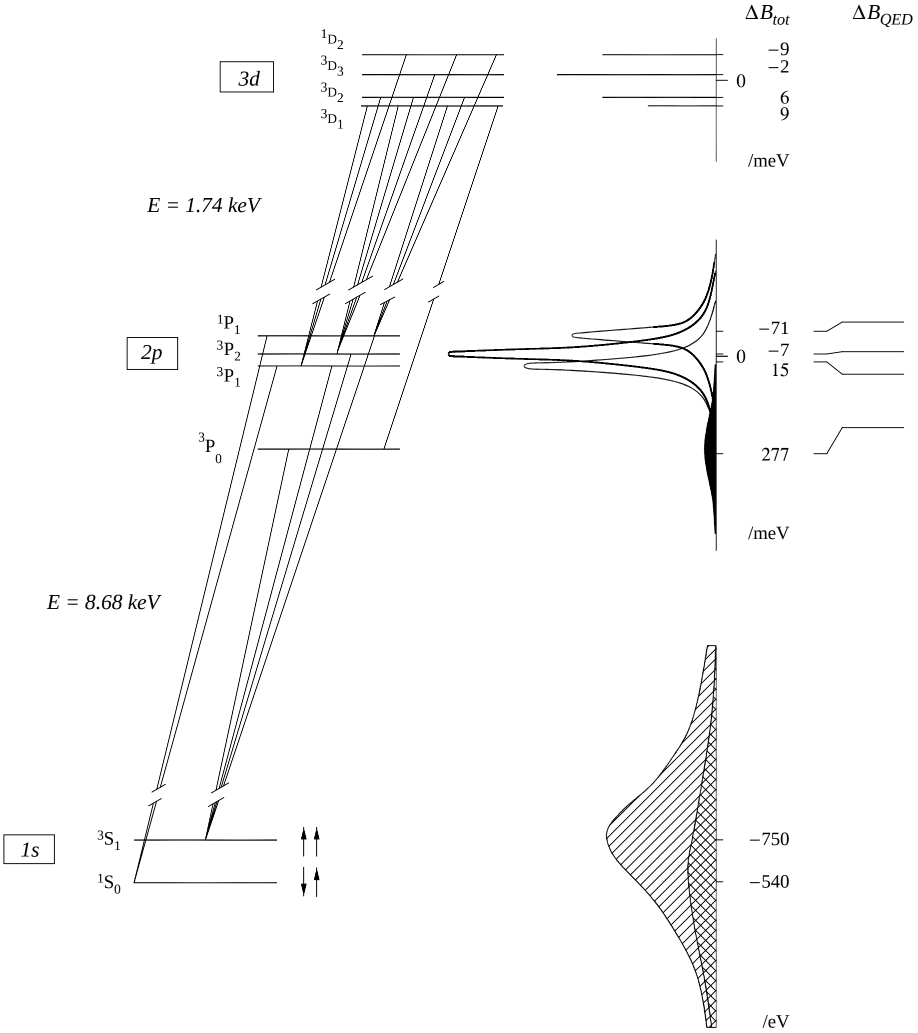

Fig. 9. Low-lying Lyman and Balmer α hyperfine transitions in antiprotonic hydrogen. ΔB_{tot} indicates the change of binding energy including the strong-interaction shift relative to the center of the multiplet as given by the pure electromagnetic interaction. The electromagnetic level energies and splittings are taken from a recent calculation of Boucard and Indelicato [211] (see Fig. 22). The hadronic contributions are predictions of Carbonell et al. obtained with the optical potential DR1 [139]. The pure electromagnetic hyperfine splitting of the *2p* state is indicated in the column ΔB_{QED}.

range of the predictions as are the measured mean shift and width of the group (2 $^3P_2$, 2 $^3P_1$, 2 $^1P_1$).

Obviously, the level structure originating from the real part of the hadronic potential is not destroyed by the very fast annihilation. The experimental results are considered as

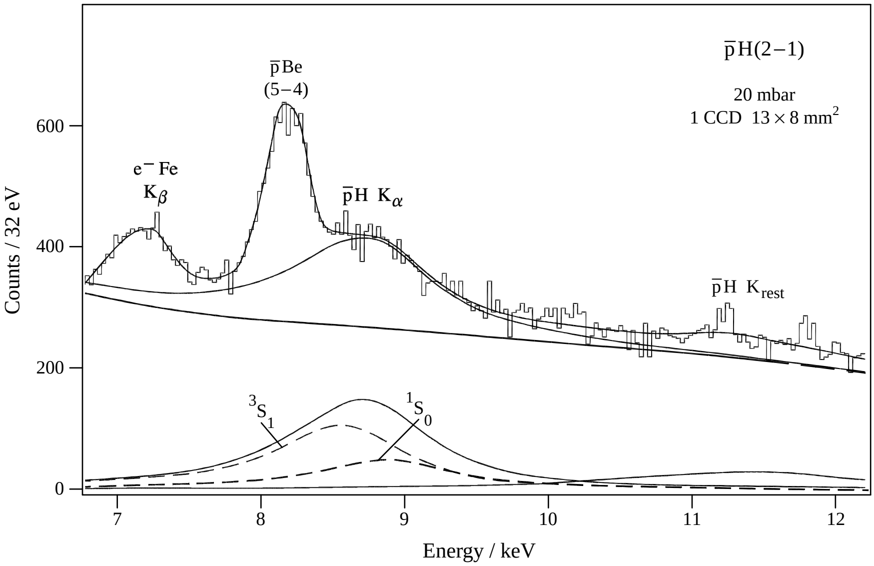

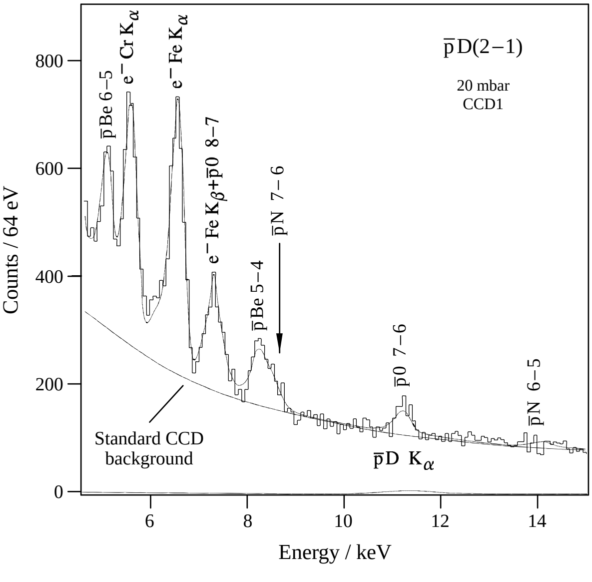

Fig. 10. X-ray spectra in the energy range of the $\bar{p}$H and $\bar{p}$D Lyman transitions measured at LEAR [222–224]. The electromagnetic 2p–1s transition energies of the hydrogen isotopes are 9.4 and 12.5 keV.

strong support for the validity of the meson-exchange models for the medium- and long-range real part. The outstanding strong p-wave interaction, in particular of the shift of the $2\,^3P_0$ state, may suggest discussing again close-to-threshold $\bar{N}N$ bound states [230].

Table 7
Spin-averaged hadronic shifts and broadenings in antiprotonic hydrogen and deuterium compared to theoretical predictions. The largest contribution to the error of ϵ_{2p} is due to the uncertainties in energy for the Kα lines of silicon and sulphur! The strong suppression of K transitions becomes obvious from the small radiative width Γ^X_{2p} compared to the hadronic broadening Γ_{2p}

	ϵ_{1s} /eV[a]	Γ_{1s} /eV		ϵ_{2p} /meV[a]	Γ_{2p} /meV		Γ^X_{2p} /meV
$\bar{p}$H							0.38
Experiment	-714 ± 14	1097 ± 42	[223]	$+15 \pm 20$	38.0 ± 2.8	[86]	
DR1	-707	933	[139]	$+6$	33.5	[139]	
KW	-698	1062	[139]	$+7$	35	[139]	
Eff. range	-600	1080	[147]	$+9$	39	[147]	
$\bar{\mathrm{N}}$N bound states	-730	≈ 1400	[156]	-18	36	[156]	
$\bar{p}$D							0.51
Experiment	-1050 ± 250	1100 ± 750	[224]	-243 ± 26	489 ± 30	[86]	
Geometrical scaling		2300 ± 300	[86]				
Mult. scatt.	≈ -4000	≈ 5500	[227]	-52	422	[227]	
3-body cal.	≈ -1600	≈ 1000	[228]				
Potential cal.	≈ -4000	≈ 2000	[229]				

[a] For the definition of the sign of ϵ see Fig. 1.

Without the crystal spectrometer results, only an average 2p-level broadening is accessible from the intensity balance between the total Balmer series and the Lyman α transition. This value, however, is equal to the spin-averaged hadronic width only in the limit of equal broadening for all 2p hyperfine levels [86]. Hence, the large value for $\Gamma(2\ ^3P_0)$ yields dramatic consequences. Whereas a value of $\Gamma^{\mathrm{bal}}_{2p} = 32.5 \pm 2.1$ meV is obtained from the intensity, the true spin-averaged 2p-level width is found to be 20% larger when corrected by using the crystal spectrometer result (Table 7). The larger value is in good agreement with recent results from low-energy scattering experiments [150].

5.2. Antiprotonic deuterium

5.2.1. 1s ground state

Evidence was found for the $\bar{p}$D Lyman α transition [224] (Fig. 10—*right*). The Lyman α yield of $Y_K = 2.3 \pm 1.3 \times 10^{-3}$, deduced from yield ratios in the direct measurement, is only in fair agreement with the values derived from the 2p annihilation width measured with the crystal spectrometer ($Y_K = 5.2 \pm 0.7 \times 10^{-4}$ [86]) and a recent fit to the $\bar{p}$D cascade data by Batty ($Y_K = 3.2 \times 10^{-4}$ [231]). Besides the low statistics the analysis described by Augsburger et al. [224] is additionally complicated by the background shape and contamination lines, but the signals from all three CCDs used in the experiment were found to be still consistent.

Surprising is the small value for the broadening, comparable to the ground-state broadening in hydrogen. From scaling of the hadronic 2p level widths based on the geometrical overlap of (hydrogen-like) wavefunctions a value is derived, which is a factor of about 2 larger. It is just consistent with the result of the direct measurement [86] (Table 7). Considering the low expected yield, however, it is questionable that the small

Table 8
Spin-averaged $\bar{p}$p scattering lengths $\mathbf{a_s}$, volumes $\mathbf{a_p}$, and $\bar{\mathrm{N}}$N isospin scattering lengths $\mathbf{a_I}$

	Experiment		Theory		
	$\bar{p}$H	Scattering	DR1[f]	KW[f]	Eff. range[g]
$\mathbf{a}^{\mathbf{cs}}_{\mathbf{s},\bar{\mathbf{p}}\mathrm{p}}$/fm	$0.913 \pm 0.018 - \mathbf{i}0.694 \pm 0.027$[a]	$-\mathbf{i}0.69 \pm 0.03$[e]	$0.83 - \mathbf{i}0.59$	$0.82 - \mathbf{i}0.67$	
$\mathbf{a}^{\mathbf{s}}_{\mathbf{s},\bar{\mathbf{p}}\mathrm{p}}$/fm	$0.95 \pm 0.02 - \mathbf{i}0.73 \pm 0.03$[b]		$0.91 - \mathbf{i}0.72$	$0.88 - \mathbf{i}0.82$	$0.4 - \mathbf{i}0.6$
$\Im\mathbf{a}_{\mathbf{s},\mathbf{I=1}}$/fm	-0.83 ± 0.07[c]		−0.62	−0.76	−0.83
$\Im\mathbf{a}_{\mathbf{s},\mathbf{I=0}}$/fm	-0.63 ± 0.08[d]		−0.87	−0.92	−0.60
$\mathbf{a}^{\mathbf{s}}_{\mathbf{p},\bar{\mathbf{p}}\mathrm{p}}$/fm^3	$-0.61 \pm 0.81 - \mathbf{i}0.77 \pm 0.06$[a]	$-\mathbf{i}0.75 \pm 0.06$[e]	$-0.26 - \mathbf{i}0.71$	$-0.40 - \mathbf{i}0.75$	$-0.6 - \mathbf{i}0.2$

[a] Scattering length in the presence of the Coulomb field $\mathbf{a^{cs}}$ as obtained with the Trueman formula to second order from $\bar{p}$H atom data [150].

[b] The pure strong-interaction scattering length $\mathbf{a^s}$ determined from $\mathbf{a^{cs}}$ by using the method of Kudryavtsev and Popov [99]. At present the correction can be neglected for p waves [97].

[c] $\Im\mathbf{a}_{\mathbf{s},\mathbf{I=1}}$ is obtained from a measurement of the $\bar{n}p$ annihilation cross section [226].

[d] Obtained with the isospin relation $\mathbf{a}_{\mathbf{s},\bar{\mathbf{p}}\mathrm{p}} = \frac{1}{2}(\mathbf{a}_{\mathbf{s},\mathbf{I=0}} + \mathbf{a}_{\mathbf{s},\mathbf{I=1}})$.

[e] Analysis of $\bar{p}$ scattering data of Protasov et al. [150].

[f] Coulomb strong interference for the potentials DR1 and KW as discussed by Carbonell et al. [97].

[g] Effective range analysis of Pirner et al. [149].

extra intensity at about 11.5 keV can be identified unambiguously with the Kα line in $\bar{p}$D. A confirmation of the experimental result would be highly desirable.

5.2.2. 2p state

From the (3d–2p) line shape, no evidence was observed for a hyperfine structure though a large electromagnetic splitting was predicted [232] (Fig. 11: $\bar{p}$D—*asymmetric line shape*). A much better description of the line shape was achieved by introducing a 2p level splitting as calculated recently by Boucard and Indelicato [211] (Section 6.3). It allowed determination of the spin-averaged hadronic broadening Γ_{2p} from a fit to the line shape using a single Lorentzian (Fig. 11: $\bar{p}$D—*symmetric line shape*), the width of which exceeds by far the level splitting. Hence, the $\bar{p}$H system remains the only one where 2p hyperfine components are accessible. Again a statistical population of the sub-levels is assumed.

Though more than one order of magnitude larger, the measured hadronic broadening Γ_{2p} is consistent with geometrical scaling taking into account the different proton and deuterium radii [86]. Such a large broadening is predicted by a multiple-scattering ansatz, which has been successfully used for pion absorption. The magnitude of the shift ϵ_{2p}, however, is underestimated by a factor of about 5 [227].

5.3. Antiprotonic helium and lithium

In the helium and lithium isotopes hadronic effects occur in s, p, and d states, but antiprotonic K transitions cannot be observed because of the too strong p-state annihilation.

Table 9
Strong-interaction effects in hyperfine states of $\bar{p}$H. The approach DPS [156] includes close-to-threshold $\bar{\rm N}$N bound and resonance states

	$\epsilon(1^1S_0)$/eV	$\Gamma(1^1S_0)$/eV	$\epsilon(1^3S_1)$/eV	$\Gamma(1^3S_1)$/eV	$\epsilon(2^3P_0)$/meV	$\Gamma(2^3P_0)$/meV
Experiment						
PS171 [221]	-740 ± 150	1600 ± 400				
PS175 [62]			-850 ± 42	770 ± 150		
PS207 [223][a]	-440 ± 75	1200 ± 250	-785 ± 35	940 ± 80		
PS207 [86]					$+139 \pm 38$	120 ± 25
Theory						
DR1 [139]	-540	1010	-750	680	$+74$	114
KW [139]	-500	1260	-750	880	$+69$	96
DPS [156]	≈ -1300	≈ 2800	-470	290	$+27$	39

[a] Obtained from a fit using a fixed background shape and a $^3S_1/\,^1S_0$ intensity ratio of 2 (see Section 5.1.1).

The hadronic p-level broadening is measured directly (Fig. 12), whereas Γ_{3d} has to be determined from the intensity balance of the feeding transitions (nf–3d) to the (3d–2p) line (Table 10). Annihilation dominates even 3d states as can be seen from the comparison of the hadronic and radiative widths. A compilation of the existing $\bar{p}$He X-ray data is given by Schneider et al. [233].

A combined analysis of antiprotonic atom and low-energy antiproton–nucleus scattering data indicates an unexpected saturation of the annihilation strength [150, 230, 234, 235]. The imaginary part of the antiproton–nucleus scattering length of antiprotonic protonium, deuterium, and helium does not increase in line with increasing atomic weight A or, for atoms, with the overlap of the antiproton's wavefunction with the nucleus. For the scattering volumes, i.e., the p-wave interaction, after an increase saturation may occur from about $A = 4$ (Fig. 13). A deviation from the scaling with overlap for targets with A up to 23 has been found also for Γ_{3d} by Poth et al. [236] and for Γ_{4f} by Rohmann et al. [237], whereas shift values perfectly follow the scaling law [236]. Such a behavior is not understood up to now.

Isotope effects are sensitive to the relative strengths R of the $\bar{p}$p and $\bar{p}$n annihilation. As single-nucleon annihilation dominates in the lightest nuclei and effects from absorption in the nuclear halo must not be taken into account, the ratio for annihilation on neutrons to protons, when corrected for the proton–neutron ratio, reflects approximately the conditions of the free $\bar{p}$p and $\bar{p}$n reactions. Rewriting the relative annihilation probability in terms of isospin scattering lengths and volumes $\Im\mathbf{a_s}$, $\Im\mathbf{a_p}$, and $\Im\mathbf{a_d}$, respectively, this ratio is also sensitive to isospin effects. For the partial wave ℓ the relative annihilation strength is given by $R_\ell = 2\Im\mathbf{a}_{\ell,\mathbf{I=1}}/(\Im\mathbf{a}_{\ell,\mathbf{I=0}} + \Im\mathbf{a}_{\ell,\mathbf{I=1}})$. For the s-wave one obtains $R_s = 1.14 \pm 0.13$ from protonium and $\bar{n}p$ scattering data (Table 8).

The relative strength of $\bar{p}$p to $\bar{p}$n annihilation was measured by detecting the charge of the final state to $R^b = \sigma(\bar{p}n)/\sigma(\bar{p}\mathrm{p}) = 0.467 \pm 0.035$ for ^{3}He [242] and $R^b = 0.42 \pm 0.05$ for ^{4}He [243–245]. The index b indicates possible modifications for a bound system. The small value obtained for R^b, which differs significantly from the threshold value R_s, suggests $I = 0$ dominance also observed in low-energy $\bar{\rm N}$N scattering [246].

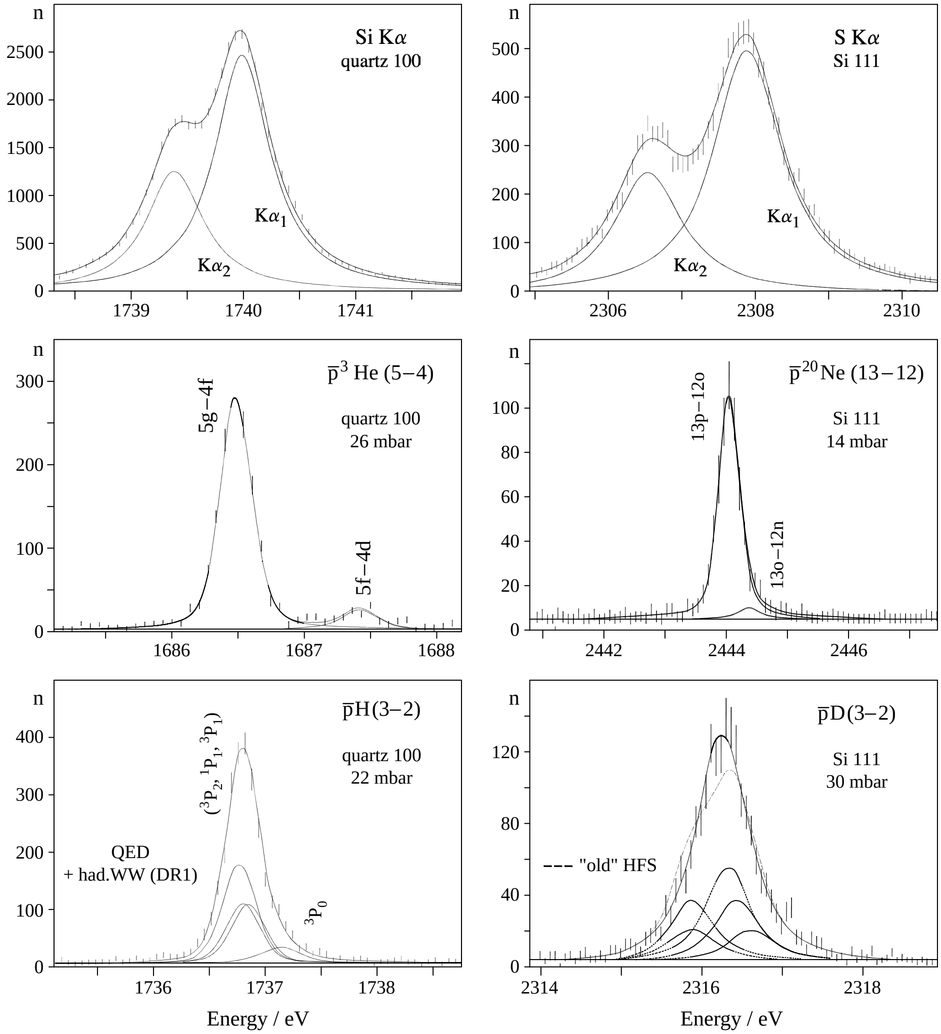

Fig. 11. Balmer α transitions of antiprotonic hydrogen and deuterium as measured with the crystal spectrometer. Kα_1 fluorescence X-rays from silicon and sulphur were used for energy calibration. The response functions of the spectrometer were obtained from the narrow transitions $\bar{p}^3$He and $\bar{p}^{20}$Ne (from [86]).

Assuming single-nucleon annihilation, the relative absorption strength in ^{3}He to ^{4}He is given by $(2 + 2R^b)/(2 + R^b)$ and results in 0.84 ± 0.02. Exploiting the isotope effect in $\bar{p}$He and assuming 50% annihilation both from p and d states, the average for the ratios $\Gamma(^3\text{He})/\Gamma(^4\text{He})$ of the 2p and 3d level broadenings yields in good agreement 0.83 ± 0.12 [233].

From measurements on deuterium $R^b = 0.81 \pm 0.03$ [247] and $R^b = 0.75 \pm 0.02$ [248] is obtained. The value of R^b, smaller than R_s, reflects the dominance of p-wave absorption

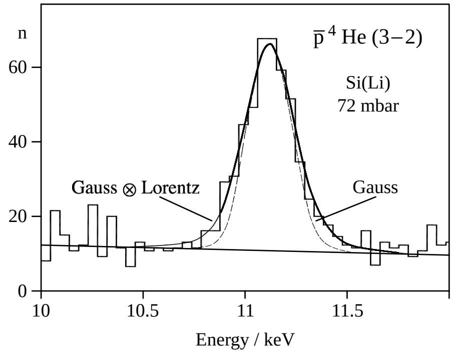

Fig. 12. Strong-interaction broadening of the Lα transition in antiprotonic helium (from [233]). The energy resolution of the Si(Li) detector (200 eV) is represented by the Gaussian. The total line shape is given by the convolution with the natural Lorentzian line shape.

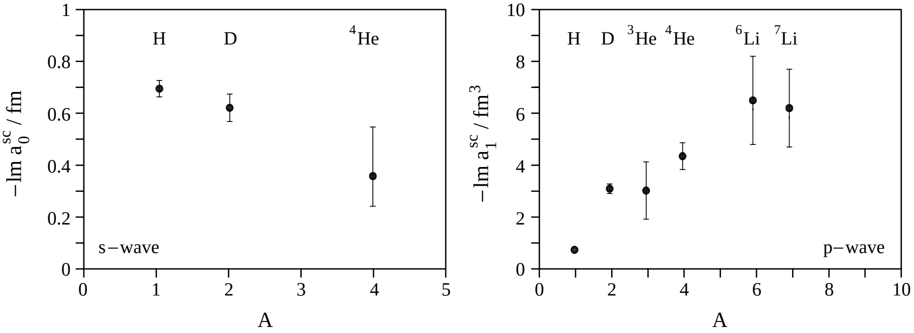

Fig. 13. Imaginary parts of the antiproton–nucleus scattering lengths (s-wave: *left*) and volumes (p-wave: *right*) as a function of atomic weight A from a combined analysis of exotic-atom and scattering data (adapted from Protasov et al. [150]). The pre-LEAR results for the lithium isotopes of Guigas et al. [238] have been replaced by the more recent results of Poth et al. [236].

in $\bar{p}$D at all target densities [231]. It is corroborated by fits to low-energy scattering data resulting in $R_p = 0.35$ and 0.2 for the p-wave [147, 148].

In terms of isospin, the ratio $R_b = 2\frac{\sigma(I=1)/\sigma(I=0)}{(1+\sigma(I=1)/\sigma(I=0))}$. Evidence for isospin-dependent annihilation strength has been found in the helium isotopes both from the detection of the final state [244, 245], $\bar{p}$He X-ray measurements [233], and from the analysis of $\bar{p}$p and $\bar{n}$p cross sections [147, 148]. For a conclusive result to corroborate the $\bar{p}$p data, the quality of the $\bar{p}$He data is not sufficient (Table 8). To determine the relative annihilation strength an accuracy of at least 10% is required, which is feasible with present day experimental techniques.

5.4. *Kaonic hydrogen and helium*

Kaonic atom experiments suffer currently from the worldwide non-availability of low-energy kaon beams, which in the past never reached the quality of pion or antiproton

Table 10
Spin-averaged hadronic shifts ϵ and broadenings Γ in the helium and lithium isotopes compared to theoretical predictions. The 2p width was measured directly with semiconductor detectors as a line broadening. The 3d-level broadening is determined from the intensity balance of the (nf–3d) and the (3d–2p) transitions and the radiative width of the 3d state Γ^X_{3d}

	ϵ_{2p}/eV	Γ_{2p}/eV	Γ_{3d}/meV	Reference	Γ^X_{3d}/meV[a]
$\bar{p}^3$He					1.56
Experiment	-17 ± 4	25 ± 9	2.14 ± 0.18	[233]	
Optical potential fit	-6 ± 1	24 ± 2	1.30 ± 0.15	[239]	
Multiple scattering	-17.3	42.1	2.16	[240]	
$\bar{p}^4$He					1.44
Experiment	-18 ± 2	45 ± 5	2.36 ± 0.10	[233]	
Optical potential fit	-8 ± 1	25 ± 2	1.67 ± 0.16	[239]	
Multiple scattering	-18.2	40.4	2.46	[240]	
$\bar{p}^6$Li					6.48
Experiment	-215 ± 25	660 ± 170	135 ± 16	[236]	
$\bar{p}^7$Li					6.48
Experiment	-265 ± 20	690 ± 170	129 ± 13	[236]	

[a] Γ^X_{3d} is corrected for a contribution from the center-of-mass motion (Fried–Martin correction [241]).

sources. For hydrogen, several attempts to measure kaonic X-ray transitions at the highly pion contaminated beams were performed [249–251] in the 1970s and 1980s. But only a recent measurement was able to establish unambiguously the K^-p K X-ray pattern (Fig. 14) by using a highly sophisticated target–detector set-up (Fig. 8) [218, 219].

The hadronic effects for the 1s ground state as determined from this experiment result in a value for the complex scattering length $\mathbf{a_{K^-p}}$ which is consistent with a multichannel analysis of low-energy scattering data [163] (Table 11). The negative sign of $\Re \mathbf{a_{K^-p}}$ for the scattering length corresponds to a repulsive interaction as expected, in contrast to the results of the first-generation experiments, which indicated a positive sign for the shift. Furthermore, from the relative intensities of the K transitions—by using the cascade code of [58]—a guess for $\Gamma_{2p} \approx 0.3$ meV is obtained. The result of this experiment suggests that the *kaonic hydrogen puzzle* disappeared and the K^-p system exhibits a normal threshold behavior.

Whereas the severe discrepancy between the first exotic-atom data and low-energy scattering seems to be resolved for KH, the situation in K^4He is still puzzling, because neither optical potential [239] nor microscopic calculations [164, 252] were able to reproduce the atom data (Table 11). A small imaginary part, however, is common to all solutions. Explanations offered are (i) phase-space limitations because of a strong binding [253, 254], and (ii) kaon–nucleus bound states causing such an anomalous threshold behavior [255–258]. On the other hand, the KH results of [218, 219] are not in favor of an anomalous threshold behavior as given by the standard form of the optical potential.

Modern theories go beyond the optical potential approach and are based on χPT formulated with three flavors, i.e., incorporate also the s quark [116, 260]. For conclusive

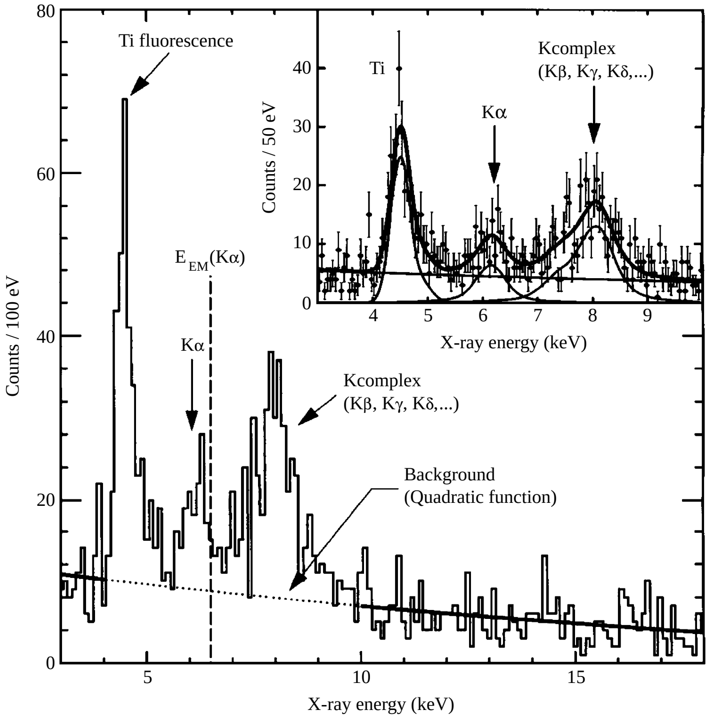

Fig. 14. The K series in kaonic hydrogen as measured at KEK by Iwasaki et al. [218]. The experiment was performed with hydrogen gas pressurized to 4 bar at a temperature of 100 K.

Table 11

Hadronic effects in light kaonic atoms. The total errors for shift and width were calculated quadratically from statistical and systematic errors as given by [218, 219]. The values for the scattering lengths $\mathbf{a_0}$ and $\mathbf{a_1}$ of the isospin channels are taken from a multichannel analysis of low-energy KN data by Martin ("Low-energy scatt." [163]). The resulting shift and broadening, obtained from the scattering length $\mathbf{a_{K^-p}}$ with the Deser formula, are consistent with the result of the KEK measurement [218, 219]. Experimental values for K^4He represent the average of the results of [249–251]. No convergence of optical potential parameters is obtained when fitting to the K^4He data ("Optical pot." $(Z = 2)$). Vice versa, the fit to heavier kaonic atoms ("Optical pot." $(Z > 2)$) does not reproduce the helium measurement

	ϵ_{1s}/eV	Γ_{1s}/eV	$\mathbf{a_{K^-p}}$/fm	Reference
KH				
Experiment	-323 ± 64	407 ± 230	$(-0.78 \pm 0.15) + \mathbf{i}(0.49 \pm 0.28)$	[218, 219]
Low-energy scatt.			$\mathbf{a_0} = -1.70 + \mathbf{i}0.68$ $\mathbf{a_1} = 0.37 + \mathbf{i}0.60$	[163]
$\mathbf{a_{K^-p}} = (\mathbf{a_0} + \mathbf{a_1})/2$	-274	527		
K^4He				
Experiments	-43 ± 8	55 ± 34		[249–251]
Optical pot. fit $(Z = 2)$			$(1.2 - 3.7) + \mathbf{i}(0.01 - 0.03)$	[239]
Optical pot. fit $(Z > 2)$	-0.13 ± 0.02	1.8 ± 0.1	$(0.34 \pm 0.003) + \mathbf{i}(0.84 \pm 0.03)$	[259]

tests, higher-quality data are indispensable. A new experiment has been started at the facility at the e^+e- collider DAΦNE at Frascati [261, 262]. Kaons originating from Φ decays are used and stopped in a hydrogen container surrounded by X-ray detectors. The goal is to determine ϵ_{1s} and Γ_{1s} with a relative precision of 1% and 5%, respectively. As a first result a clear signal from KH transitions was reported [263].

In addition to a precision study on hydrogen and deuterium, also for the helium isotopes an experiment using up-to-date experimental feasibilities is also lacking. Count rates are still limited and for systematic investigations of other light elements also the installation of dedicated low-energy kaon beams is highly desirable. Such a facility is being discussed within the project of the *Japanese Hadron Facility* (JHF) [264].

5.5. *Pionic hydrogen and deuterium*

5.5.1. *Cascade effects*

A conclusive test of χPT requires the knowledge of both isospin scattering lengths a^+ and a^- at about 1%, to be determined from correspondingly precise measured hadronic shift and broadening in πH. The pure hadronic parameters, however, are obscured in pionic hydrogen by two cascade effects—(i) *Coulomb de-excitation* and (ii) *resonance formation*.

- At present, the correction for Doppler broadening from *Coulomb de-excitation* is the basic limitation in the determination of the hadronic width in πH from the experiments of Sigg et al. [265] and Schröder et al. [266, 267], where the πH(3p–1s) transition was measured at a density equivalent to 15 bar. The consequences of this process for the linewidth are so far not yet sufficiently understood. A large part of the uncertainty of 7% of the hadronic broadening is given by the poorly known correction to the measured linewidth [267].
- *Resonance formation* of complex molecules such as $(\pi H)_{nl} + H_2 \rightarrow [(pp\pi)_{nvj}p]2e^-$ is known to occur in muon-catalyzed fusion [32, 268] and during the lifetime of the μH system even at lowest densities [269]. The quantum numbers v and j denote vibrational and total angular momentum of the three-body molecular state. Though the three-body system $(pp\pi)_{nvj}$ is assumed to de-excite mainly by Auger emission, it cannot be excluded that a fraction of the πH atoms bound into such molecules may decay radiatively to the ground state. Small line shifts—in this case always to lower energies—cannot be resolved and, hence, falsify the extracted hadronic shift [270].

To identify cascade effects originating from collisional processes, the measurement of the density dependence is the natural strategy. The above-mentioned cascade processes are being studied in more detail in a new experiment, aiming finally at an accuracy of 0.2% and 1% for ϵ_{1s} and Γ_{1s}, respectively [271].

5.5.2. *Ground-state shift in πH*

Effects originating from *resonance formation* were searched for by measuring the pressure dependence of the πH(3p–1s) transition energy from 3.5 bar equivalent pressure up to liquid H_2, i.e., over a density range of about 200. The density was adjusted by a

Table 12

Recent results on strong-interaction effects in pionic hydrogen and deuterium. E_{QED} represents the pure electromagnetic transition energy. The method of *energy* calibration and determination of the spectrometer resolution function (*res. f.*) is indicated (Table 5)

Transition	E_{QED}/eV	ϵ_{1s}/eV	Γ_{1s}/eV	p/bar	Calibration energy/res. f.	Reference
πH(3p–1s)	2878.808	$+7.108 \pm 0.036$	0.865 ± 0.069	15	Ar Kα/πBe(4d–3p)	[267]
		$+7.120 \pm 0.012$		4–LH$_2$	πO(6h–5g)/–	[272, 273]
πH(4p–1s)	3036.094		<0.85	10	–/πC(5g–4f)	[272, 273]
πD(3p–1s)	3077.95	-2.43 ± 0.10	1.02 ± 0.21	15	Ar Kα/πBe(4d–3p)	[277]
πD(2p–1s)	2695.527	-2.469 ± 0.055	1.093 ± 0.129	2.5	Cl Kα/πNe(7i–6h)	[278]

cryogenic target. No density dependence was observed and it is concluded that radiative de-excitation within molecules does not play a role for the currently achieved precision [272, 273]. The weighted average of the results for the individual densities is $\epsilon_{1s} = 7.120 \pm 0.008^{+0.009}_{-0.008}$ eV. The first error represents the statistical accuracy. The second one includes all systematic effects, which are due to the spectrometer set-up, imaging properties of extended Bragg crystals, analysis, and instabilities.

The agreement for ϵ_{1s} in the two recent experiments is remarkable in view of the completely different methods used for the energy calibration (Table 12). For energy calibration either the precisely measured Ar K fluorescence line or the πO(6h − 5g) transition as calculated from QED were used. At lower densities a simultaneous measurement of the πH(3p–1s) and the πO transitions (Fig. 15) was performed. At lower temperatures, measurements with H_2 and O_2 filling had to alternate.

It is noteworthy that the present accuracy of the QED calculation for the (3p–1s) transition energy amounts to ±6 meV or about 50% of the systematic error of the experiment of Hennebach et al. [273]. In addition, the uncertainty of the pion mass hardly contributes here because the energy calibration was performed with a pionic atom transition as compared to the calibration with argon Kα fluorescence X-rays by Schröder et al. [267]. Unfortunately only in the case of the (3p–1s) transition is a nearby calibration line available.

5.5.3. *Ground-state broadening in πH*

A significant improvement of background conditions by about one order of magnitude was achieved at the $\pi E5$ channel at PSI with a dedicated concrete shielding (Fig. 15). Low background is indispensable for sensitivity to the tails of the line shape which basically contain the information on the Lorentz and Doppler contributions to the total width. Furthermore, by measuring the total line width of three different transitions πH (2p–1s), πH (3p–1s), and πH (4p–1s) the effects of *Coulomb de-excitation* could be studied in more detail. After deconvolution of the crystal spectrometer response an increased total linewidth was found for the (2p–1s) line compared to the (3p–1s) transition, which is attributed to the higher energy release available for the acceleration of the pionic hydrogen system. This result is corroborated by a reduced linewidth of the (4p–1s) line.

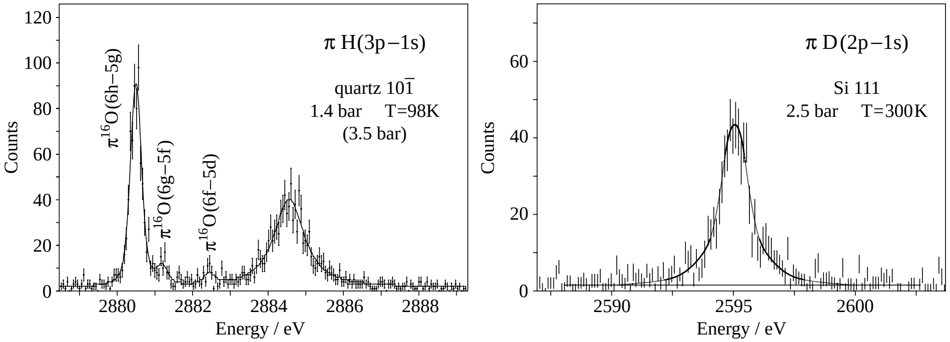

Fig. 15. *Left*: Simultaneous measurement of the (3p–1s) transition in pionic hydrogen and the calibration transition π^{16}O (6h–5g) using an H_2/O_2 gas mixture of 98%/2% at a temperature of 98 K [272]. *Right*: The (2p–1s) transition in pionic deuterium (from [278]).

Kinetic energy distributions for the 4p, 3p, and 2p initial states have been reconstructed in the framework of the cascade model of Jensen and Markushin, which takes into account the development of the velocity distribution during the atomic cascade [76–78]. The velocity distribution—adjusted to the Doppler broadening observed in liquid H_2 for the neutron TOF following charge exchange $\pi^- p \to \pi^0 n$ [75]—cannot explain the measured X-ray line shapes. The charge-exchange reaction, however, occurs only from s states (mainly from $n = 2$–5), whereas the pions finally generating the K X-ray transitions follow a de-excitation path through states with high angular momentum.

Obviously a better approach to the kinetic energy distribution is essential for the width determination, but a safe upper limit of $\Gamma_{1s} < 0.850$ eV has now been derived from the (4p–1s) transition where the contribution from *Coulomb de-excitation* is smallest [272, 273]. This upper limit is still consistent with the result obtained from the πH (3p–1s) transition [267].

A more precise value for Γ_{1s} clearly depends on cascade studies in hydrogen. It is planned to explore *Coulomb de-excitation* by measuring the pressure dependence of the line shape of Lyman transitions from *muonic hydrogen*, where any strong-interaction broadening is absent [271]. In μH, the line yields are much larger than in πH [274, 275] balancing the lower stop efficiency for muons. A realistic picture of the influence of Doppler broadening will evolve with the cascade code, which takes into account the velocity distribution at all stages of the de-excitation [78]. The knowledge will then be applied to the pionic hydrogen cascade by using the *extended cascade model* [276].

5.5.4. *Ground-state shift in πD*

To circumvent the problem arising from *Coulomb de-excitation* the ground-state shift ϵ_{1s} in pionic deuterium was exploited in combination with ϵ_{1s} of pionic hydrogen. In this way better constraints for a^+ and a^- are obtained than using the experimental result for Γ_{1s} in πH. Two measurements performed at different conditions [277, 278] yielded accurate values and agree well within the errors (Table 12). However, cascade effects on the strong-interaction shift have not been studied up to now.

The use of ϵ_{1s} from deuterium to determine the isospin scattering lengths and the pion–nucleon coupling constant requires a sophisticated treatment of the three-body system πD. Studies have been performed using the multiple-scattering ansatz including corrections for absorption by Baru and Kudryavtsev [193]. A recent re-examination by Ericson et al. exploits the GMO sum rule (Section 3.3) yielding constraints on a^+, a^- and $f^2_{\pi\mathrm{N}}$ [184, 185]. A treatment by using Faddeev equations was given by Deloff [279]. Beane et al. derive the constraints within a chiral perturbation approach together with a phenomenological deuteron wavefunction [280, 281].

It should be mentioned that in πD after molecule formation, radiative decays could be strongly enhanced in contrast to the case for pionic hydrogen [282, 283]. Measurements covering a larger density range and improved statistics could clarify the situation.

5.5.5. *Scattering lengths $a^\pm$ and the πN coupling constant*

The efforts to improve on the accuracy of the scattering lengths face the problem that the linear combination $a^+ + a^-$ to be determined from ϵ_{1s} suffers from the uncertainty of δ_ϵ (see Eq. (16)). In the framework of HBχPT the relation between exotic-atom parameters and $a^\pm$ has been calculated by Gasser et al. [178, 284]. At present the correction for ϵ_{1s} is calculated to be $\delta_\epsilon = (-7.2 \pm 2.9)\%$, the uncertainty of which is given mainly by one particular LEC—f_1 [178, 179]. As seen from Fig. 16, the experimental accuracy is significantly better than the uncertainty originating from δ_ϵ. Progress in the determination of f_1 may come from constraints for LECs derived in the framework of the chiral quark model [285].

The correction δ_Γ for the level broadening Γ_{1s} (see Eq. (17)) is subject to detailed theoretical studies and will be worked out within a short time. Here f_1 does not appear in next-to-leading order, which reduces the uncertainty substantially [179]. Therefore, a precise experimental value for Γ_{1s} provides an accurate value for the isovector scattering length a^- and the pion–nucleon coupling constant $f^2_{\pi\mathrm{N}}$. An independent source for a^- is the photoproduction $\gamma n \to \pi^- \mathrm{p}$ [286].

Schröder et al. combined their experimental results for ϵ_{1s} and Γ_{1s} from πH and ϵ_{1s} from πD [265, 267, 277] using electromagnetic corrections to the πH shift and width as given by Sigg et al. [192] (see below). They obtain $a^+ = 0.0001^{+0.0009}_{-0.0021}/m_\pi$, $a^- = 0.0885^{+0.0010}_{-0.0021}/m_\pi$, and $g^2_{\pi\mathrm{N}}/4\pi = 13.21^{+0.11}_{-0.05}$. The combined analysis of Ericson et al. [185] using $\epsilon_{1s}(\pi\mathrm{H})$ from [267] and $\epsilon_{1s}(\pi\mathrm{D})$ from [278] assumes isospin symmetry and yields

$$a^+ = -0.0012 \pm 0.0002\ (\text{statistical}) \pm 0.0008\ (\text{systematic})/m_\pi, \tag{21}$$

$$a^- = 0.0895 \pm 0.0003\ (\text{statistical}) \pm 0.0013\ (\text{systematic})/m_\pi, \tag{22}$$

$$g^2_{\pi\mathrm{N}}/4\pi = 14.11 \pm 0.05\ (\text{statistical}) \pm 0.19\ (\text{systematic}). \tag{23}$$

It must be emphasised that the π^-p scattering length used here also includes the electromagnetic correction $\delta_\epsilon = (-2.1 \pm 0.5)\%$ as given by Sigg et al. [192], which disagrees significantly from the result of Gasser et al. [179] (see above). The determination within the framework of HBχPT in third order using constraints from πH and πD yielded $a^+ = -0.0029 \pm 0.0009/m_\pi$ and $a^- = 0.0936 \pm 0.0011/m_\pi$ [280, 281]. For a^+ a range of -0.0040 to $-0.0026/m_\pi$ is obtained from the Faddeev approach [279].

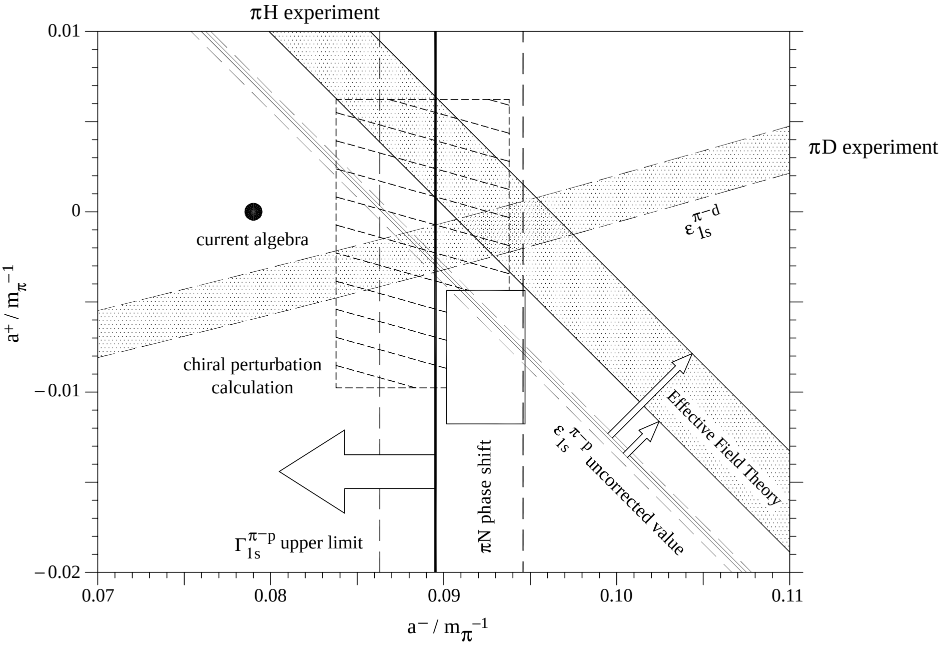

Fig. 16. Isoscalar and isovector πN scattering lengths a^+ and a^-. The narrow bands labeled $\epsilon^{\pi p}$ demonstrate the experimental accuracy achieved for ϵ_{1s} in πH as measured with the πH(3p–1s) transition (dashed band [267], solid band [273]). The uncertainty of the correction δ_ϵ to obtain $a^+ + a^-$ (narrow arrows) is dominated by the LEC f_1 [179]. The large error of Γ_{1s} is due to the correction for *Coulomb de-excitation* (dashed vertical band [267]). Recent measurements find a safe upper limit for Γ_{1s} from the πH (4p–1s) transition [273]. The dashed band labeled $\epsilon^{\pi d}$ is obtained by Ericson et al. from the combined analysis of the πH and πD s-level shifts [185]. The dot marks the leading order result given by current algebra [180, 181]. The dashed rectangle shows the constraints obtained from a third-order χPT calculation based on πN scattering [177]. The solid rectangle results from the Karlsruhe–Helsinki (KH'80) πN phase shift analysis [287].

This result for a^+, however, is in contradiction to the Karlsruhe–Helsinki phase-shift analysis yielding $a^+ = -0.0083 \pm 0.0038/m_\pi$ [287]. The other way around, the precision of a^+ is insufficient by far for predicting $\Re\mathbf{a}_{\pi\mathbf{d}}$ within an effective field theory approach [288].

A significant difference appears for the coupling constant $g^2_{\pi\mathrm{N}}/4\pi$ from the two analyses. A value well below 14 is also favored by the phase-shift analysis of the VPI/GWU group [289]. The larger value, however, is consistent with the KH'80 analysis [287] and *np* measurements as discussed in detail by Ericson et al. [185].

At present an identification of isospin violating effects in pionic hydrogen—predicted to be 1–2% for π^-p—is far from attainable. Before any missing intercept of the three bands representing the relations between a^+ and a^- can be interpreted as isospin violation, it is indispensable to achieve (i) a better knowledge of f_1 to determine $a^+ + a^-$, (ii) an accurate correction for Doppler broadening to extract a^-, and (iii) a reliable treatment of the three-body and density effects in πD. Evidence for isospin violation was reported from

Table 13
Most recent measurements for the isotope effects in pionic helium. Because of the proton excess only in pionic hydrogen and ^{3}He an attractive interaction ($\epsilon_{1s} > 0$) occurs for the s states

	ϵ_{1s}/eV	Γ_{1s}/eV	Γ_{2p}/meV	Reference
$\pi\ ^3$He	$+34 \pm 4$	36 ± 7		[297]
	$+32 \pm 3$	28 ± 7	1.6 ± 0.8^a	[293]
	$+32.3 \pm 3.0$	31.8 ± 11.0	0.69 ± 0.10^a	[298]
$\pi\ ^4$He	-75.7 ± 2.0	45 ± 3	0.72 ± 0.33^a	[70]
			2.2 ± 0.32^b	[66]
	-91 ± 12	35 ± 26		[299]
	-75.5 ± 2.0	43.7 ± 2.0	2.24 ± 0.38^c	[298]

[a] Γ_{2p} deduced from a cascade fit to the K yields.

[b] Prediction of the cascade model including ion–molecule formation using ϵ_{1s} and Γ_{1s} from experiment.

[c] From the intensity balance of the Lyman α line and the total Balmer series.

the analysis of low-energy πN scattering data [290]. However, the validity of the applied model has been criticized [291].

5.6. *Pionic helium*

A successful description of pionic helium was achieved by a microscopic approach for the optical potential based on the elementary reactions π^-p and π^-n and absorption included by πNN reactions in a semiphenomenological way [105, 106, 292]. The assumption, that for the lightest nuclei the interaction can be traced back to elementary channels, is supported by examining scattering lengths and absorptive strengths from a combinatorial point of view. The real part of the $\pi\ ^3$He scattering length appears as the sum of a deuteron and a neutron. The imaginary part, however, is about twice that of πD [293], which is understood from the fact that absorption on $I = 0$ NN pairs dominates [294, 295]. The nuclear structure effects are approximated by the proton and neutron densities, which quickly become important for $A > 4$ as can be seen from pion absorption in oxygen [293] or lithium isotopes [296], where T, ^{3}He, and α subclusters are clearly identified.

Atom data are dominated by the s-wave interaction. This is justified because experiments used dense targets (60 bar equivalent or liquid He). A fraction of 87 ± 6% s-wave absorption is obtained from the cascade model, which includes molecule–ion formation [66] (see Table 13 and Section 2). The validity of this model is corroborated by a measurement of the intensity balance of the Balmer series and the Lyman α transition described by [298].

Recently, first attempts have been made to apply χPT to three-nucleon systems [300]. The real part of the $\pi\ ^3$He scattering length $\Re \mathbf{a}_{\pi^-{}^3\mathbf{He}}$ was calculated from the elementary isospin scattering lengths a^+ and a^- and yielded reasonable agreement.[8] A comparison of $\pi\ ^3$He and πT, if available, provides another source for determining a^+ and a^- separately.

---

[8] A recent QED calculation yielded about 3 and 1 eV larger values for the electromagnetic transition energies in $\pi\ ^3$He and $\pi\ ^4$He, respectively [322] and consequently decreased the tabulated shift values.

Table 14
π^--nucleus scattering lengths $\mathbf{a}_{\pi^-\mathbf{A}}$. Assuming charge symmetry, a_{π^-n} is given by a^+–a^-

	$\mathbf{a}_{\pi^-\mathbf{A}}/m_\pi^{-1}$			
p	$+0.0883 \pm 0.0008$			[267]
n	-0.0907 ± 0.0016			Using $a^{\pm}$ from [185]
d	-0.0261 ± 0.0005	$+\mathbf{i}$	-0.0063 ± 0.0007	[278]
^{3}He	$+0.0430 \pm 0.004$	$+\mathbf{i}$	0.019 ± 0.005	[293]
^{4}He	-0.098 ± 0.003	$+\mathbf{i}$	0.030 ± 0.002	[303]

The imaginary parts of the πA scattering length obtained from the level widths yield important constraints for pion threshold production from nucleon–nucleus collisions by detailed balance [301], which in the end should be calculable within χPT. At present, calculations underestimate pion production significantly [302].

6. Supplementary results

6.1. Mass of the charged pion

For short-lived particles such as pions, X-ray spectroscopy offers a precise method for determining the particles' rest mass. Capture and cascade times for $Z > 2$ elements are in the femtosecond range and therefore fast enough that the X-ray part of the cascade is also completely passed.

The precise determination of the pion mass from the X-ray energy depends strongly on the knowledge of the status of the atomic shell. In solid state targets the number of K electrons, the only electrons contributing significantly to an energy shift, is usually not well defined because of the competition of refilling and Auger emission. Though very precise, a previous measurement using the πMg(5g–4f) transition led to an ambiguity of 16 ppm. The decision for one of the solutions (B) came also from the fact that the resulting mass squared for the limit of the muon neutrino should not become negative [304, 305].

By using gaseous targets for low-Z elements all electrons are emitted in the upper part of the atomic cascade. Because electron refilling is strongly suppressed under such conditions, X-ray emission occurs in the intermediate part from hydrogen-like exotic atoms where the nucleus can still be treated as point-like (Fig. 17).

From the measurement of the πN (5g–4f) transition, the above-mentioned ambiguity in πMg was resolved [204]. At a pressure of 1 bar, the probability for one remaining K electron was found to be less than or equal to 2% when the pion reaches the 5g level, as predicted from a cascade calculation based on the code of Akylas and Vogel [306]. Finite-size effects in the $(n, l) = (5, 4)$ and $(4, 3)$ levels are at the ppb level and, hence, can be neglected. In this experiment, the copper Kα_1 fluorescence line in the parametrisation of Deutsch et al. [210] served as energy calibration (Fig. 18).

The mass determined from pionic nitrogen is in agreement with the solution B of the experiment with pionic magnesium, which assumes two remaining K electrons. Both values are consistent with the result of the π^+-decay experiment, which yields a lower

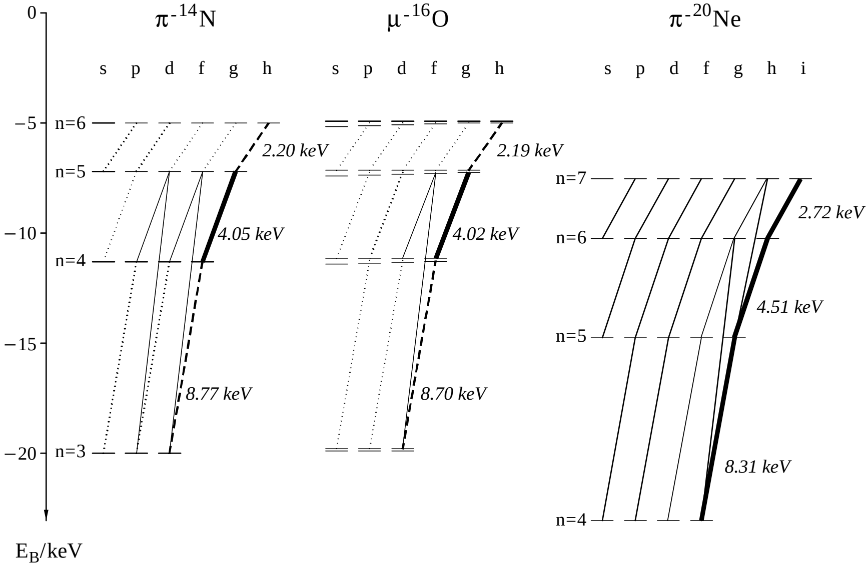

Fig. 17. The intermediate atomic cascade of light exotic atoms. During this part of the cascade, exotic atoms are free of electrons in dilute targets ("true hydrogen-like" exotic atoms).

limit for m_π when $m_{\nu_\mu} = 0$ and CPT invariance is assumed [307] (Fig. 19). From the present world average

$$m_\pi = (139.57018 \pm 0.00035)\ \mathrm{MeV/c^2} \tag{24}$$

with an error of 3 ppm, an upper limit of 190 $\mathrm{keV/c^2}$ is derived for the muon neutrino mass [34].

A further increase in accuracy requires a new method for the absolute energy calibration. The limitation in accuracy using the Cu Kα fluorescence line comes from two aspects:

- Multiple ionisation with the subsequent coupling of the vacancies creates a complicated line shape, which prevents a precise assignment of the center of gravity of the line to a wavelength.
- The πN(5–4) transition and the Cu Kα line are measured in different orders of reflection (Fig. 18). The corrections due to the index of refraction and the different penetration depths are uncertain to 2–3 ppm.

Exploiting the fact that the mass of the positively charged muon is known to 0.05 ppm [34] and again assuming CPT invariance, muonic atom transitions can be used to improve the absolute energy calibration [308]. Measuring two transitions of almost equal energy, equal in terms of quantum numbers, and at the same pressure ensures comparable experimental conditions and a similarly developing atomic cascade.

The most suitable case was found for the pair pionic nitrogen and muonic oxygen and the (5–4) transitions, again using the Si 220 reflection. The radiative decay widths are

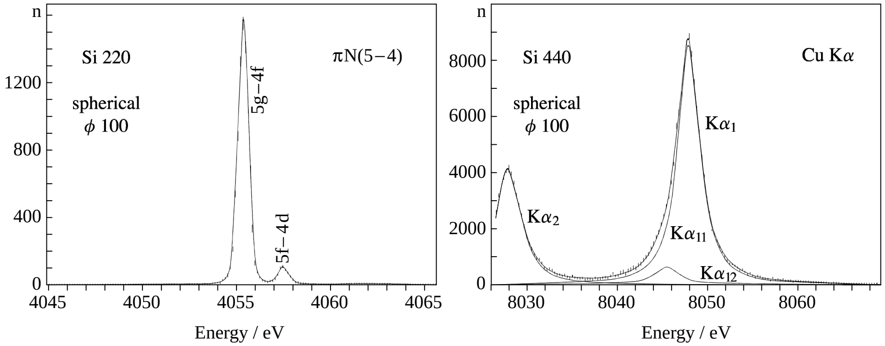

Fig. 18. The πN(5–4) transition measured at 1 bar gas pressure with a silicon (110) crystal in second order. The Cu Kα_1, measured in fourth order, was used for the energy calibration.

negligibly small compared to the intrinsic resolution of the silicon crystal (Table 5). To avoid any systematic errors from a change of the crystal spectrometer set-up, the two lines were measured simultaneously with a large-area CCD detector [217]. The count rate was adjusted to be about 15/h in each of the circular transitions using an N_2/O_2 gas mixture of 90%/10%. A small defocussing error due to the slightly different focal lengths can be corrected by means of Monte Carlo simulations. Almost 10000 events have been recorded both in the πN and the μO transitions which will result in an accuracy of 1–2 ppm for the charged pion mass [309].

Such an improvement in accuracy is desirable in various respects:

- The ongoing high-precision experiments will use pionic atom transitions for energy calibration, which are supposed to replace fluorescence X-rays as standards in the few keV range [310, 311] (Section 6.4). For example, the error Δm_π of 3 ppm contributes 7 meV or 0.13% to the uncertainty of the hadronic shift ϵ_{1s} in the experiment of Schröder et al. [267] (Section 5.5).
- The upper limit for the muon neutrino mass m_{ν_μ} has been determined from the muon momentum in the decay $\pi^+_{\text{at rest}} \rightarrow \mu^+\nu_\mu$ [307]. Here, the uncertainty is dominated by the charged pion mass. The sensitivity can be improved by a factor of about 2–3 to below 70 keV/c^2, which allows one to test certain classes of theories going beyond the Standard Model of particle physics. Taking into account cosmological bounds, a mass range between 35 eV/c^2 and 3 GeV/c^2 is possible for unstable neutrinos [312, 313]. For the sum of the masses of light stable neutrinos, the matter density of the universe yields an upper bound of 1 eV/c^2 [334]. Recent results from neutrino-oscillation experiments, though measuring only the difference of masses squared for pairs of neutrinos, suggest much smaller masses of well below 1 eV/c^2 [314].
- A recent search for muonium-to-antimuonium conversion ($M\bar{M}$) yielded a limit of $G_{M\bar{M}}/G_F \leq 3 \times 10^{-3}$ for the coupling constant $G_{M\bar{M}}$ given in units of the Fermi coupling constant G_F [315]. In combination with this, a significantly lower limit for the muon neutrino mass also excludes certain types of theory extending the Standard Model [313].

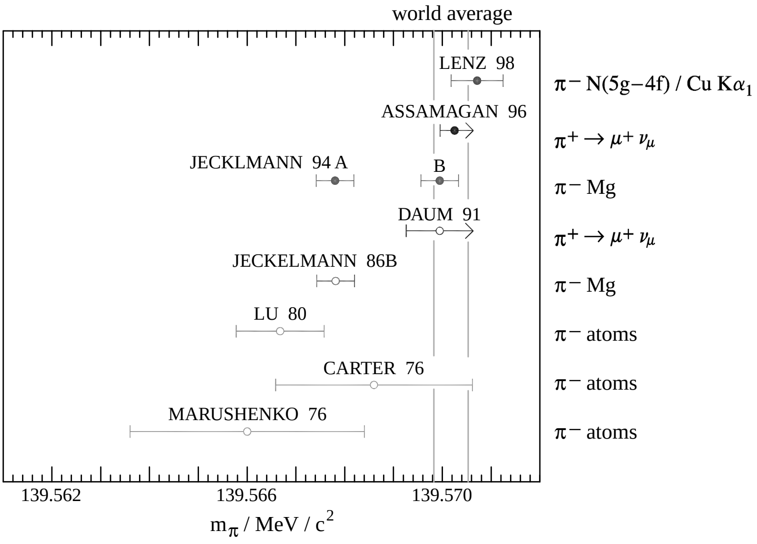

Fig. 19. The most recent results for the charged pion mass. The world average value from 2002 [34], as indicated by the vertical band, is derived from the πMg (solution B) and the πN experiment. The older measurements are also referenced in [34].

- High-precision X-ray standards are not available in the few keV range (Section 4.2.2). With pionic transitions, preferably from noble gases (Section 6.4), the precision in energy is basically limited only by the knowledge of the pion mass.

6.2. Coulomb explosion

In pionic nitrogen and muonic oxygen much larger linewidths have been measured for the (5g–4f) transitions than expected from the spectrometer resolution obtained with the πNe(6h–5g) transition (Fig. 21 and Table 5). The broadening is attributed to the *Coulomb explosion* of diatomic molecules such as N_2. Here, the πN system gains kinetic energy, when after Auger emission of several electrons the binding of the molecular system πN_2 breaks and the two charged fragments of almost equal mass are accelerated by the Coulomb force.

Such effects are well known, e.g., in laser-induced reactions [316], but now have been observed directly for the first time in the case of exotic atoms [317]. Formerly, the only evidence was deduced from the different pressure dependences of the K X-ray line yields in muonic nitrogen and neon [318]. As expected, a similar effect was measured in muonic oxygen since due to the symmetry of the diatomic molecules N_2 and O_2 the acceleration is expected to be maximal.

The best fit to the line shape was obtained assuming an additional broadening from a single box-like distribution. This implies that the velocity and, hence, the charge state of the molecular system is rather well defined. The measured Doppler broadening of the (5g–4f) transition corresponds to a velocity of about $v/c = 10^{-4}$ for the πN or μO system at the

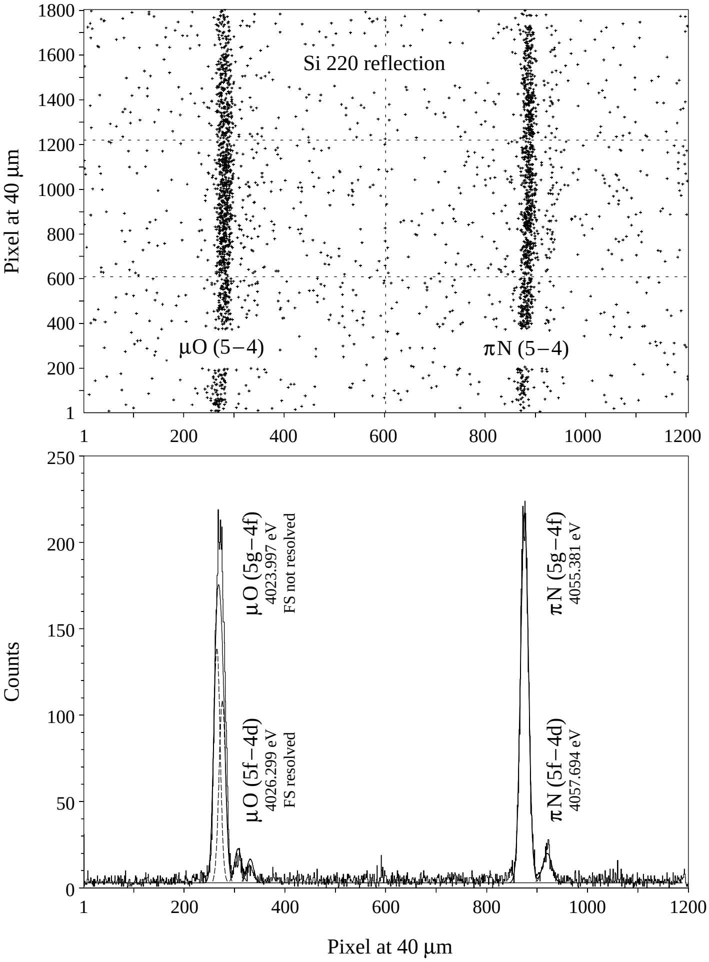

Fig. 20. Simultaneously measured reflections of the (5–4) transitions in πN and μO for the new precision determination of the charged pion mass (from [310]).

time of the X-ray emission. Starting from the timescales for the depletion of the electron shell and electron refilling, fragmentation happens approximately at the molecular bond length as explained in the following.

Auger emission is by far the fastest process in the upper and medium parts of the atomic cascade. Radiative decay rates are several orders of magnitude smaller [50, 319]. Therefore, the pion (muon) is able to remove several if not all binding electrons in less than 1 fs. Over such a short period, the (heavy) ions cannot change their relative distance substantially compared to the original molecular bond lengths of about 1.1×10^{-10} m. Only a few collisions can occur at gas pressures around 1 bar before the emission of the (5g–4f) X-ray and the mean energy loss per collision is small. Hence, the velocity

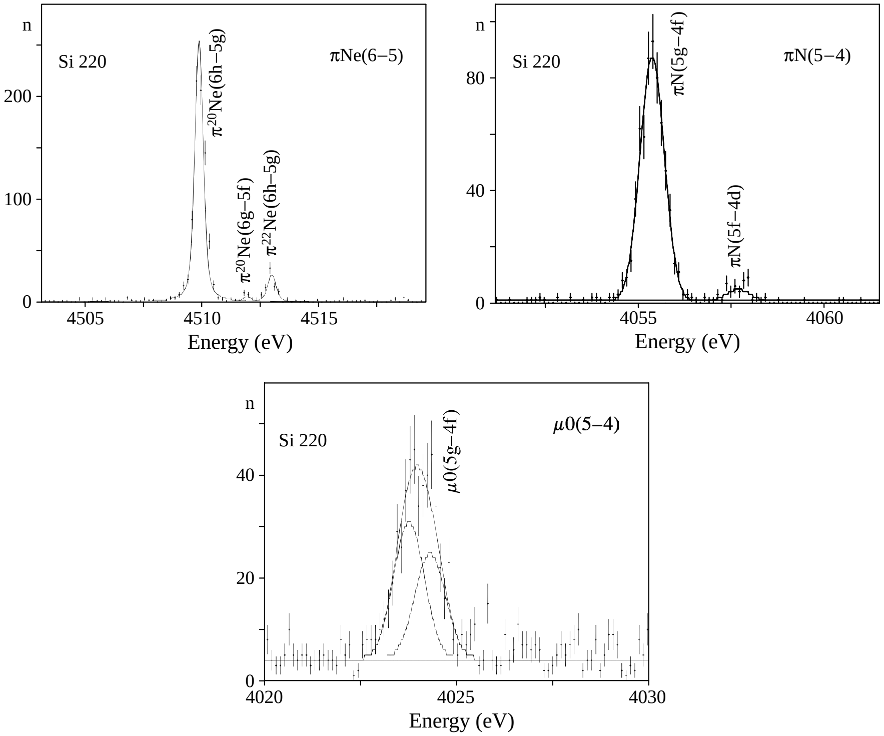

Fig. 21. *Coulomb explosion* of exotic atoms formed from diatomic molecules. The broadening of the πN and μO lines compared to the πNe transition is attributed to the acceleration of the charged ions at the time of separation of the molecule. The measurements were performed at a target pressure of 1 bar (from [317]).

derived from the Doppler broadening is close to the one originating from Coulomb repulsion.

For a fragmentation distance of about the molecular bond length, the possible range of one fragment's charge is between 2*e* and 6*e* (Table 15). Most likely, a symmetric configuration occurs, i.e., $q_1 q_2/\mathrm{e}^2 \sim 3 \times 3$ to $\sim 3 \times 4$, which corresponds approximately to the complete removal of the 6 binding electrons from the N_2 molecule with a subsequent fast emission of the remaining 2s electrons from the atom to which the pion is finally attached. A second possibility, resulting in asymmetric charge states, is separation after removal of four binding electrons leaving a N^{2+} and a $(\pi N)^{2+}$ system. In the $(\pi N)^{2+}$ system, however, all remaining electrons must be emitted before the distance deviates from the molecular bond length.

6.3. Bound-state QED

Level energies of bound states in the Coulomb field of a nucleus are obtained from the relativistic approach as given by the Dirac and the Klein–Gordon equation for fermions and bosons, respectively, together with the contributions from QED and recoil corrections.

Table 15
The measured linewidths $\Delta E_{\text{measured}}$ represent the convolution of the spectrometer response function and a Doppler contribution $\Delta E_{\text{Coulomb}}$ caused by Coulomb repulsion. To calculate the charge product $q_1 q_2/\mathrm{e}^2$, separation is assumed at the molecular bond length (adapted from [317])

	$\Delta E_{\text{measured}}$/meV	$\Delta E_{\text{Coulomb}}$/meV	$q_1 q_2/\mathrm{e}^2$
$\pi\ ^{14}$N(5g–4f)	744 ± 26	$805 \pm 35^{+30}_{-110}$	$10 \pm 1^{+1}_{-2}$
$\mu\ ^{16}$O(5g–4f)	775 ± 100	$990 \pm 100^{+230}_{-280}$	$19 \pm 4^{+9}_{-11}$

The QED contributions are dominated by vacuum polarisation in contrast to self-energy as is the case for electronic atoms. Corrections arising from the anomalous magnetic moment are important in the case of antiprotons and finite-size effects have to be taken into account for the low-lying levels.

6.3.1. Hyperfine structure in $\bar{p}$H and $\bar{p}$D

In light antiprotonic atoms, the masses of the "nucleus" and the "orbiting" particle are (almost) equal and, therefore, so also are the corresponding magnetic moments. Consequently, for the hydrogen isotopes fine and hyperfine structure splittings are both of the order $\Delta E_{FS} \approx \Delta E_{HFS} \approx \alpha^2 \cdot B_1$. Owing to the large mass, the recoil corrections due to the large anomalous magnetic moment of the proton and antiproton are significant. For that reason, the level ordering in protonium is different from that in the analog system positronium [51].

The determination of hadronic effects relies on the precisely known values of the pure electromagnetic energy levels, especially for the complex multiplet structures in antiprotonic hydrogen, where not all components can be resolved (Fig. 11). Here, the electromagnetic level splitting is a mandatory input for the analysis [86].

In the case of $\bar{p}$D, the line shape could not be understood if the analysis was based on an existing prediction of [232] for the electromagnetic level splitting. According to this calculation the electromagnetic interaction dominates the splitting in a way that the (3d–2p) line shape becomes approximately a "doublet" structure formed by the groups (^{4}P$_{3/2}$, ^{4}P$_{1/2}$) and (^{4}P$_{5/2}$, ^{2}P$_{3/2}$, ^{2}P$_{1/2}$) (Figs. 11 and 22—*old*). The measured line shape, however, does not show any evidence for such a structure (Fig. 11: *$\bar{p}$D —asymmetric fit* to the line shape using the five displayed hyperfine components).

The discrepancy between observed and expected line shape initiated a recalculation for the level splitting in both hydrogen and deuterium, which yields much smaller splittings [211] (Fig. 22—*new*). With that, a good description of the line shape was obtained with a single-line Lorentzian convoluted with the spectrometer response function (Section 5.2.2). The origin of the discrepancies is not understood so far. A critical review of the spin-averaged pure electromagnetic transition energies yielded slightly different results of the order of a few tens of meV between the former calculations by Barmo et al. [232] and Borie [321] and the recent one by Boucard and Indelicato [211] for practically all antiprotonic transitions investigated.

For the hyperfine splittings in p̄H the deviations are significant (Fig. 22—*new*). The *new* values led to a substantially improved description of the p̄H Lα line shape.

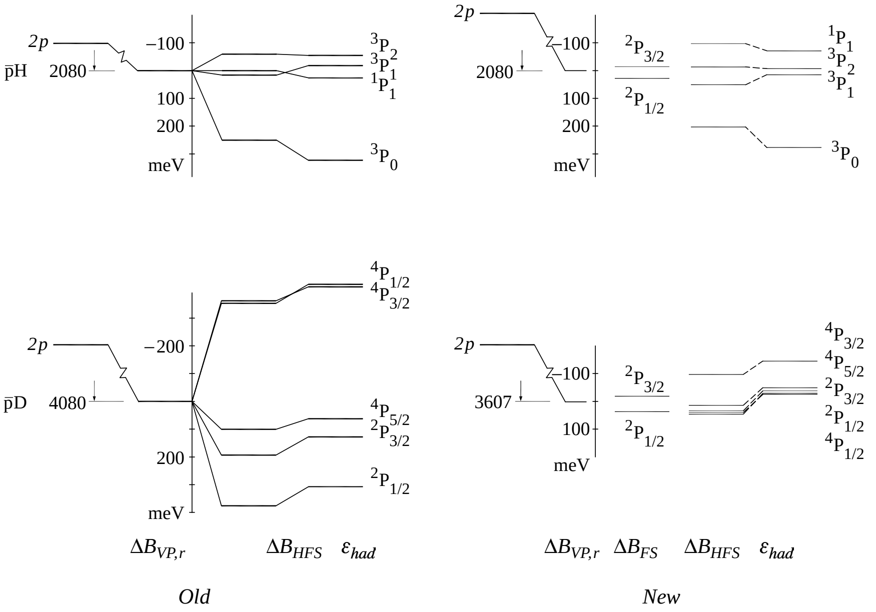

Fig. 22. Comparison of (former and recent) calculations for the electromagnetic 2p hyperfine splittings in antiprotonic hydrogen and deuterium. ($\bar{p}$H: [232, 320] and [211], $\bar{p}$D: [232] and [211]). The calculations include vacuum polarisation and recoil $\Delta B_{VP,r}$, electromagnetic fine ΔB_{FS} and hyperfine structure ΔB_{HFS}. To illustrate the magnitude of the strong interaction, the hadronic shifts ϵ_{had} as predicted by [139] ($\bar{p}$H) and [227] ($\bar{p}$D) are added in the rightmost columns.

The origin of the discrepancies is supposed to stem from the treatment of the $(g-2)$ corrections [322].

6.3.2. Antiprotonic helium

For $\bar{p}$He, the parallel transition (5f–4d) is well resolved from the circular transitions (5g–4f) (Fig. 11). The QED contributions to the energy difference are of the order 0.3 eV in the 5g and 1.4 eV in the 4f levels. Corrections due to the magnetic moment and recoil are one and two orders of magnitude smaller, respectively. As seen from Table 16, the recent theoretical approach is in agreement with experiment.

6.3.3. Test of the Klein–Gordon equation

In pionic nitrogen, the measurement of the (5g–4f) and (5f–4d) transitions allows for a precise test of the pure electromagnetic binding in a bosonic system [204]. Electron screening effects are negligibly small when using low-density targets and only s, p, and d levels are affected to more than 1 ppm by the hadronic interaction.

The measured energy difference between the circular transition $\pi\ ^{14}$N(5g–4f) and the next inner parallel transition $\pi\ ^{14}$N(5f–4d) (Fig. 23) is in good agreement with the result obtained from a full QED calculation (Table 16). The precision achieved now exceeds by a factor of about 5 that of an earlier test using pionic titanium. In the calculation of the

Table 16
Measured and calculated energy separations ΔE_{exp} and ΔE_{QED} between the circular and next inner transition

	$\Delta E_{\mathrm{exp}}(5g\text{–}4f)/(5f\text{–}4d)$	Reference	$\Delta E_{\mathrm{QED}}(5g\text{–}4f)/(5f\text{–}4d)$	Reference
$\bar{p}\ {}^3$He	907 ± 12 meV	[323]	390 meV	[232]
			913 meV	[211]
$\bar{p}\ {}^4$He	987 ± 72 meV	[323]	460 meV	[232]
			969 meV	[211]
πTi	87.6 ± 1.8 eV	[324]	88.1 ± 1.2 eV	[324]
πN	2.3082 ± 0.0097 eV	[204]	2.3129 eV	[211]

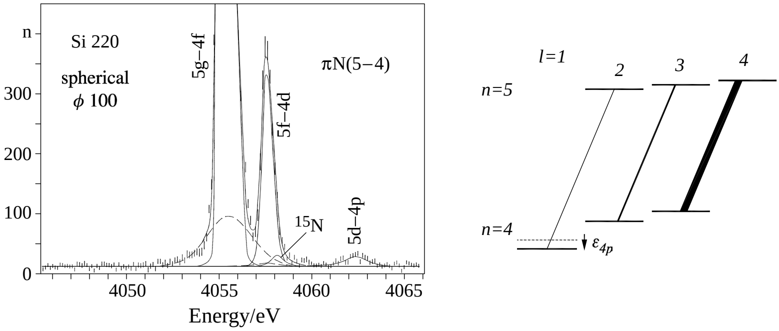

Fig. 23. An enlarged view of the πN(5–4) transitions. From the energy distance of the pionic nitrogen lines (5g–4f) and (5f–4d) the most precise test for the Klein–Gordon equation up to now was achieved. The 4p level is shifted and broadened by the strong interaction (adapted from [204]).

πTi binding energies, the largest contribution to the uncertainty (≈1 eV) stems from a level shift caused by the strong interaction. The advantage to forming a pure hydrogen-like exotic atom at principal quantum numbers large enough to suppress any finite-size effects is obvious.

6.4. Fluorescence X-rays

In the few keV range, narrow and sufficiently intense γ lines from nuclear decay are not available in practical cases and, hence, the only calibration standards easily accessible are fluorescence X-rays excited by means of X-ray tubes or radioactive sources. Precision experiments, however, may suffer twofold from properties of the fluorescence radiation.

- A precise energy determination is hindered by large natural linewidths owing to fast Auger transitions. Furthermore, multiple-hole excitations lead to complex line shapes [210], which normally make it impossible to relate unambiguously the center of gravity of the diagram line (stemming from atoms with one K-shell vacancy only)

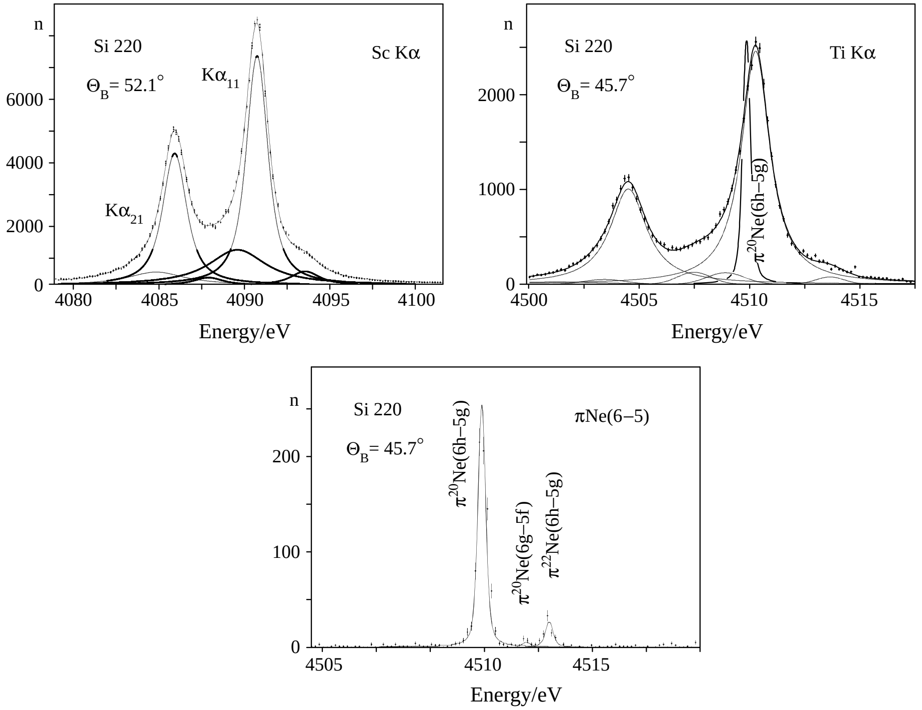

Fig. 24. Scandium and titanium Kα doublets. The response function in both cases was obtained from $\pi\ {}^{20}$Ne(6h–5g). For Ti and πNe, the "ideal case", the energy calibration and response function were obtained from the same exotic-atom transition (from [310, 311]).

to a wavelength with a precision of better than a few ppm. The creation of the inner-shell vacancies depends on the excitation mechanism itself and strong chemical shifts have been found even for Kα X-rays [325].

- The natural linewidth exceeds typical values for the resolution of crystal spectrometers by at least a factor of 3. A precise determination of response functions, however, is mandatory for line-shape analysis to extract, e.g., hadronic effects or a Doppler broadening.

A new method for achieving low-energy standards in the few keV range comes from completely ionised exotic atoms. On the basis of the high-intensity pion beams at PSI, at present pionic atoms are the most promising case [310, 311]. Up to 500 X-rays from specific "hydrogen-like" pionic atom transitions can be recorded per hour with a crystal spectrometer. Besides experimental limitations the accuracy is then determined only by the mass of the negative pion. A further improvement for m_π may come from a new calibration method using one- or two-electron systems (see Section 7.2).

The examples studied up to now are the pairs $\pi\ {}^{14}$N(5g–4f)/Sc Kα_1 and $\pi\ {}^{20}$Ne (6h–5g)/Ti Kα (Fig. 24). The accuracy for the electronic transition energy was increased by factors 12 and 3, respectively, compared to the values given in the literature (Table 17).

Table 17
Energies of Kα_1 fluorescence X-rays determined by using pionic atom transitions [310] compared to previously tabulated values (from [327, 328]). The errors do not contain a contribution from the uncertainty of the pion mass

	From pionic atoms	Calibration line	Previous determination
Sc Kα_1	4090.735 ± 0.017 eV	π ^{14}N(5g–4f)	4090.62 ± 0.20 eV
Ti Kα_1	4510.903 ± 0.019 eV	π ^{20}Ne(6h–5g)	4510.869 ± 0.049 eV

Exotic-atom transitions from diatomic targets such as N_2 are well suited for energy calibration but, because of *Coulomb explosion*, show an additional (symmetric) Doppler broadening. Hence, noble gases are preferred for measuring the spectrometer response. A precisely known resolution function allows detailed line-shape studies of fluorescence X-rays like the one performed for metallic Sc [326]. The resolution function was determined from π ^{20}Ne [210].

7. Conclusions

Recent precision experiments provided an unprecedented view of the physics of light exotic atoms in various respects. At the high-intensity pion and antiproton beams at PSI and CERN (LEAR), a novel combination of high-resolution crystal spectrometer, cyclotron trap, and X-ray detection by CCDs was used. Kaonic atom experiments using linear stop arrangements are confronted with a significant background requiring dedicated trigger capabilities.

7.1. Summary of results

7.1.1. Strong interaction

- For the two elementary **antiprotonic systems p̄H** and **p̄D**, the strong-interaction shift and broadening of both the atomic ground state 1s and the first excited state 2p are now determined from experiment. In hydrogen, hadronic effects for the hyperfine levels in the 1s and 2p states were shown to be a sensitive test for the predictions of the long-range antiproton–proton interaction.

  The results from $\bar{p}$H strongly support the approach of meson-exchange models, which is deduced from the nucleon–nucleon interaction. The large strong-interaction shift of the 2 $^3P_0$ hyperfine state is being re-discussed as evidence for close-to-threshold N̄N bound states.

  Evidence for a decreasing annihilation strength with increasing nuclear mass number was found from both the low-energy scattering and the level widths of antiproton–nucleus systems. Such a mass dependence is not yet understood.
- The recently finished **kaonic hydrogen** experiment resulted in a normal threshold behavior of the K^-p interaction. **Kaonic helium** data, however, yield a value for the scattering length contradictory to the expectations.
- Precise values for the hadronic shifts in π**H** and π**D** are available now and notable progress was achieved in the determination of the strong-interaction widths.

Combining with the most recent theoretical treatment of the three-body problem, new constraints on the πN isospin scattering lengths and π**N coupling constant** are imposed.

7.1.2. *Pion mass and electromagnetic properties of exotic atoms*

- From a study of pionic nitrogen an ambiguity of 16 ppm could be removed for the **mass of the charged pion** yielding an accuracy of less than 3 ppm for the world average value. From the ongoing analysis of a recent measurement an improvement of about a factor of 2 may be expected.
- From the energy separation of the πN(5g–4f) and πN(5f–4d) transitions the best test of the **Klein–Gordon equation** up to now was obtained.
- **Coulomb explosion** in exotic systems formed from molecules has been directly observed by the Doppler broadening of the (5–4) transitions in πN and μO.
- The measurement of antiprotonic hydrogen and deuterium initiated a recalculation of electromagnetic binding energies, leading to the discarding of some of the earlier **QED calculations**.
- A new method of **energy calibration** has been established for fluorescence X-rays in the few keV range by using transitions from “hydrogen-like” pionic atoms.

7.2. *Outlook*

At existing and future facilities, a variety of efforts are being made or discussed as regards approaching new high-precision results. Besides improved crystal spectrometers, fast-read-out CCDs [329] and new generations of triggerable X-ray detectors [330, 331] will add to existing devices.

X-ray transitions from hydrogen-like exotic atoms will become additional X-ray standards in the few keV range. They will be supplemented by high-intensity narrow electronic X-rays emitted from few-electron atoms produced in an electron–cyclotron-resonance ion trap (ECRIT). Such a device is currently set up at PSI [332].

7.2.1. *Hadronic interaction*

- In **antiprotonic hydrogen** a more precise knowledge of the strength of the $\bar{\text{N}}$N spin–spin interaction requires a high-statistics measurement of the $\bar{p}$H Kα transition. This would allow an unbiased determination of the shift and width of the $\bar{p}$H 1s hyperfine levels. Such a measurement may become feasible at the new Antiproton Decelerator (AD) facility at CERN [333] together with a slow extraction scheme (MUSASHI [334]) combined with the ASACUSA set-up [335] and high-rate-capable CCDs [329]. For $\bar{p}$D, the confirmation of the results for the s-wave strong-interaction effects would be highly desirable. To clarify the dependence of the annihilation strength and isospin effects on the nuclear mass, a significantly improved accuracy for the strong-interaction effects in antiprotonic helium isotopes is necessary.
- In the case of **kaonic hydrogen** a precision experiment aiming at an accuracy of 1% for the hadronic shift of the K$^-$H ground state has been started at the e$^+$e$^-$ collider DAΦNE—the Φ factory at Frascati [261, 262]. The experiment will go on after the

installation of triggerable X-ray detectors [330, 331]. A continuation to K^-D system is planned to access the K^-n interaction to separate the isospin 0 and 1 contributions. Also a determination of Γ_{2p} from a measurement of the intensity balance would be desirable.

- The new **pionic hydrogen** experiment aims at a determination of the isovector πN scattering lengths and the πN coupling constant to 1% [271]. The increase in precision relies on new advanced techniques in the study of crystal spectrometer properties by using narrow X-rays from few-electron atoms produced in an ECRIT and a detailed study of *Coulomb de-excitation* with muonic hydrogen.

7.2.2. *Particle properties*

- At the AD the laser experiments on antiprotonic helium performed at LEAR have been resumed and will be continued by the investigation of $\bar{p}p$ Rydberg states. A precision measurement of the **antiproton magnetic moment** is aimed at, which will surpass the accuracy of a LEAR result obtained from the level splitting in $\bar{p}\,^{208}Pb$ [21] by about three orders of magnitude [336]. Because antiprotons do not decay, further progress will come from future trap experiments [337].
- The accuracy for the **mass of the charged pion** can be improved by applying a new method for the energy calibration, which is combining few-electron systems and hydrogen-like pionic atoms. This method avoids the problem of the low count rates from muonic atoms.
- At present, the knowledge of the root mean square **proton charge radius $\mathbf{r}_p$** limits the tests of bound-state QED in hydrogen [338]. A laser-based experiment will measure $\mathbf{r}_p$ by determining the $2\,^5P_{3/2}$–$2\,^3S_{1/2}$ level splitting in the hyperfine structure of **muonic hydrogen** [339, 340]. The experiment aims at an improvement of the actual value of $r_p = 0.880 \pm 0.008$ fm [34] by at least one order of magnitude.

7.2.3. *Multidisciplinary problems*

- With an ECRIT, the gap of energy calibration standards of 1 ppm or better in the few keV range may be closed by correlating the energies from “true hydrogen-like” pionic atoms and fluorescence X-rays from low- and medium-Z one-electron systems. The multitude of transitions yields a dense set of **calibration standards** [341].
- Level energies of hydrogen-like electronic and exotic atoms are measurable and in principle calculable to better than 1 ppm [342]. Advanced tests of **bound-state QED** could be performed, e.g., **vacuum polarisation** of medium-Z pionic atoms [343, 344].
- Further applications are studies of helium-like or few-electron atoms in order to examine various theoretical approaches to the **electron–electron interaction** or **nuclear structure effects** in muonic atoms.
- Finally, X-rays from the ECRIT allow one to gauge curved Bragg crystals—mandatory for ultimate-precision experiments—without the necessity to use accelerators.

Table 18
Selected problems for a wish list of future precision studies of hadronic interactions and particle properties with the elementary exotic atoms

	Parameters	Method	
$\bar{\mathrm{N}}$N	Spin–spin interaction	$\bar{p}$H	1s hyperfine splitting
	Annihilation strength	$\bar{p}$D	1s level shift and broadening
KN	Scattering lengths $\mathbf{a_{K^-p}}$ and $\mathbf{a_{K^-n}}$	K^-H and K^-D	1s level shift and width
πN	Isospin scattering lengths $a^{\pm}$	π^-H	1s level width
	πN coupling constant $g^2_{\pi\mathrm{N}}/4\pi$		
QED	Proton charge radius r_p	μ^-H	2s–2p laser spectroscopy

Acknowledgements

It is a pleasure to thank many colleagues participating in the experiments described for illuminating discussions. The efforts in preparing numerous drawings by K.-P. Wieder and the careful reading of the manuscript by M. Hennebach and L.M. Simons are gratefully acknowledged.

References

[1] S. Tomonaga, G. Araki, Phys. Rev. 58 (1940) 90.
[2] M. Conversi, E. Pancini, O. Piccioni, Phys. Rev. 68 (1945) 232.; Phys. Rev. 71 (1946) 209.
[3] E. Fermi, E. Teller, Phys. Rev. 72 (1947) 399.
[4] W.F. Fry, Phys. Rev. 83 (1951) 594.
[5] V.L. Fitch, J. Rainwater, Phys. Rev. 92 (1953) 789.
[6] M. Camac, A.D. McGuire, J.B. Platt, H.J. Schulte, Phys. Rev. 88 (1952) 134.
[7] G.R. Burleson et al., Phys. Rev. Lett. 15 (1965) 70.
[8] A. Bamberger et al., Phys. Lett. B 33 (1970) 233.
[9] G. Backenstoss et al., Phys. Lett. B 33 (1970) 230.
[10] J. Hüfner, Phys. Rep. 21 (1975) 1.
[11] R. Seki, C.E. Wiegand, Ann. Rev. Nuclear Sci. 25 (1975) 241.
[12] G. Backenstoss, Ann. Rev. Nuclear Science 20 (1970) 467.
[13] G. Backenstoss, Contemp. Phys. 30 (1989) 433.
[14] C.J. Batty, Rep. Prog. Phys. 52 (1989) 1165.
[15] C.J. Batty, E. Friedman, A. Gal, Phys. Rep. 287 (1997) 385.
[16] E. Klempt, F. Bradamante, A. Martin, J.M. Richard, Phys. Rep. 368 (2002) 119.
[17] F. Scheck, Leptons, Hadrons and Nuclei, North-Holland, 1983.
[18] T.E.O. Ericson, W. Weise, Pions and Nuclei, Clarendon, Oxford, 1988.
[19] K.P. Gall et al., Phys. Rev. Lett. 60 (1988) 186.
[20] A.S. Denisov et al., JETPL 54 (1991) 558.
[21] A. Kreissl et al., Z. Phys. C 37 (1988) 557.
[22] D.W. Hertzog et al., Phys. Rev. D 37 (1988) 1142.
[23] E.F. Borie, G.A. Rinker, Rev. Mod. Phys. 54 (1982) 67.
[24] L.A. Schaller, Z. Phys. C 56 (1992) 548.
[25] L.M. Simons, D. Horvâth, G. Torelli (Eds.), Proceedings of the Fifth Course of the International School of Physics of Exotic Atoms, Erice, Italy, May 14–20, 1989, Plenum Press, New York, 1990, and references therein.
[26] L.N. Cooper, E.M. Henley, Phys. Rev. 92 (1953) 801.

[27] J. Bernabeu, T.E.O. Ericson, C. Jarlskog, Phys. Lett. B 50 (1974) 467.
[28] G. Feinberg, M.Y. Chen, Phys. Rev. D 10 (1974) 190; Phys. Rev. D 10 (1974) 3789.
[29] N.C. Mukhopadyay, Phys. Rep. 30 (1977) 1.
[30] J. Missimer, L.M. Simons, Phys. Rep. 118 (1985) 179.
[31] L.W. Alvarez, H. Bradner, F.S. Crawford et al., Phys. Rev. 105 (1957) 1127.
[32] Proceedings of the International Symposium on Exotic Atoms, Molecules, and Muon Catalyzed Fusion (EXAT98), Hyp. Interact. 118/119 (1999), and references therein.
[33] Proceedings of the International RIKEN Conference on Muon Catalyzed Fusion and Related Exotic Atoms (MuCF01), Hyp. Interact. 138 (2001), and references therein.
[34] K. Hagiwara et al. (PDG), Phys. Rev. D 66 (2002) 010001. Available from http://www.pdg.lbl.gov.
[35] C.E. Wiegand, D.A. Mack, Phys. Rev. Lett. 18 (1967) 685.
[36] H.J. Leisi, in: G. Fiorentini, G. Torelli (Eds.), Proceedings of the First Course on Exotic Atoms, Erice, Italy, 1977, p. 75, and references therein.
[37] Paul-Scherrer-Institut (PSI), Villigen, Schweiz, Available from http://www.psi.ch.
[38] M. Chanel, in: G. Kernel, P. Krizan, M. Mikuz (Eds.), Proceedings of the 3rd Biennial Conference on Low Energy Antiproton Physics (LEAP'94), Bled, Slovenia, September 12–17, 1994, World Scientific, Singapore, 1995, p. 511.
[39] Proceedings of the International Workshop on Exotic Atoms—Future Perspectives (EXA 2002), Vienna, Austria, 28–30 November, 2002, Austrian Academy of Science Press, Vienna, 2003.
[40] T. Yamazaki, N. Morita, R. Hayano, E. Widmann, J. Eades, Phys. Rep. 366 (2002) 183.
[41] T. Yamazaki et al., Z. Phys. A 355 (1996) 219.
[42] K. Suzuki et al., Nuclear Phys. A (2003) 831c. Available from nucl-ex/0211023, Phys. Rev. Lett., submitted for publication.
[43] S.G. Karshenboim, F.S. Pavone, G.F. Bassani, M. Ingusco, T.W. Hänsch (Eds.), PSAS 2000, Proceedings of Hydrogen II: Precise Physics with Simple Systems, Castiglione della Pescaia, Italy, June 1–3, 2000, Springer Lecture Notes in Physics, vol. 570, Springer, Berlin, 2001.
[44] P. Vogel, P.K. Haff, V. Akylas, A. Winther, Nuclear Phys. A 254 (1975) 445.
[45] T. von Egidy, F.J. Hartmann, Phys. Rev. A 26 (1982) 2355.
[46] D. Horvâth, F. Entezami, Nuclear Phys. A 407 (1984) 297.
[47] J.S. Cohen, N.T. Padial, Phys. Rev. A 41 (1990) 3460.
[48] T.S. Jensen, V.E. Markushin, in: Karshenboim S.G., V.B. Smirnov (Eds.), PSAS'02, Proceedings of Precision Physics of Simple Atomic Systems, St. Petersburg, Russia; June 30–July 4, 2002, Lecture Notes in Physics, vol. 627, Springer, Berlin, 2003, p. 37.
[49] M. Leon, H.A. Bethe, Phys. Rev. 127 (1962) 636.
[50] G.R. Burbidge, A.H. deBorde, Phys. Rev. 89 (1953) 189.
[51] H.A. Bethe, E.E. Salpeter, Handbuch der Physik, Band XXXV, Springer, Berlin, 1957.
[52] R.A. Ferrell, Phys. Rev. Lett. 4 (1960) 425.
[53] R. Bacher et al., Phys. Rev. Lett. 54 (1985) 2087.
[54] R. Bacher et al., Phys. Rev. A 38 (1988) 4395.
[55] R. Bacher et al., Phys. Rev. A 39 (1989) 1610.
[56] V.E. Markushin, Phys. Rev. A 50 (1994) 1137.
[57] V.E. Markushin, Hyp. Interact. 119 (1999) 11.
[58] E. Borie, M. Leon, Phys. Rev. A 21 (1980) 1460.
[59] G. Reifenröther, E. Klempt, Nuclear Phys. A 503 (1989) 885.
[60] G. Reifenröther, E. Klempt, Phys. Lett. B 248 (1990) 250.
[61] R. Bacher et al., Z. Phys. A 334 (1989) 93.
[62] K. Heitlinger et al., Z. Phys. A 342 (1992) 359.
[63] A.J. Rusi El Hassani et al., Z. Phys. A 351 (1995) 113.
[64] T.B. Day, G.A. Snow, J. Sucher, Phys. Rev. Lett. 3 (1959) 61; Phys. Rev. 118 (1960) 864.
[65] R.A. Burnstein, G.A. Snow, H. Whiteside, Phys. Rev. Lett. 15 (1965) 639.
[66] R. Landua, E. Klempt, Phys. Rev. Lett. 48 (1982) 1722.
[67] G. Reifenröther, E. Klempt, R. Landua, Phys. Lett. B 191 (1987) 15.
[68] G. Reifenröther, E. Klempt, R. Landua, Phys. Lett. B 203 (1988) 9.
[69] T. Koike, Y. Akaishi, Nuclear Phys. A 639 (1998) 521c.
[70] G. Backenstoss et al., Nuclear Phys. A 232 (1974) 519.

[71] L. Bracci, G. Fiorentini, Nuo. Cim. A 43 (1978) 9.
[72] J.F. Crawford et al., Phys. Lett. B 213 (1988) 391.
[73] E.C. Aschenauer et al., Phys. Rev. A 51 (1995) 1965.
[74] A. Badertscher et al., Phys. Lett. B 392 (1997) 278.
[75] A. Badertscher et al., Europhys. Lett. 54 (2001) 313.
[76] T.S. Jensen, V.E. Markushin, Eur. Phys. J. D 19 (2002) 165.
[77] T.S. Jensen, V.E. Markushin, Eur. Phys. J. D 21 (2002) 261.
[78] T.S. Jensen, V.E. Markushin, Eur. Phys. J. D 21 (2002) 271.
[79] A.V. Kravtsov, A.I. Mikhailov, I.A. Mikhailov, Phys. Rev. A 67 (2003) 042713.
[80] G. Reifenröther et al., Phys. Lett. B 214 (1988) 325.
[81] A. Adamo et al., Phys. Lett. B 285 (1992) 15.
[82] A. Bianconi et al., Phys. Lett. B 487 (2000) 224.
[83] ASACUSA status report 2002, CERN/SPSC 2003–010, SPSC–M–695 (2003).
[84] T.S. Jensen, private communication (2003).
[85] K.A. Aniol et al., Phys. Rev. A 28 (1983) 2684.
[86] D. Gotta et al., Nuclear Phys. A 660 (1999) 283.
[87] G. Reifenröther, E. Klempt, Phys. Lett. B 245 (1990) 129.
[88] C. Batty, Nuclear Phys. A 655 (1999) 203c, and references therein.
[89] U. Schaefer et al., Nuclear Phys. A 495 (1989) 451.
[90] C.A. Baker et al., Nuclear Phys. A 483 (1988) 631.
[91] M. Siegbahn, Spectroscopy of X-rays, Oxford University Press, 1925.
[92] S. Deser, L. Goldberger, K. Kaufmann, W. Thirring, Phys. Rev. 96 (1954) 774.
[93] T.L. Trueman, Nuclear Phys. 26 (1961) 57.
[94] A. Partensky, T.E.O. Ericson, Nuclear Phys. B 1 (1967) 382.
[95] E. Lambert, Hel. Phys. Acta 42 (1969) 667.
[96] M.J. Turner, D.F. Jackson, Phys. Lett. B 130 (1983) 362.
[97] J. Carbonell, J.-M. Richard, S. Wycech, Z. Phys. A 343 (1992) 325.
[98] J. Carbonell, K.V. Protasov, J. Phys. G: Nuclear Part. Phys. 18 (1992) 1863.
[99] A.E. Kudryavtsev, V.S. Popov, JETP Lett. 29 (1979) 280.
[100] V.C. Mur, V.S. Popov, Sov. J. Nuclear Phys. 3 (1983) 844.
[101] V.B. Mandelzweig, Nuclear Phys. A 292 (1977) 333.
[102] C.J. Batty, Sov. J. Part. Nuclear 13 (1982) 71.
[103] C.J. Batty, E. Friedman, A. Gal, Nuclear Phys. A 689 (2001) 721.
[104] J. Konijn et al., Nuclear Phys. A 519 (1990) 773.
[105] M. Ericson, T.E.O. Ericson, Ann. Phys. 36 (1966) 323.
[106] M. Krell, T.E.O. Ericson, Nuclear Phys. B 11 (1969) 521.
[107] L.S. Kisslinger, Phys. Rev. 98 (1955) 761.
[108] C.J. Batty, E. Friedman, A. Gal, Nuclear Phys. A 592 (1995) 487.
[109] M. Lacombe et al., Phys. Lett. B 101 (1981) 139.
[110] R. Machleidt, K. Holinde, Ch. Elster, Phys. Rep. 149 (1987) 1.
[111] S. Weinberg, Physica A 96 (1979) 327.
[112] J. Gasser, H. Leutwyler, Ann. Phys. 158 (1984) 142.
[113] G. Ecker, Prog. Part. Nuclear Phys. 35 (1995) 1.
[114] A.W. Thomas, W. Weise, The Structure of the Nucleon, WILEY–VCH, Berlin, 2001.
[115] S. Scherer, Introduction to Chiral Perturbation Theory, hep–ph/0210398v1, to be published in Advances in Nuclear Physics, vol. 27, Kluwer Academic Publishers.
[116] J. Gasser, H. Leutwyler, Nuclear Phys. B 250 (1985) 465.
[117] J. Gasser et al., in [165], p. 659.
[118] M.E. Sainio, in: MENU'01, Proceedings of the 9th Symposium on Meson–Nucleon Physics and the Structure of the Nucleon, πN newsletter, vol. 16, 2002, p. 138, and references therein.
[119] J. Gasser, H. Leutwyler, M.P. Locher, M.E. Sainio, Phys. Lett. B 213 (1988) 85.
[120] M.A. Alberg et al., Phys. Rev. D 27 (1983) 536.
[121] M. Kohno, W. Weise, Phys. Lett. B 152 (1985) 330.
[122] J.A. Niskanen, V. Kuikka, A.M. Green, Nuclear Phys. A 443 (1985) 691.
[123] M. Kohno, W. Weise, Nuclear Phys. A 454 (1986) 429.

[124] S. Furui, Z. Phys. A 325 (1986) 375.
[125] G. Ihle, H.J. Pirner, J.M. Richard, Phys. Lett. B 183 (1987) 15.
[126] T.D. Lee, C.N. Yang, Nuovo Cim. III (1956) 749.
[127] R.A. Bryan, R.J.N. Phillips, Nuclear Phys. B 5 (1968) 201.
[128] W.W. Buck, C.B. Dover, J.M. Richard, Ann. Phys. (NY) 121 (1979) 47.
[129] C.B. Dover, J.M. Richard, Phys. Rev. C 21 (1980) 1466.
[130] J. Côté et al., Phys. Rev. Lett. 48 (1982) 1319.
[131] A.M. Green, S. Wycech, Nuclear Phys. A 377 (1982) 441.
[132] M. Pignone et al., Phys. Rev. Lett. 67 (1991) 2423.
[133] A.M. Green, J.A. Niskanen, Prog. Part. Nuclear Phys. 18 (1987) 93.
[134] L. Mandrup et al., Nuclear Phys. A 512 (1990) 591.
[135] C.B. Dover, J.M. Richard, J. Carbonell, Phys. Rev. C 44 (1991) 1281.
[136] W.B. Kaufmann, H. Pilkuhn, Phys. Rev. C 17 (1978) 215.
[137] W.B. Kaufmann, Phys. Rev. C 19 (1979) 440.
[138] J.M. Richard, M.E. Sainio, Phys. Lett. B 110 (1982) 349.
[139] J. Carbonell, G. Ihle, J.M. Richard, Z. Phys. A 334 (1989) 329.
[140] B. Moussallam, Z. Phys. A 325 (1986) 1.
[141] A. Abele et al., Euro. Phys. J. C 17 (2000) 583.
[142] H. Pilkuhn, Z. Phys. A 272 (1975) 259.
[143] W.B. Kaufmann, H. Pilkuhn, Phys. Lett. B 62 (1976) 165.
[144] W.B. Kaufmann, H. Pilkuhn, Phys. Lett. B 166 (1986) 279.
[145] R. Schmitt et al., Phys. Rev. C 58 (1998) 3195.
[146] A. Trzińska et al., Phys. Rev. Lett. 87 (2001) 082501.
[147] I.L. Grach, B.O. Kerbikov, Yu.A. Simonov, Sov. J. Nuclear Phys. 48 (1988) 609; Phys. Lett. B 208 (1988) 309.
[148] J. Mahalanabis, H.J. Pirner, T.-A. Shibata, Nuclear Phys. A 485 (1988) 546.
[149] H.J. Pirner, B.O. Kerbikov, J. Mahalanabis, Z. Phys. A 338 (1991) 111.
[150] K.V. Protasov, G. Bonomi, E. Lodi Rizzini, A. Zenoni, Eur. Phys. J. A 7 (2000) 429.
[151] C.F. Chew, in: Proc. 3rd Eur. Symposium on $N\bar{N}$ Interactions, Stockholm, 1976, Pergamon Press, New York, 1977, p. 515.
[152] G.C. Rossi, G. Veneziano, Nuclear Phys. B 123 (1977) 507.
[153] I.S. Shapiro, Phys. Rep. 35 (1978) 129, and references therein.
[154] R.H. Landau, J. Schnick, Phys. Rev. C 36 (1987) 1942.
[155] O.D. Dalkarov, K.V. Protasov, I.S. Shapiro, JETP Lett. 47 (1988) 75.
[156] O.D. Dalkarov, K.V. Protasov, I.S. Shapiro, Int. J. Mod. Phys. A 5 (11) (1990) 2155.
[157] J. Carbonell, O.D. Dalkarov, K.V. Protasov, I.S. Shapiro, Nuclear Phys. A 535 (1991) 651.
[158] T.E.O. Ericson, F. Scheck, Nuclear Phys. B 19 (1970) 450.
[159] R.H. Dalitz, in [34], p. 748.
[160] G. Otter, Fortschritte der Physik 15 (1967) 333.
[161] J. Law, M.J. Turner, R.C. Barett, Phys. Rev. C 35 (1987) 305.
[162] P.B. Siegel, Z. Phys. A 328 (1987) 239.
[163] A.D. Martin, Nuclear Phys. B 179 (1981) 33.
[164] M. Mizoguchi, S. Hirenzaki, H. Toki, Nuclear Phys. A 567 (1994) 893.
[165] Proc. of the III. Int. Workshop on Physics and Detectors for DAΦNE, Frascati Physics Series, vol. XVI, 1999, and references therein.
[166] P.M. Gensini, preprint DFUPG–98–GEN–02. Available from hep-ph/9804344 (1998).
[167] B. Adeva et al., CERN experiment PS212 (DIRAC), CERN/SPSLC 95–1 (1995); CERN/SPSC 2000–032 (2000), SPSC/P284 add.1.
[168] S. Pislak et al., Phys. Rev. Lett. 87 (2001) 221081.
[169] Proceedings of HADATOM02, CERN, Geneva, October 14–15, 2002, Available from hep-ph/0301266.
[170] A. Gall, J. Gasser, V.E. Lyubovitskij, A. Rusetsky, Phys. Lett. B 462 (1999) 335.
[171] G. Colangelo et al., Phys. Rev. B 488 (2000) 261.
[172] G. Colangelo, J. Gasser, H. Leutwyler, Nuclear Phys. B 603 (2001) 125.
[173] J. Gasser, V.E. Lyubovitskij, A. Rusetsky, A. Gall, Phys. Rev. D 64 (2001) 016008.
[174] E. Jenkins, A.V. Manohar, Phys. Lett. B 255 (1991) 558.

[175] U.-G. Meissner, Czech. J. Phys. 45 (1995) 153.
[176] U.-G. Meissner, S. Steininger, Phys. Lett. B 419 (1998) 403.
[177] N. Fettes, U.-G. Meissner, S. Steininger, Nuclear Phys. A 640 (1998) 199.
[178] V.E. Lyubovitskij, A. Rusetsky, Phys. Lett. B 494 (2000) 9.
[179] J. Gasser et al., Eur. Phys. J. C 26 (2003) 13.
[180] S. Weinberg, Phys. Rev. Lett. 17 (1966) 616.
[181] Y. Tomozawa, Nuovo Cim. A (1966) 707.
[182] M.L. Goldberger, H. Miyazawa, R. Oehme, Phys. Rev. 99 (1955) 986.
[183] Proceedings of the Eighth International Symposium on Meson–Nucleon Physics and the Structure of the Nucleon, Zuoz, Switzerland, August 15–21, 1999, πN newsletter 15 (1999).
[184] T.E.O. Ericson, B. Loiseau, A.W. Thomas, Phys. Scripta T87 (2000) 71.
[185] T.E.O. Ericson, B. Loiseau, A.W. Thomas, Phys. Rev. C 66 (2002) 014005.
[186] M.L. Goldberger, S.B. Treiman, Phys. Rev. 110 (1958) 1178.
[187] H. Leutwyler, in [183], p. 1.
[188] V. Bernard, N. Kaiser, U.-G. Meissner, Phys. Rev. C 52 (1995) 2185.
[189] G. Rasche, W.S. Woolcock, Nuclear Phys. A 381 (1982) 405.
[190] J. Spuller et al., Phys. Lett. B 67 (1977) 479.
[191] M. Mojžiš, Eur. Phys. J. C 2 (1998) 181.
[192] D. Sigg et al., Nuclear Phys. A 609 (1996) 310.
[193] V.V. Baru, A.E. Kudryavtsev, Phys. At. Nuclear 60 (1997) 1475.
[194] L.M. Simons, Phys. Scripta 90 (1988); Hyperfine Interactions 81 (1993) 253.
[195] W.H. Zachariasen, Theory of X-ray Diffraction in Crystals, J. Wiley and Sons Inc., New York, 1947.
[196] S. Brennan, P.L. Cowan, Rev. Sci. Instrum. 63 (1992) 850.
[197] H.H. Johann, Z. Phys. 69 (1931) 185.
[198] J. Eggs, K. Ulmer, Z. angew. Phys. 20 Band, Heft 2 (1965) 118.
[199] W. Beer et al., Nuclear Instrum. Meth. A 311 (1992) 240.
[200] A. Badertscher et al., Nuclear Instrum. Meth. A 335 (1993) 470.
[201] G. Zschornack, G. Müller, G. Musiol, Nuclear Instrum. Meth. 200 (1982) 481.
[202] A.E. Sandström, Handbuch der Physik, vol. XXX, Springer, Berlin, 1952, p. 78.
[203] F. Cembali et al., J. Appl. Cryst. 25 (1992) 424.
[204] S. Lenz et al., Phys. Lett. B 416 (1998) 50.
[205] D.F. Anagnostopoulos et al., Precision measurement of the energies and line shapes of antiprotonic Lyman and Balmer transitions from hydrogen and helium isotopes: LEAR experiment PS207, CERN/PSCC/90-9/P124 (1990).
[206] M. Sanchez del Rio, R.J. Dejus, XOP: Recent developments, SPIE proc. (1998) 3448.
[207] R. Deslattes, T. Mooney, private communication.
[208] R. Deslattes, E.G. Kessler Jr., P. Indelicato, E. Lindroth, in: P. Mohr, W.L. Wiese (Eds.), Atomic and Molecular Data and their Applications, AIP, 1998, p. 89. 1–56396–751–0/98.
[209] J. Schweppe, private communication.
[210] M. Deutsch et al., Phys. Rev. A 51 (1995) 283.
[211] S. Boucard, P. Indelicato, private communication.
[212] J.-P. Egger, D. Chatellard, E. Jeannet, Particle World 3 (1993) 139.
[213] D. Sigg, Nuclear Instrum. Meth. A 345 (1994) 107.
[214] J.-P. Egger, in [32], vol. 119, p. 291.
[215] H. Gorke, Thesis, University of Cologne, 1996, unpublished.
[216] J.R. Janesick, Scientific Charge-Coupled Devices, SPIE Press, Bellingham, Washington, USA, 2001.
[217] N. Nelms et al., Nuclear Instrum. Meth. A 484 (2002) 419.
[218] M. Iwasaki et al., Phys. Rev. Lett. 78 (1997) 3067.
[219] T.M. Ito et al., Phys. Rev. C 58 (1998) 2366.
[220] C.W.E. van Eijk et al., Nuclear Phys. A 486 (1988) 604.
[221] M. Ziegler et al., Phys. Lett. B 206 (1988) 151.
[222] M. Augsburger et al., in [32], vol. 118, p. 59.
[223] M. Augsburger et al., Nuclear Phys. A 658 (1999) 149.
[224] M. Augsburger et al., Phys. Lett. B 461 (1999) 417.
[225] R. Rückl, Č. Zupančič, Phys. Lett. B 150 (1985) 225.

[226] G.S. Mutchler et al., Phys. Rev. D 38 (1988) 742.
[227] S. Wycech, A.M. Green, J.A. Niskanen, Phys. Lett. B 152 (1985) 308.
[228] G.P. Latta, P.C. Tandy, Phys. Rev. 42 (1990) R1207.
[229] G.Q. Liu, J.-M. Richard, S. Wycech, Phys. Lett. B 260 (1991) 15.
[230] J. Carbonell, in: LEAP2000, Proceedings of the 6th Biennial Conference on Low Energy Antiproton Physics, Venice, Italy, August 20–26, 2000. Nuclear Phys. A 692 (2001) 11.
[231] C.J. Batty, Nuclear Phys. A 703 (2002) 702.
[232] S. Barmo, H. Pilkuhn, H.G. Schlaile, Z. Phys. A 301 (1981) 283; H. Pilkuhn, private communication (corrections).
[233] M. Schneider et al., Z. Phys. A 338 (1991) 217.
[234] A. Zenoni et al., Phys. Lett. B 461 (1999) 413.
[235] V.A. Karmanov, K.V. Protasov, A.Yu. Voronon, Eur. J. Phys. A 8 (2000) 429.
[236] H. Poth et al., Nuclear Phys. A 466 (1987) 667.
[237] D. Rohmann et al., Z. Phys. A 325 (1986) 261.
[238] R. Guigas et al., Phys. Lett. B 137 (1984) 323.
[239] C.J. Batty, Nuclear Phys. A 506 (1990) 89c.
[240] S. Wycech, A.M. Green, Z. Phys. A 344 (1992) 117.
[241] Z. Fried, A.D. Martin, Nuovo Cim. 29 (1963) 574.
[242] G. Bendiscioli et al., Nuclear Phys. B (Proc. Suppl.) (1989) 274.
[243] F. Balestra et al., Nuclear Instrum. Meth. A 234 (1985) 30.
[244] F. Balestra et al., Nuclear Phys. A 465 (1987) 714.
[245] F. Balestra et al., Nuclear Phys. A 491 (1989) 541.
[246] T. Bressani, A. Filippi, Phys. Rep. 383 (2003) 213.
[247] R. Bizarri et al., Nuovo Cim. A 22 (1974) 225.
[248] T.E. Kalogeropoulos et al., Phys. Rev. D 22 (1980) 2585.
[249] J.D. Davies et al., Phys. Lett. B 83 (1979) 55.
[250] M. Izycki et al., Z. Phys. A 297 (1980) 11.
[251] P.M. Bird et al., Nuclear Phys. A 404 (1983) 482.
[252] K. Masutani, Nuclear Phys. A 508 (1988) 565.
[253] S. Wycech, Nuclear Phys. A 450 (1985) 399c.
[254] R. Staronski, S. Wycech, Czechoslovak. J. Phys. B 36 (1986) 903.
[255] J.H. Koch et al., Phys. Rev. Lett. 26 (1971) 1465; Phys. Rev. C 5 (1972) 381.
[256] R. Seki, Phys. Rev. C 5 (1972) 1196.
[257] A.E. Kudryavtsev et al., Phys. Lett. B 143 (1984) 41.
[258] V.S. Popov et al., Sov. Phys.—JETP 61 (1985) 420.
[259] C.J. Batty, Nuclear Phys. A 372 (1981) 418.
[260] B. Borosoy, U.-G. Meissner, Ann. Phys. 254 (1997) 192.
[261] S. Bianco et al., Nuovo Cim. 22 (11) (1999) 1.
[262] C. Guaraldo, Proceedings of the VIIth International Conference on Hypernuclear and Strange Particle Physics, Torino, 23–27 October 2000; Nuclear Phys. A 691 (2001) 278.
[263] J. Zmeskal et al., The DAΦNE exotic atom research—results and future perspectives, in [39], p. 113.
[264] T. Nagae, Proceedings of the International Conference on Hypernuclear and Strange Particle Physics, Brookhaven, USA, 1997; Nuclear Phys. A 639 (1998) 551c, and references therein.
[265] D. Sigg et al., Phys. Rev. Lett. 75 (1995) 3245; Nuclear Phys. A 609 (1996) 269; Erratum A 617 (1997) 526.
[266] H.-Ch. Schröder et al., Phys. Lett. B 469 (1999) 25.
[267] H.-Ch. Schröder et al., Eur. Phys. J. C 21 (2001) 433.
[268] D. Taqqu, Muon Catalyzed Fusion, AIP Conf. Proc. 181 (1989) 217.
[269] R. Pohl et al., in [33], p. 35.
[270] S. Jonsell, J. Wallenius, P. Froelich, Phys. Rev. A 59 (1999) 3440.
[271] Measurement of the strong interaction width and shift of the ground state of pionic hydrogen, PSI experiment R–98.01, Available from http://www.pihydrogen.web.psi.ch.
[272] D.F. Anagnostopoulos et al., Precision Spectroscopy of Pionic Hydrogen, in [39], p. 71.
[273] M. Hennebach, Thesis, University of Cologne, 2003, unpublished.
[274] M. Bregant et al., Phys. Lett. A 241 (1998) 344.

[275] B. Lauss et al., Phys. Rev. Lett. 80 (1998) 3041.
[276] T.S. Jensen, V.E. Markushin, πN Newsletter 16 (2002) 358.
[277] D. Chatellard et al., Nuclear Phys. A 625 (1997) 855.
[278] P. Hauser et al., Phys. Rev. C 58 (1998) R1869.
[279] A. Deloff, Phys. Rev. C 64 (2001) 065205.
[280] S.R. Beane et al., Phys. Rev. C 57 (1998) 424.
[281] S.R. Beane et al., Nuclear Phys. A 720 (2003) 399.
[282] V.I. Korobov, private communication.
[283] J. Wallenius, private communication.
[284] J. Gasser, A. Rusetski, private communication.
[285] V.E. Lyubovitskij, Th. Gutsche, A. Faessler, R. Vinh Mau, Phys. Lett. B 520 (2001) 204.
[286] V. Bernard, Proceedings of Chiral Dynamics 1997, Mainz, Springer Lecture Notes in Physics, vol. 513. Springer, Berlin, 1998, p. 89, and references therein.
[287] R. Koch, Nuclear Phys. A 448 (1986) 1986.
[288] B. Borasoy, H. Grieshammer, Int. J. Mod. Phys. 12 (2003) 65.
[289] M.M. Pavan et al., πN Newsletter 16 (2002) 110.
[290] E. Matsinos, Phys. Rev. C 56 (1997) 3014.
[291] G. Höhler, in [183], p. 126.
[292] T.E.O. Ericson, L. Tauscher, Phys. Lett. B 112 (1982) 425.
[293] I. Schwanner et al., Nuclear Phys. A 412 (1984) 253.
[294] D. Gotta et al., Phys. Rev. C 51 (1995) 469.
[295] E. Daum et al., Nuclear Phys. A 589 (1995) 553.
[296] M. Dörr et al., Nuclear Phys. A 445 (1985) 557.
[297] G.R. Mason et al., Nuclear Phys. A 340 (1980) 240.
[298] R. el Hassani, Thesis, ETH Zürich no. 9256, 1990, unpublished.
[299] S. Baird et al., Nuclear Phys. A 392 (1983) 297.
[300] V. Baru et al., Eur. Phys. J. A 16 (2003) 437.
[301] J.-F. Germond, C. Wilkin, J. Phys. G: Nuclear Phys. 14 (1988) 181.
[302] C. de Rocha, G. Miller, U. van Kolck, Phys. Rev. C 61 (2000) 034613.
[303] J. Hüfner, L. Tauscher, C. Wilkin, Nuclear Phys. A 231 (1974) 455.
[304] B. Jeckelmann et al., Nuclear Phys. A 457 (1986) 709.
[305] B. Jeckelmann, P.F.A. Goudsmit, H.J. Leisi, Phys. Lett. B 335 (1994) 326.
[306] V.R. Akylas, P. Vogel, Comput. Phys. Comm. 15 (1978) 291.
[307] K. Assamagan et al., Phys. Rev. D 53 (1996) 6065.
[308] D. Anagnostopoulos et al., New Precision Determination of the Charged Pion Mass, PSI experiment R–97.02 (1997).
[309] D.F. Anagnostopoulos et al., Acta Phys. Pol. B 31 (2000) 2219.
[310] D.F. Anagnostopoulos et al., Charged Pion Mass and Energy Calibration Standards Based on Pionic X-ray Transitions, in [43], p. 500.
[311] D.F. Anagnostopoulos, D. Gotta, P. Indelicato, L.M. Simons, to be published in Phys. Rev. Lett.
[312] P.B. Pal, Nuclear Phys. B 227 (1983) 237.
[313] P. Herczeg, R.N. Mohapatra, Phys. Rev. Lett. 69 (1992) 2475.
[314] S. Hannestad, Phys. Rev. D 66 (2002) 125011.
[315] L. Willmann et al., Phys. Rev. Lett. 82 (1999) 49.
[316] Ph. Hering, C. Cornaggia, Phys. Rev. A 59 (1999) 2836.
[317] T. Siems et al., Phys. Rev. Lett. 84 (2000) 4573.
[318] P. Ehrhart, F.J. Hartmann, E. Köhler, H. Daniel, Z. Phys. A 311 (1983) 259.
[319] F.J. Hartmann, in [25], p. 127.
[320] E. Borie, in: U. Gastaldi, R. Klapisch (Eds.), Proceedings of the 2nd Workshop on Physics at LEAR, Erice, Italy, May 9–16, 1982, Plenum Publishing Corporation, New York, 1984, p. 561.
[321] E. Borie, B. Jödicke, Comput. Phys. 2 (6) (1988) 61.
[322] P. Indelicato, private communication (2002).
[323] D. Gotta, private communication (1998).
[324] L. Delker et al., Phys. Rev. Lett. 42 (1979) 89.
[325] J. Kawai, E. Nakamura, Y. Nihei, K. Fujisawa, Y. Goshi, Spectrochim. Acta B 45 (1990) 463.

[326] D.F. Anagnostopoulos, M. Deutsch, D. Gotta, R. Sharon, Phys. Rev. A 60 (1999) 2018.
[327] J.A. Bearden, Rev. Mod. Phys. 39 (1967) 78.
[328] R. Deslattes et al., in: A.J.C. Wilson, E. Prince (Eds.), International Tables for Crystallography, vol. C11, Kluver Academic Publishers, 1998, Table 4.2.2.4 (Chapter 4).
[329] A. Ackens et al., IEEE Trans. 46 (1999) 1995.
[330] P. Lechner et al., Nuclear Instrum. Methods A 377 (1996) 346.
[331] J. Marton et al., Target and Detector Systems for Exotic Atom Experiments, in [39], p. 223.
[332] S. Biri, L. Simons, D. Hitz, Rev. Sci. Instrum. 71 (2000) 1116.
[333] The antiproton decelerator (AD) at CERN, Available from http://www.psdoc.web.cern.ch/PSdoc/acc/ad.
[334] Y. Yamazaki, in [33], p. 141.
[335] ASACUSA status report 2001, CERN/SPSC 2002–002, SPSC–M–674 (2002).
[336] Atomic Spectroscopy and Collisions Using Slow Antiprotons (LEAR/AD experiment PS205—phase 3 experiments), Available from http://www.asacusa.web.cern.ch/ASACUSA.
[337] W. Quint, Perspectives for Low-energy Antiproton Physics at the Future GSI Accelerator Facility, Workshop Future AD Physics Program, Munich, May 15–16, 2003, Available from http://www.mpq.mpg.de.
[338] R. Rosenfelder, Phys. Lett. B 479 (2000) 318.
[339] PSI experiment R–98.03, Laser Spectroscopy of the Lamb Shift in Muonic Hydrogen.
[340] F. Kottman et al., in [33], p. 55.
[341] D.F. Anagnostopoulos et al., HCI02, Proceedings of the 11th International Conference on the Physics of Highly Charged Ions, Caen, France; Nuclear Instrum. Methods B 205 (2003) 9.
[342] P. Indelicato et al., Aspects of QED on the Framework of Exotic Atoms, in [39], p. 61.
[343] P. Indelicato, L.M. Simons, Proceedings of QED 2000, Trieste, Italy, October 5–12, 2000; AIP Conf. Proc. 564 (2001) 269.
[344] D.F. Anagnostopoulos et al., Cyclotron Trap: Future Experiments, in [39], p. 197.
[345] K. Kilsch et al., Phys. Rev. A 59 (1999) 3375.
[346] M. Gell-Mann, R. Oakes, B. Renner, Phys. Rev. 122 (1968) 2195.